

Nanomaterials for Energy and Environmental Applications

Guest Editors: Sesa Srinivasan, Arunachalanadar M. Kannan,
Nikhil Kothurkar, Yehia Khalil, and Sarada Kuravi





Nanomaterials for Energy and Environmental Applications

Journal of Nanomaterials

Nanomaterials for Energy and Environmental Applications

Guest Editors: Sesa Srinivasan,
Arunachalanadar M. Kannan, Nikhil Kothurkar,
Yehia Khalil, and Sarada Kuravi



Copyright © 2015 Hindawi Publishing Corporation. All rights reserved.

This is a special issue published in "Journal of Nanomaterials." All articles are open access articles distributed under the Creative Commons Attribution License, which permits unrestricted use, distribution, and reproduction in any medium, provided the original work is properly cited.

Editorial Board

Domenico Acierno, Italy
Katerina Aifantis, USA
Nageh K. Allam, USA
Margarida Amaral, Portugal
Martin Andersson, Sweden
Raul Arenal, Spain
Ilaria Armentano, Italy
Vincenzo Baglio, Italy
Lavinia Balan, France
Thierry Baron, France
Andrew R. Barron, USA
Reza Bayati, USA
Hongbin Bei, USA
Daniel Bellet, France
Stefano Bellucci, Italy
Enrico Bergamaschi, Italy
Samuel Bernard, France
Debes Bhattacharyya, New Zealand
Sergio Bietti, Italy
Giovanni Bongiovanni, Italy
Theodorian Borca-Tasciuc, USA
Mohamed Bououdina, Bahrain
Torsten Brezesinski, Germany
C. Jeffrey Brinker, USA
Christian Brosseau, France
Philippe Caroff, Australia
Victor M. Castaño, Mexico
Albano Cavaleiro, Portugal
Bhanu P. S. Chauhan, USA
Shafiu Chowdhury, USA
Jin-Ho Choy, Republic of Korea
Kwang-Leong Choy, UK
Yu-Lun Chueh, Taiwan
Elisabetta Comini, Italy
Giuseppe Compagnini, Italy
David Cornu, France
Miguel A. Correa-Duarte, Spain
P. Davide Cozzoli, Italy
Shadi A. Dayeh, USA
Luca Deseri, USA
Yong Ding, USA
Philippe Dubois, Belgium
Zehra Durmus, Turkey
Joydeep Dutta, Oman
Ali Eftekhari, USA
Jeffrey Elam, USA
Samy El-Shall, USA
Ovidiu Ersen, France
Claude Estournès, France
Andrea Falqui, KSA
Matteo Ferroni, Italy
Elena J. Foster, USA
Ilaria Fratoddi, Italy
Alan Fuchs, USA
Miguel A. Garcia, Spain
Siddhartha Ghosh, Singapore
P. K. Giri, India
Russell E. Gorga, USA
Jihua Gou, USA
Jean M. Greneche, France
Smrati Gupta, Germany
Kimberly Hamad-Schifferli, USA
Simo-Pekka Hannula, Finland
Michael Harris, USA
Yasuhiko Hayashi, Japan
F. Hernandez-Ramirez, Spain
Michael Z. Hu, USA
Nay Ming Huang, Malaysia
Shaoming Huang, China
David Hui, USA
Zafar Iqbal, USA
Balachandran Jeyadevan, Japan
Xin Jiang, Germany
Rakesh Joshi, Australia
Jeong-won Kang, Republic of Korea
Hassan Karimi-Maleh, Iran
Antonios Kelarakis, UK
Alireza Khataee, Iran
Ali Khorsand Zak, Iran
Philippe Knauth, France
Ralph Krupke, Germany
Christian Kübel, Germany
Prashant Kumar, UK
Michele Laus, Italy
Eric Le Bourhis, France
Burtrand Lee, USA
Jun Li, Singapore
Meiyong Liao, Japan
Shijun Liao, China
Silvia Licocchia, Italy
Wei Lin, USA
Nathan C. Lindquist, USA
Jun Liu, USA
Zainovia Lockman, Malaysia
Nico Lovergine, Italy
Jim Low, Australia
Jue Lu, USA
Songwei Lu, USA
Ed Ma, USA
Laura M. Maestro, Spain
Gaurav Mago, USA
Muhamamd A. Malik, UK
Devanesan Mangalaraj, India
Sanjay R. Mathur, Germany
Tony McNally, UK
Yogendra Mishra, Germany
Paulo Cesar Morais, Brazil
Paul Munroe, Australia
Jae-Min Myoung, Republic of Korea
Rajesh R. Naik, USA
Albert Nasibulin, Russia
Toshiaki Natsuki, Japan
Koichi Niihara, Japan
Natalia Noginova, USA
Sherine Obare, USA
Won-Chun Oh, Republic of Korea
Atsuto Okamoto, Japan
Abdelwahab Omri, Canada
Ungyu Paik, Republic of Korea
Piersandro Pallavicini, Italy
Edward A. Payzant, USA
Alessandro Pegoretti, Italy
Ton Peijs, UK
Oscar Perales-Pérez, Puerto Rico
Jorge Pérez-Juste, Spain
Alexey P. Popov, Finland
Philip D. Rack, USA
Peter Reiss, France
Orlando Rojas, USA
Marco Rossi, Italy
Ilker S. Bayer, Italy
Cengiz S. Ozkan, USA
Sudipta Seal, USA
Shu Seki, Japan
Vladimir Šepelák, Germany

Huaiyu Shao, Japan
Prashant Sharma, USA
Donglu Shi, USA
Bhanu P. Singh, India
Surinder Singh, USA
Vladimir Sivakov, Germany
Ashok Sood, USA
Adolfo Speghini, Italy
Marinella Striccoli, Italy
Xuping Sun, KSA
Ashok K. Sundramoorthy, USA
Angelo Taglietti, Italy
Bo Tan, Canada

Leander Tapfer, Italy
Valeri P. Tolstoy, Russia
Muhammet S. Toprak, Sweden
Ramon Torrecillas, Spain
Achim Trampert, Germany
Takuya Tsuzuki, Australia
Tamer Uyar, Turkey
Bala Vaidhyanathan, UK
Luca Valentini, Italy
Rajender S. Varma, USA
Ester Vazquez, Spain
Antonio Villaverde, Spain
Ajayan Vinu, Australia

Ruibing Wang, Macau
Shiren Wang, USA
Yong Wang, USA
Magnus Willander, Sweden
Ping Xiao, UK
Zhi Li Xiao, USA
Yangchuan Xing, USA
Doron Yadlovker, Israel
Yoke K. Yap, USA
Kui Yu, Canada
William Yu, USA
Michele Zappalorto, Italy
Renyun Zhang, Sweden

Contents

Nanomaterials for Energy and Environmental Applications, Sesha Srinivasan, Arunachalanadar M. Kannan, Nikhil Kothurkar, Yehia Khalil, and Sarada Kuravi
Volume 2015, Article ID 979026, 2 pages

A Study of Fuel and Reactor Design for Platinum Nanoparticle Catalyzed Microreactors, Dylan McNally, Marika Agnello, Brigitte Pastore, James R. Applegate, Eric Westphal, and Smitesh D. Bakrania
Volume 2015, Article ID 538752, 8 pages

Evaluation of a Novel Water Treatment Residual Nanoparticles as a Sorbent for Arsenic Removal, Elsayed Elkhatab, Ahmed Mahdy, Fatma Sherif, and Hala Hamadeen
Volume 2015, Article ID 912942, 10 pages

Kinetics, Equilibrium, and Thermodynamics of the Sorption of Bisphenol A onto N-CNTs- β -Cyclodextrin and Fe/N-CNTs- β -Cyclodextrin Nanocomposites, Keletso Mphahlele, Maurice S. Onyango, and Sabelo D. Mhlanga
Volume 2015, Article ID 214327, 13 pages

Experimental Study and Stabilization Mechanisms of Silica Nanoparticles Based Brine Mud with High Temperature Resistance for Horizontal Shale Gas Wells, Xian-yu Yang, Ye Yue, Ji-hua Cai, Yue Liu, and Xiao-ming Wu
Volume 2015, Article ID 745312, 9 pages

Application of Polymeric Nanocomposites and Carbon Fiber Composites in the Production of Natural Gas Reservoirs, Gilberto João Pavani, Sérgio Adalberto Pavani, and Carlos Arthur Ferreira
Volume 2015, Article ID 658727, 7 pages

Editorial

Nanomaterials for Energy and Environmental Applications

**Sesha Srinivasan,¹ Arunachalanadar M. Kannan,² Nikhil Kothurkar,³
Yehia Khalil,⁴ and Sarada Kuravi⁵**

¹Florida Polytechnic University, 4700 Research Way, Lakeland, FL 33805, USA

²The Polytechnic School, Ira A. Fulton Schools of Engineering, Arizona State University, Mesa, AZ 85212, USA

³Department of Chemical Engineering and Materials Science, Amrita Vishwa Vidyapeetham, Amritanagar, Coimbatore 641112, India

⁴United Technologies Research Corporation, 411 Silver Lane, East Hartford, CT 06118, USA

⁵Department of Mechanical and Aerospace Engineering, New Mexico State University, Las Cruces, NM 88003, USA

Correspondence should be addressed to Sesha Srinivasan; ssrinivasan@flpoly.org

Received 19 November 2015; Accepted 23 November 2015

Copyright © 2015 Sesha Srinivasan et al. This is an open access article distributed under the Creative Commons Attribution License, which permits unrestricted use, distribution, and reproduction in any medium, provided the original work is properly cited.

Nanomaterials enabled technologies have been seamlessly integrated into applications such as aviation and space, chemical industry, optics, solar hydrogen, fuel cell, batteries, sensors, power generation, aeronautic industry, building/construction industry, automotive engineering, consumer electronics, thermoelectric devices, pharmaceuticals, and cosmetic industry. Clean energy and environmental applications often demand the development of novel nanomaterials that can provide shortest reaction pathways for the enhancement of reaction kinetics. Understanding the physicochemical, structural, microstructural, surface, and interface properties of nanomaterials is vital for achieving the required efficiency, cycle life, and sustainability in various technological applications. Nanomaterials with specific size and shape such as nanotubes, nanofibers/nanowires, nanocones, nanocomposites, nanorods, nanoislands, nanoparticles, nanospheres, and nanoshells to provide unique properties can be synthesized by tuning the process conditions.

The major objective of this special issue is to bring out the salient research paradigms of nanomaterials and their potential impacts on clean energy generation, storage, utilization, waste heat recovery, environmental detoxification, and disinfection and advocate the process sustainability. The research papers accepted after thorough review process for publication in this issue are briefly narrated below. The potential clean energy and environmental applications where the nanomaterials are employed and reported in this special issue

are for (a) microcombustion and thermoelectric devices, (b) compressed natural gas reservoirs fabrication, (c) high temperature shale well drilling, and (d) water purification by removal of arsenic (V) and bisphenol.

D. McNally et al. reported the design of a thermoelectric device using approximately 8 nm platinum nanoparticles as catalysts for microcombustion applications. The as-developed Pt nanoparticles seem to play a major role in controlling the fuel conversion (in case of ethanol, methane, propane, and butane) and the heat production rate as well. For the fabrication of natural gas reservoirs, it is reported by G. J. Pavani et al. that polymeric nanocomposites tandem with carbon fiber composites (i) improved the strengths of the liner, (ii) reduced the final weight of the reservoir, and (iii) decreased the gas permeability as well. These nanocomposites based compressed natural gas (CNG) reservoirs are potential alternative for vehicular applications. X. Yang et al. have successfully developed stabilization processes of silica nanoparticles based brine muds for the shale gas wells drilling applications. These nanoparticles brine muds (NPBMs) enhanced the mud systems' capabilities such as physical plugging of nanoparticles, balanced chemical activity with inorganic salts (NaCl, KCl, etc.), rational drilling mud density, and the wellbore stability. Other potential applications of water treatment residual nanoparticles (nWTR) as sorbents for the arsenic removal is demonstrated by E. Elkhatib et al. According to the authors, the nWTR consists

of iron, silicon, calcium, and aluminum in either oxide or hydroxide forms. It is claimed that the nWTR showed at least 16 times higher reactivity in arsenic (V) removal when compared to their bulk counterparts. Similar to arsenic removal mentioned above, K. Mphahlele et al. have shown the removal of bisphenol A (BPA) from aqueous solution using Fe/N-CNTs- β -cyclodextrin nanocomposites. All the above research papers are original and are well aligned with the scope of this special issue.

Acknowledgments

We thank all the contributing authors and reviewers for their help in bringing out this special issue. We also thank the editorial board for the smooth process flow and publication.

*Sesha Srinivasan
Arunachalanadar M. Kannan
Nikhil Kothurkar
Yehia Khalil
Sarada Kuravi*

Research Article

A Study of Fuel and Reactor Design for Platinum Nanoparticle Catalyzed Microreactors

Dylan McNally, Marika Agnello, Brigitte Pastore, James R. Applegate, Eric Westphal, and Smitesh D. Bakrania

Mechanical Engineering Department, Rowan University, 201 Mullica Hill Road, Glassboro, NJ 08028, USA

Correspondence should be addressed to Smitesh D. Bakrania; bakrania@rowan.edu

Received 25 August 2015; Revised 3 November 2015; Accepted 12 November 2015

Academic Editor: Nikhil Kothurkar

Copyright © 2015 Dylan McNally et al. This is an open access article distributed under the Creative Commons Attribution License, which permits unrestricted use, distribution, and reproduction in any medium, provided the original work is properly cited.

Typical microcombustion-based power devices entail the use of catalyst to sustain combustion in less than millimeter scale channels. This work explores the use of several other candidate fuels for ~8 nm diameter Pt particle catalyzed combustion within 800 μm channel width cordierite substrates. The results demonstrate while commercial hydrocarbon fuels such as methane, propane, butane, and ethanol can be used to sustain catalytic combustion, room temperature ignition was only observed using methanol-air mixtures. Fuels, other than methanol, required preheating at temperatures $>200^\circ\text{C}$, yet repeated catalytic cycling similar to methanol-air mixtures was demonstrated. Subsequently, a new reactor design was investigated to couple with thermoelectric generators. The modified reactor design enabled ignition of methanol-air mixtures at room temperature with the ability to achieve repeat catalytic cycles. Preliminary performance studies achieved a maximum temperature difference ΔT of 55°C with a flow rate of 800 mL/min. While the temperature difference indicates a respectable potential for power generation, reduced exhaust temperature and improved thermal management could significantly enhance the eventual device performance.

1. Introduction

Microreactors are actively studied for their potential for portable power generation, as documented by a number of exhaustive reviews [1–3]. Their large surface area-to-volume ratios and subsequent heat loss, however, make them susceptible to combustion instabilities and quenching [4]. While several approaches exist to mitigate these design challenges, catalytic combustion has been extensively studied as an effective strategy to address quenching [5]. Typically, metal nanoparticles are used to achieve ignition within submillimeter substrate channels using hydrocarbon fuels [6]. The current focus is on the specific combination of fuel, catalyst, and reactor design to optimize performance [1, 7]. Among the various reactor designs, direct conversion from thermal to electrical power using thermoelectric generators is preferred for its mechanical robustness and size [8, 9]. With thermoelectric power generation governed by temperature differential and thus an effective heat loss from the reactor, thermal management within the reactor becomes a key reactor design parameter [10, 11].

A variety of metal catalysts have been studied to sustain combustion reactions in micron-sized channels. Metal based catalysts are commonly used with nanometer dimensions to enhance reactivity via dramatically increased surface area [12–17]. Studies have also demonstrated Pt nanoparticles as the most active catalytic system when the fuel percent conversion or the fuel ignition behavior is compared [18–21]. Hu et al. [22] and subsequent studies [23–25] have demonstrated room temperature ignition of fuel using Pt nanoparticles. Further enhancements in reactivity can be achieved by alloyed or supported catalysts [26–30]. With respect to the choice of fuels, typically small hydrocarbon fuels or hydrogen [10, 31, 32] has been studied. Hydrocarbon fuels studied include commercially available alkanes such as methane [12, 14, 27, 33, 34], propane [11, 21, 28, 30, 35], and butane [36–38] and simple alcohols such as methanol [29, 39, 40] and ethanol [17, 41, 42]. While simplified catalytic mechanisms have been proposed for various fuels, they are not predictive in terms of their ignition and combustion behavior within microreactors [2, 21, 39, 43]. Most fuels require preheating or hydrogen assistance [43–45] to combat

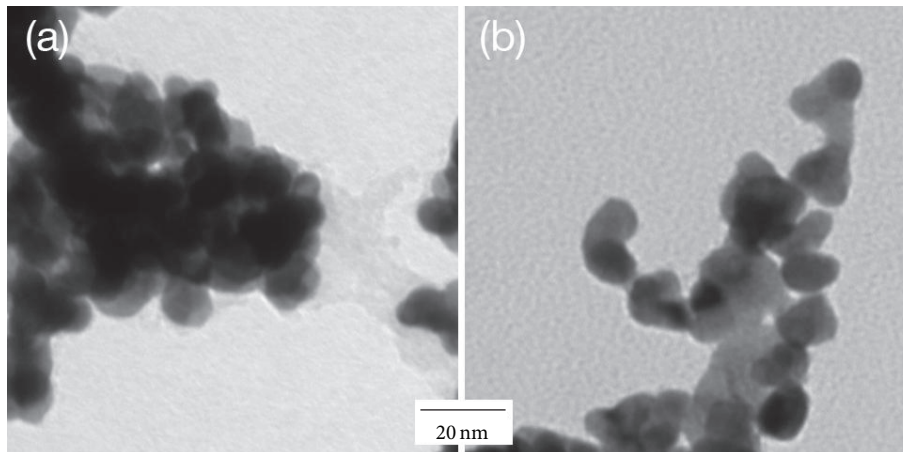


FIGURE 1: TEM images of platinum nanoparticle catalyst material used in combustion studies. Particles were deposited on copper TEM grids for imaging.

reaction quenching. To further ameliorate thermal quenching, a variety of reactor design configurations have been explored, ranging from simple planar [10, 36, 38–40, 46] to counter-flow [11, 20, 47] and Swiss-roll geometries [35]. These and other studies serve as useful guides for catalytic microcombustor design. However, a thorough investigation of thermal design parameters specific to the system is warranted to drive further performance when the reactor designs deviate from the previously explored configurations.

Our previous studies involved catalytic combustion and room temperature ignition of methanol-air mixtures [48, 49]. These studies demonstrated sustained and repeatable methanol combustion using platinum nanoparticles within cordierite substrates. As a next step, this work examines the details of microreactor configuration and explores its dependence on the fuel type using Pt impregnated-cordierite substrate. This work also demonstrates the behavior of different fuels over multiple catalytic cycles. This study highlights the unique combination of factors important to microcombustor-thermoelectric coupled devices.

2. Experimental

2.1. Material Synthesis. Pt nanoparticles were synthesized using a colloidal synthesis technique delineated by Bonet et al. [50] and further specifics detailed elsewhere [48]. The ethylene glycol-based (EG, 99.8% purity, Sigma Aldrich) synthesis incorporated hexachloroplatinic acid precursor (H_2PtCl_6 , ACS reagent grade, Sigma Aldrich) stabilized by polyvinylpyrrolidone (PVP, MW 29,000, Sigma Aldrich). Particles were cleaned through centrifugation using methanol followed by deionized water yielding Pt nanoparticles suspended in water.

XRD analysis confirmed metallic platinum particles were present in the synthesized solution with an average crystallite diameter of 8.9 nm. TEM analysis provided an average primary particle diameter of 8 nm. Figures 1(a) and 1(b) provide TEM images of representative particles with appreciable agglomeration. Particle agglomeration can be attributed to

the drop-coating method used to deposit samples on to TEM grids. It is expected that the particle morphology shown in Figure 1 is representative of deposited particles on catalytic cordierite substrates using draw-coating.

2.2. Substrate Preparation and Reactors. A bulk cordierite monolith was used for uniform nanoparticle distribution and unhindered reactant flow (Corning Inc., 900 cells/in², 800 μm internal channel width). Octagonal substrates 13.5 mm wide and 19 mm long were prepared from the bulk monolith. The substrates were coated with cleaned Pt nanoparticles using a draw-coating method and allowed to dry at ambient conditions. Refer to Applegate et al. [48] for preparation details. This technique deposited a single coating to the base of each channel (estimated to be 10 mg Pt per deposition). The square-channeled substrate was rotated 180°, 90°, and 180° with respect to previous coatings to obtain two, three, and four Pt coated sides, respectively. A layer of quartz wool (0.6–1.6 mm thick) was added around the substrate to prevent reactant bypass through the gap existing between the substrate and the reactor inner wall. Figure 2(c) shows an image of the substrate prepared using the methods described here. The substrate was then inserted within an aluminum reactor. Two reactor configurations were used based on the study parameters. Alternative fuel study used a cylindrical reactor shown in Figures 2(a) and 2(b), while the power device study used a rectangular reactor shown in Figure 2(d) to accommodate the planar thermoelectric generators.

2.3. Alternative Fuel Study. Since previous work focused only on methanol as the reactant fuel, four alternative fuels were explored for Pt-based cyclic catalytic microcombustion. One liquid fuel and three gaseous fuels were investigated as alternatives to liquid methanol. Liquid-phase ethanol ($\geq 99.5\%$ purity, Sigma Aldrich) was combined with synthetic air (99.9% purity, Airgas) via a bubbler assembly. Fuel content in the reactor flow was adjusted to achieve stoichiometric mixtures of fuel and air. A flow controller was

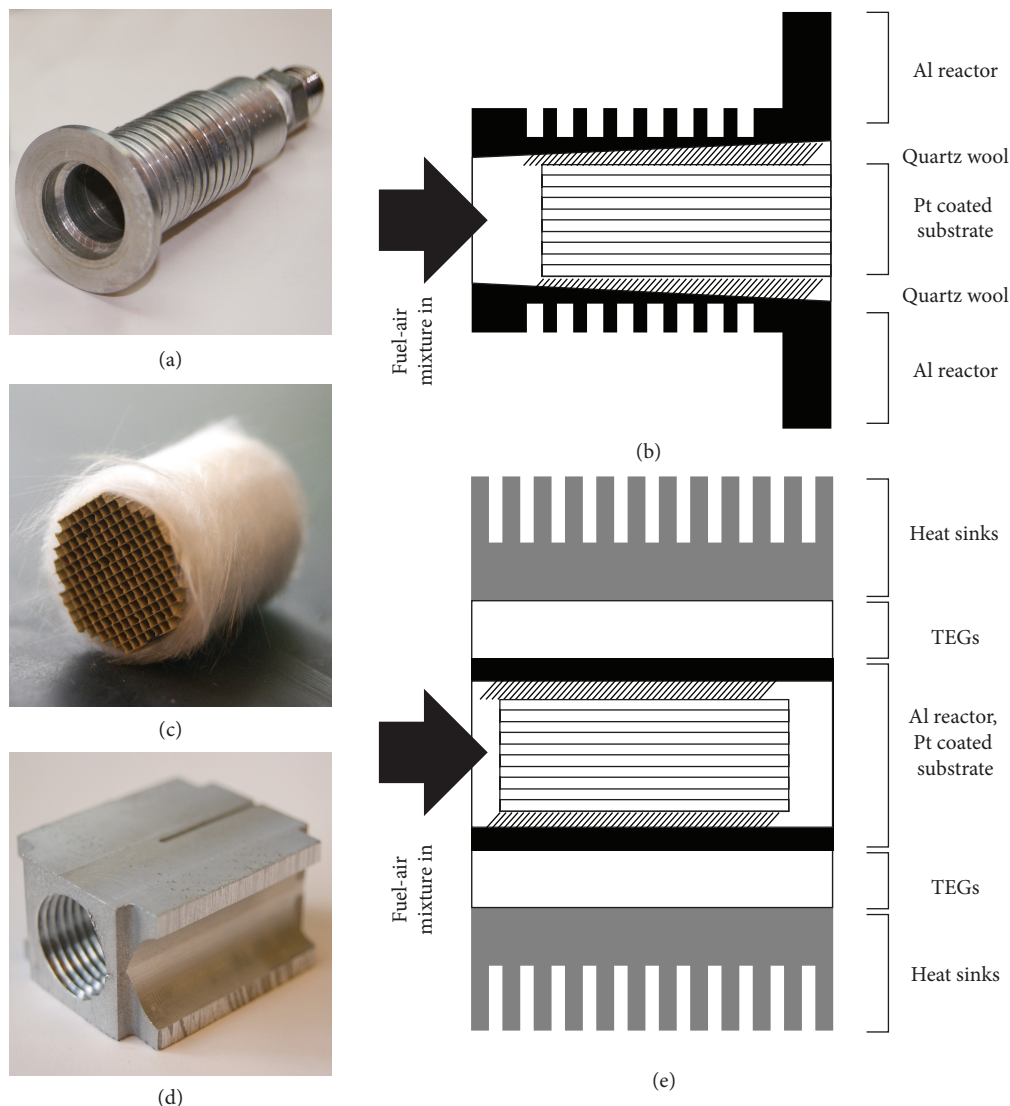


FIGURE 2: Images of (a) the cylindrical reactor used for the alternative fuel study and (d) the rectangular reactor used for the MTC device study. The rectangular reactor was designed to accommodate a (c) catalytic substrate identical to that used in the alternative fuel studies. Cross section schematics show the catalytic substrate inside (b) the cylindrical reactor and (e) microcombustion-thermoelectric coupled (MTC) device assembly. An exhaust tube was added to the rectangular reactor exit. The assembly in (e) schematic represents a top-down view.

used to achieve bubbler inlet flow rates of 800 mL/min and 1000 mL/min. To achieve stoichiometric ethanol-air mixture (based on vapor pressure), the ethanol contained in the bubbler was maintained at 45°C using an oil bath, while the reactor inlet line was maintained at ~105°C to avoid condensation. Gaseous fuels included methane (99% purity, Praxair), propane (99% purity, Praxair), and butane (99.5%, Praxair). The gaseous fuels and air were premixed in the dry bubbler prior to introduction to the reactor at flow rates of 800 mL/min and 1000 mL/min. Preliminary studies, discussed later, indicated the inability of all alternative fuels to ignite without preheating. Preheating of the gaseous fuels involved heating the inlet line using an insulated electrical heater to achieve inlet mixture temperatures of ~210°C.

For the alternative fuel studies, the cylindrical aluminum continuous flow reactor shown in Figures 2(a) and 2(b)

was used. Detailed dimensions and features of the cylindrical reactor were provided previously [48]. The catalyst coated substrate was positioned within the reactor with a K-type thermocouple (KMTXL-020G, Omega Engineering) cemented 7.6 mm deep from the substrate exit into the center channel, hereon referred to as the “substrate temperature.” Temperature data was collected at 10 Hz via a LabView-based DAQ system. Each test comprised three repeat cycles in which heated air and fuel mixtures at the indicated flow rates were introduced in intervals of 30 minutes. All experiments were conducted at atmospheric pressure.

2.4. MTC Device Study. The microcombustion-thermoelectric coupled (MTC) device consisted of three primary components: an aluminum (Al) reactor, thermoelectric generators (TEG’s), and heat sinks. A rectangular reactor shown

in Figure 2(d) was designed to match the planar geometry of the TEGs while keeping a 14.3 mm diameter cylindrical substrate cavity. The reactor was placed between two 1 in² 2.5 W bismuth telluride thermoelectric modules (HZ-2, Hi-Z Technology, Inc.). The Al reactor formed the hot side of the TEGs, while folded sheet-metal computer heat sinks were placed on either side of the two TEGs as cold junctions. A thermal grease (Hi-Z Technology, Inc.) was applied to the TEG faces for improved thermal contact. A constant mechanical compression was maintained for every MTC experiment. K-type thermocouples (KMTXL-020G, Omega Engineering) were used to monitor hot- and cold-side temperatures as well as the substrate temperature using LabView-based DAQ. In addition, exhaust product gas temperature was monitored to account for heat loss. Figure 2(e) provides a complete schematic of the MTC assembly. The schematic is a cross section top view of the MTC device. The orientation was selected to optimize convective heat transfer from the heat sinks.

Material and substrate preparation methods described earlier were used to produce the catalytic substrate shown in Figure 2(c). All MTC device tests were conducted using methanol (99.8% purity, Sigma Aldrich) as the reactant fuel introduced by bubbling synthetic air through a glass bubbler. Previous work has demonstrated such a process to yield near stoichiometric mixture of methanol and air. Air flow rates ranged from 400 mL/min to 800 mL/min. A threaded exhaust tube was screwed into the reactor outlet to secure the substrate and to reduce exhaust heat loss. Experiments were conducted at ambient conditions by introducing the reactants into the microcombustor which subsequently ignited to provide a stable heat source for the TEGs to produce power.

3. Results and Discussion

3.1. Alternative Fuel Study. Our previous work has already demonstrated successful room temperature ignition of methanol-air mixture with platinum nanoparticles [48]. Furthermore, this previous work has presented the effect of reactant flow rate and mass loading (in the form of a number of coated sides) on the catalytic performance of the microreactor. Therefore, the selected test parameters for the alternative fuel study were based on previous trends observed with methanol-air mixtures. Figure 3 shows the Pt coated substrate undergoing a single catalytic combustion of methanol within the cylindrical reactor. As the resulting glow suggests, heat generation is concentrated in the center core of the substrate; subsequent temperature measurements at radial locations have indicated <10% drop in average temperatures from the substrate center. This is in contrast to the axial locations that demonstrate a more dramatic reduction of ~35% in temperature when inlet temperatures are compared to the outlet temperatures within the center channel, a feature that is common with low conductivity substrates [31]. While thermal map of the substrate is sufficiently described here, additional temperature and ignition time mapping studies are reported elsewhere [51].

As opposed to methanol ignition at room temperature, preliminary tests conducted using ethanol, methane,

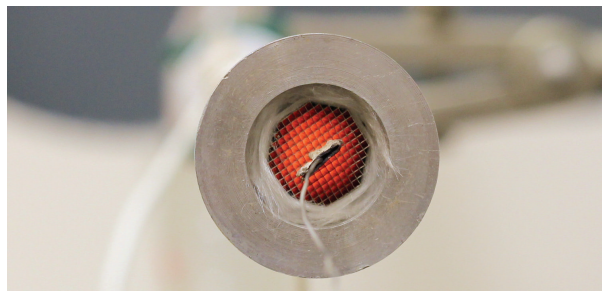


FIGURE 3: Cylindrical reactor exit showing cordierite substrate undergoing catalytic combustion with methanol-air mixture. Image shows a thermocouple probe cemented within the center channel to measure the substrate temperature.

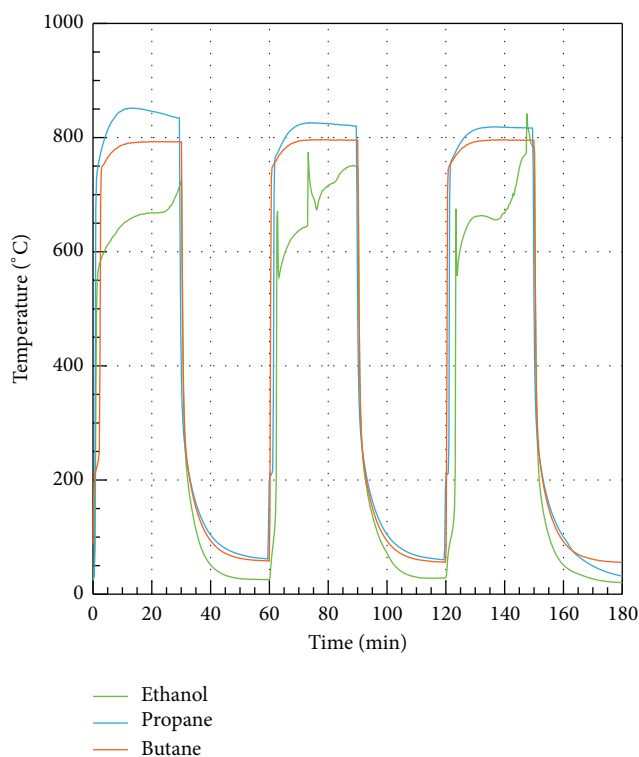


FIGURE 4: Temperature histories of ethanol, propane, and butane undergoing catalytic combustion cycles. Tests were conducted with preheated inlet at ~210°C and reactant flow rate of 800 mL/min. Two-sided Pt coated substrates used for these tests.

propane, and butane failed to ignite at room temperature. Ethanol, in particular, as the only liquid-phase alternative to methanol, yielded fuel-lean mixtures at room temperature and failed to ignite. For combustion to proceed, the ethanol flask was submerged in an oil bath maintained at 45°C and the reactor inlet line was heated to 105°C to maintain near stoichiometric mixtures. The gaseous fuels, methane, propane, and butane, were preheated to achieve ignition. Preheating was achieved using a resistive heating wire to raise the inlet reactant temperatures up to ~210°C. It is important to note that the preheating temperature is appreciably higher than individual fuel light-off temperatures. Figure 4 provides representative results of catalysis experiments conducted

TABLE 1: Alternative fuel study using preheated inlet results summary. Ethanol reservoir was maintained at 45°C.

Fuel	Fuel-air flow rate [mL/min]	Avg. peak temp. [°C]	Avg. time const. [s]	Heat production rate [W] based on LHV
Ethanol	800	667 ± 59	—	677
Methane	1000	740 ± 6.8	14.6	547
Propane	800	820 ± 22	10.1	1113
Butane	800	790 ± 9.1	13.9	1435

for ethanol, propane, and butane flowing at 800 mL/min with two-sided Pt coated substrates. Methane results were excluded from Figure 4 because only a single catalytic cycle was observed at the higher flow rate of 1000 mL/min. The need for thermal activation for these fuels is in agreement with similar studies of various Pt catalytic combustion systems [12, 19, 21, 28, 30, 31, 41].

Figure 4 shows catalytic cycling and relatively constant peak temperatures for propane and butane fuels consistent with previous methanol studies. Ethanol, however, demonstrated unstable catalytic combustion temperatures. In other words, while catalytic cycling similar to methanol can be achieved with propane, butane and ethanol, preheating is necessary to achieve light-off at room temperature. Results in Figure 4 are representative of multiple runs conducted with each fuel. In order to discuss quantitative trends, Table 1 lists the average peak temperature, time constant, and heat production rate for each fuel. The average peak temperature is defined as the average of temperature data after reaching 95% of the peak cycle value. The average and standard deviation of peak temperatures for each fuel were evaluated for three cycles within a test. The mean time constants for each fuel ignition were similarly calculated. The analysis was performed using a MATLAB algorithm. Table 1 includes a theoretical estimate of heat production rate based on the assumption that 100% of the fuel is converted to products. Standard Lower Heating Values (LHV) found in combustion literature were used for comparison. Table 1 shows propane attained the highest average temperature of combustion at $820 \pm 22^\circ\text{C}$, while the lowest average temperature was achieved by ethanol at $667 \pm 59^\circ\text{C}$. These trends do not correlate with the heat production rate, suggesting fuel-specific interaction with platinum nanoparticles that potentially controls fuel conversion and in turn heat production rate. A fuel conversion rate study as a function of fuel type is required to thoroughly explain the observed trends. While the alternative fuel study established methanol as the fuel of choice for its ability to combust from room temperature, one can easily integrate the alternative fuels in self-preheating reactor configurations or with hydrogen blended ignition considering that ethanol, propane, and butane successfully yielded the cyclical catalytic combustion desired for an MTC device.

3.2. MTC Device Study. In development of the MTC device, the design requirements were governed by existing and previously tested cordierite-based octagonal catalytic substrate. Therefore, to maximize potential power output, according to

the previous study [48] substrates with 4-coated sides were primarily used instead of substrates with 2-coated sides used in the alternative fuel study. As a reminder, all MTC device studies utilized near stoichiometric methanol-air mixtures for performance tests. TEG modules that best matched the substrate dimensions were selected. The aluminum reactor dimensions and geometry were dependent on both the substrate and TEG devices, at the same time minimizing thermal mass of the system. Large reactor thermal mass prompts quenching due to excessive heat loss at the heterogeneous combustion stage, eventually requiring reactant preheating. Considering a theoretical model of the ignition characteristics and the quenching mechanisms that are challenging to develop for such a system, a combination of steady state thermal simulations and empirical results were used to guide the final design. A substrate placement location study was conducted to determine the optimal substrate position for uniform temperatures on the “hot side” of the TEG modules. Simulations concluded that a substrate located closer to the fuel-air mixture inlet was ideal. The location, verified by experiments, yielded reactor surface temperatures that were within 10°C of each other. In addition, three heat sink pairs (with 3.5 cm, 8 cm, and 15 cm contact widths) were tested for combustion stability and the temperature difference across the TEGs. Analogous to the reactor thermal mass discussion, the large 15 cm heat sinks promoted quenching, while the smaller heat sinks yielded minimal temperature difference across the TEG modules. As a result 8 cm heat sinks were selected for the MTC device. The final MTC device included a 7.6 cm long aluminum exhaust tube attached to the reactor outlet, which was shown to increase substrate temperature by $\sim 50^\circ\text{C}$.

Figure 5 presents representative temperature histories from thermocouple probes placed at key locations (namely, two hot- and cold-side temperatures, exhaust temperature, and the substrate temperature) within the final MTC device during a preliminary test to assess device performance. With a flow rate of 400 mL/min, this substrate with two-coated sides experiences the highest substrate temperature that stabilizes within ~ 7 min of operation. The substrate maintains the high substrate temperature of 500°C before returning to room temperature as the reactant mixture supply is stopped. The device symmetry is evident from the pair of hot-side and cold-side temperature profiles in Figure 5. The pair of hot- and cold-side temperatures directly overlap each other. The temperature difference between the hot-side and the cold-side temperature is defined as the TEG temperature difference ΔT , and that drives thermoelectric conversion. Considering

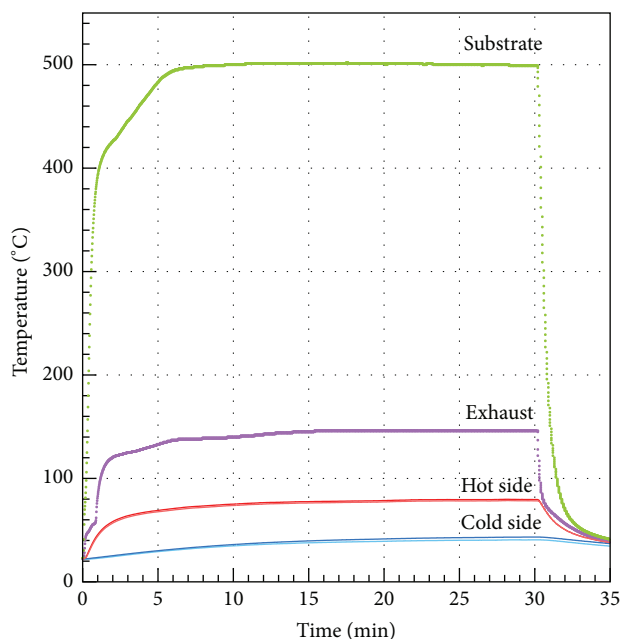


FIGURE 5: A single catalytic cycle of a typical methanol-air run showing temperatures of substrate, the two hot and cold sides, and the exhaust. Experiment conducted with flow rate 400 mL/min and 2 single coated sides.

an MTC device that operates at steady conditions, ΔT at the end of a cycle is a reasonable metric to estimate device performance. Figure 5 also provides the product gas exhaust temperature which is noticeably higher than the hot-side temperature, indicating the future potential for harvesting the heat energy or using the exhaust heat for reactant flow preheat. Alternatively, the substrate temperature can be raised by increasing the flow rate through the substrate resulting in higher heat production rate due to an increase in reactant mixture content.

Figure 6 provides a summary of ΔT as a function of reactant flow rate. ΔT represent the mean temperature difference between the hot-side and the cold-side temperatures of a pair of TEGs over three consecutive catalytic cycles. The error bars represent a single standard deviation within the data subset. As indicated in Figure 6 the ΔT increases with increasing reactant flow rate up to $\sim 60^\circ\text{C}$ with 800 mL/min. The increase in ΔT can be explained by the increased heat release as documented by our previous work [48]. Due to system limitations, thermoelectric conversion performance was not conducted with these experiments. Instead, theoretical values for potential power output based on TEG module specifications and operational parameters (such as TEG temperature and ΔT) were obtained and plotted alongside. Calculations used a Seebeck coefficient of $200 \mu\text{V K}^{-1}$ provided by the manufacturer. Figure 6 indicates the maximum power output at 300 mW for the highest flow rate. Considering the methanol LHV and the flow rate, the thermal conversion efficiency of the system is estimated at 0.1%. While this value is low in comparison to hydrocarbon based power production, the state-of-the-art conversion efficiencies for microcombustion-TEG power

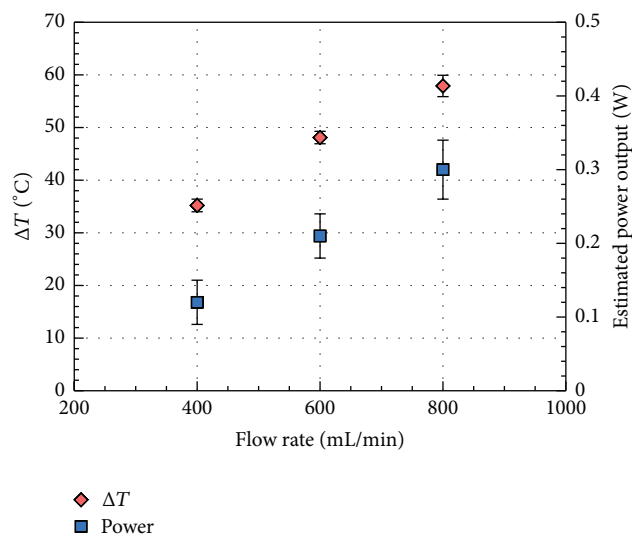


FIGURE 6: Average temperature difference ΔT between hot and cold sides of a TEG plotted as a function of methanol-air flow rates. Substrate was coated on 4 sides. Error bars represent a single standard deviation. Secondary axis maps methanol-air flow rate to theoretical estimate of potential power production.

devices are in the range of 2-3% [36, 38, 39, 46]. Furthermore, a number of parameters remain to be optimized within the MTC device that minimizes exhaust gas temperature and maximizes the ΔT . The critical design parameters that can drive further enhancements include improved substrate-reactor geometry match, custom heat sink design, optimized reactant residence time, and exhaust heat management, to name a few. Already, the extension of the substrate length has demonstrated notable improvement in fuel conversion (methanol-conversion is estimated at 60% for the substrates used in these studies). Further investigation on the reactant flows, as investigated by Leu et al. [47], is warranted for achieving higher fuel conversion rates.

4. Conclusion

This work provided important experimental results on design of a microcombustion-thermoelectric power device using Pt nanoparticles as the catalyst. The alternative fuel study demonstrated methanol-air mixture as the ideal fuel of choice if a self-starting device is desired. At the same time, the ethanol, propane, and butane can be used in catalytic microcombustion if preheating or an ignition source is integrated. The new reactor design provided a functional device with the ability to achieve repeatable catalytic cycles. While the efficiency of the new reactor is low, this work indicated multiple aspects of the design that can be modified to enhance performance. The results elucidate important influencing factors for further optimization of the thermal design. More importantly, the results provide a viable template towards a highly miniaturized design for a microcombustion-thermoelectric coupled power device.

Conflict of Interests

The authors declare that there is no conflict of interests regarding the publication of this paper.

Acknowledgments

The authors would like to thank Thomas Barkley for his assistance with TEM imaging and Brad Johnson for developing the MATLAB algorithm for analysis. Reactor fabrication was assisted by Charles Linderman. The authors also appreciate past contributions by Dr. Howard Pearlman on the initial development of this project.

References

- [1] A. C. Fernandez-Pello, "Micropower generation using combustion: issues and approaches," *Proceedings of the Combustion Institute*, vol. 29, pp. 883–899, 2002.
- [2] K. Maruta, "Micro and mesoscale combustion," *Proceedings of the Combustion Institute*, vol. 33, no. 1, pp. 125–150, 2011.
- [3] N. S. Kaisare and D. G. Vlachos, "A review on microcombustion: fundamentals, devices and applications," *Progress in Energy and Combustion Science*, vol. 38, no. 3, pp. 321–359, 2012.
- [4] S. Karagiannidis, J. Mantzaras, G. Jackson, and K. Boulouchos, "Hetero-/homogeneous combustion and stability maps in methane-fueled catalytic micro-reactors," *Proceedings of the Combustion Institute*, vol. 31, no. 2, pp. 3309–3317, 2007.
- [5] Y. Ju and K. Maruta, "Microscale combustion: technology development and fundamental research," *Progress in Energy and Combustion Science*, vol. 37, no. 6, pp. 669–715, 2011.
- [6] E. L. Dreizin, "Metal-based reactive nanomaterials," *Progress in Energy and Combustion Science*, vol. 35, no. 2, pp. 141–167, 2009.
- [7] A. Mitsos, B. Chachuat, and P. I. Barton, "What is the design objective for portable power generation: efficiency or energy density?" *Journal of Power Sources*, vol. 164, no. 2, pp. 678–687, 2007.
- [8] S. Leblanc, S. K. Yee, M. L. Scullin, C. Dames, and K. E. Goodson, "Material and manufacturing cost considerations for thermoelectrics," *Renewable and Sustainable Energy Reviews*, vol. 32, pp. 313–327, 2014.
- [9] S. LeBlanc, "Thermoelectric generators: linking material properties and systems engineering for waste heat recovery applications," *Sustainable Materials and Technologies*, vol. 1-2, pp. 26–35, 2014.
- [10] J. Zhou, Y. Wang, W. Yang, J. Liu, Z. Wang, and K. Cen, "Combustion of hydrogen-air in catalytic micro-combustors made of different material," *International Journal of Hydrogen Energy*, vol. 34, no. 8, pp. 3535–3545, 2009.
- [11] J. A. Federici and D. G. Vlachos, "A computational fluid dynamics study of propane/air microflame stability in a heat recirculation reactor," *Combustion and Flame*, vol. 153, no. 1-2, pp. 258–269, 2008.
- [12] R. Abbasi, L. Wu, S. E. Wanke, and R. E. Hayes, "Kinetics of methane combustion over Pt and Pt-Pd catalysts," *Chemical Engineering Research and Design*, vol. 90, no. 11, pp. 1930–1942, 2012.
- [13] C. Lee, H.-K. Yoon, S.-H. Moon, and K. J. Yoon, "Methanol decomposition over supported palladium and platinum," *Korean Journal of Chemical Engineering*, vol. 15, no. 6, pp. 590–595, 1998.
- [14] J. Li, J. Zhang, Z. Lei, and B. Chen, "Pd-Co coating onto cordierite monoliths as structured catalysts for methane catalytic combustion," *Energy and Fuels*, vol. 26, no. 1, pp. 443–450, 2012.
- [15] M. Lyubovsky, L. L. Smith, M. Castaldi et al., "Catalytic combustion over platinum group catalysts: fuel-lean versus fuel-rich operation," *Catalysis Today*, vol. 83, no. 1-4, pp. 71–84, 2003.
- [16] X. Ma, L. Liu, N. Aronhime, and M. R. Zachariah, "Ignition catalyzed by unsupported metal nanoparticles," *Energy & Fuels*, vol. 25, no. 9, pp. 3925–3933, 2011.
- [17] J. R. Salge, G. A. Deluga, and L. D. Schmidt, "Catalytic partial oxidation of ethanol over noble metal catalysts," *Journal of Catalysis*, vol. 235, no. 1, pp. 69–78, 2005.
- [18] W. M. Yang, S. K. Chou, C. Shu, Z. W. Li, and H. Xue, "Study of catalytic combustion and its effect on microthermophotovoltaic power generators," *Journal of Physics D: Applied Physics*, vol. 38, no. 23, pp. 4252–4255, 2005.
- [19] L. Kiwi-Minsker, I. Yuranov, E. Slavinskaia, V. Zaikovskii, and A. Renken, "Pt and Pd supported on glass fibers as effective combustion catalysts," *Catalysis Today*, vol. 59, no. 1-2, pp. 61–68, 2000.
- [20] M. J. Lee and N. I. Kim, "Experiment on the effect of Pt-catalyst on the characteristics of a small heat-regenerative CH₄-air premixed combustor," *Applied Energy*, vol. 87, no. 11, pp. 3409–3416, 2010.
- [21] Y. Men, G. Kolb, R. Zapf, H. Pennemann, and V. Hessel, "Total combustion of propane in a catalytic microchannel combustor," *Chemical Engineering Research and Design*, vol. 87, no. 1, pp. 91–96, 2009.
- [22] Z. Hu, V. Boiadjiev, and T. Thundat, "Nanocatalytic spontaneous ignition and self-supporting room-temperature combustion," *Energy and Fuels*, vol. 19, no. 3, pp. 855–858, 2005.
- [23] Y. Ma, C. Ricciuti, T. Miller, J. Kadlowec, and H. Pearlman, "Enhanced catalytic combustion using sub-micrometer and nano-size platinum particles," *Energy & Fuels*, vol. 22, no. 6, pp. 3695–3700, 2008.
- [24] A. M. Moreno and B. A. Wilhite, "Autothermal hydrogen generation from methanol in a ceramic microchannel network," *Journal of Power Sources*, vol. 195, no. 7, pp. 1964–1970, 2010.
- [25] X. Luo, Z. Zeng, X. Wang et al., "Preparing two-dimensional nano-catalytic combustion patterns using direct inkjet printing," *Journal of Power Sources*, vol. 271, pp. 174–179, 2014.
- [26] T. Sanders, P. Papas, and G. Veser, "Supported nanocomposite catalysts for high-temperature partial oxidation of methane," *Chemical Engineering Journal*, vol. 142, no. 1, pp. 122–132, 2008.
- [27] I. E. Beck, V. I. Bukhtiyarov, I. Y. Pakharukov, V. I. Zaikovskiy, V. V. Kriventsov, and V. N. Parmon, "Platinum nanoparticles on Al₂O₃: correlation between the particle size and activity in total methane oxidation," *Journal of Catalysis*, vol. 268, no. 1, pp. 60–67, 2009.
- [28] M.-Y. Kim, S. M. Park, G. Seo, and K.-S. Song, "Highly stable platinum catalysts in propane combustion prepared by supporting platinum on zirconia-incorporated silica," *Catalysis Letters*, vol. 138, no. 3-4, pp. 205–214, 2010.
- [29] A. Wan and C.-T. Yeh, "Ignition of methanol partial oxidation over supported platinum catalyst," *Catalysis Today*, vol. 129, no. 3-4, pp. 293–296, 2007.
- [30] H. Yoshida, Y. Yazawa, and T. Hattori, "Effects of support and additive on oxidation state and activity of Pt catalyst in propane combustion," *Catalysis Today*, vol. 87, no. 1-4, pp. 19–28, 2003.

- [31] V. Seshadri and N. S. Kaisare, "Simulation of hydrogen and hydrogen-assisted propane ignition in pt catalyzed microchannel," *Combustion and Flame*, vol. 157, no. 11, pp. 2051–2062, 2010.
- [32] F. Wang, J. Zhou, G. Wang, and X. Zhou, "Simulation on thermoelectric device with hydrogen catalytic combustion," *International Journal of Hydrogen Energy*, vol. 37, no. 1, pp. 884–888, 2012.
- [33] A. Di Benedetto, G. Landi, V. Di Sarli, P. S. Barbato, R. Pirone, and G. Russo, "Methane catalytic combustion under pressure," *Catalysis Today*, vol. 197, no. 1, pp. 206–213, 2012.
- [34] S. A. Smyth and D. C. Kyritsis, "Experimental determination of the structure of catalytic micro-combustion flows over small-scale flat plates for methane and propane fuel," *Combustion and Flame*, vol. 159, no. 2, pp. 802–816, 2012.
- [35] J. Ahn, C. Eastwood, L. Sitzki, and P. D. Ronney, "Gas-phase and catalytic combustion in heat-recirculating burners," *Proceedings of the Combustion Institute*, vol. 30, pp. 2463–2472, 2005.
- [36] K. Yoshida, S. Tanaka, S. Tomonari, D. Satoh, and M. Esashi, "High-energy density miniature thermoelectric generator using catalytic combustion," *Journal of Microelectromechanical Systems*, vol. 15, no. 1, pp. 195–203, 2006.
- [37] R. J. Bass, T. M. Dunn, Y.-C. Lin, and K. L. Hohn, "Syn-gas production from catalytic partial oxidation of n-butane: comparison between incipient wetness and sol-gel prepared Pt/Al₂O₃," *Industrial and Engineering Chemistry Research*, vol. 47, no. 19, pp. 7184–7189, 2008.
- [38] C. H. Marton, G. S. Haldeman, and K. F. Jensen, "Portable thermoelectric power generator based on a microfabricated silicon combustor with low resistance to flow," *Industrial & Engineering Chemistry Research*, vol. 50, no. 14, pp. 8468–8475, 2011.
- [39] A. M. Karim, J. A. Federici, and D. G. Vlachos, "Portable power production from methanol in an integrated thermoelectric/microreactor system," *Journal of Power Sources*, vol. 179, no. 1, pp. 113–120, 2008.
- [40] D. Resnik, S. Hočevar, J. Batista, D. Vrtačnik, M. Možek, and S. Amon, "Si based methanol catalytic micro combustor for integrated steam reformer applications," *Sensors and Actuators A: Physical*, vol. 180, pp. 127–136, 2012.
- [41] S.-N. Hsu, J.-L. Bi, W.-F. Wang, C.-T. Yeh, and C.-B. Wang, "Low-temperature partial oxidation of ethanol over supported platinum catalysts for hydrogen production," *International Journal of Hydrogen Energy*, vol. 33, no. 2, pp. 693–699, 2008.
- [42] L. V. Mattos and F. B. Noronha, "Partial oxidation of ethanol on supported Pt catalysts," *Journal of Power Sources*, vol. 145, no. 1, pp. 10–15, 2005.
- [43] B.-J. Zhong and F. Yang, "Characteristics of hydrogen-assisted catalytic ignition of n-butane/air mixtures," *International Journal of Hydrogen Energy*, vol. 37, no. 10, pp. 8716–8723, 2012.
- [44] Y. Yan, W. Tang, L. Zhang, W. Pan, and L. Li, "Thermal and chemical effects of hydrogen addition on catalytic micro-combustion of methane-air," *International Journal of Hydrogen Energy*, vol. 39, no. 33, pp. 19204–19211, 2014.
- [45] O. Deutschmann, L. I. Maier, U. Riedel, A. H. Stroemman, and R. W. Dibble, "Hydrogen assisted catalytic combustion of methane on platinum," *Catalysis Today*, vol. 59, no. 1-2, pp. 141–150, 2000.
- [46] J. A. Federici, D. G. Norton, T. Brüggemann, K. W. Voit, E. D. Wetzel, and D. G. Vlachos, "Catalytic microcombustors with integrated thermoelectric elements for portable power production," *Journal of Power Sources*, vol. 161, no. 2, pp. 1469–1478, 2006.
- [47] C.-H. Leu, S.-C. King, J.-M. Huang et al., "Visible images of the catalytic combustion of methanol in a micro-channel reactor," *Chemical Engineering Journal*, vol. 226, pp. 201–208, 2013.
- [48] J. R. Applegate, H. Pearlman, and S. D. Bakrania, "Catalysis of methanol-air mixture using platinum nanoparticles for microscale combustion," *Journal of Nanomaterials*, vol. 2012, Article ID 460790, 8 pages, 2012.
- [49] J. R. Applegate, D. McNally, H. Pearlman, and S. D. Bakrania, "Platinum-nanoparticle-catalyzed combustion of a methanol-air mixture," *Energy & Fuels*, vol. 27, no. 7, pp. 4014–4020, 2013.
- [50] F. Bonet, V. Delmas, S. Grugeon, R. H. Urbina, P.-Y. Silvert, and K. Tekaia-Elhissien, "Synthesis of monodisperse Au, Pt, Pd, Ru and Ir nanoparticles in ethylene glycol," *Nanostructured Materials*, vol. 11, no. 8, pp. 1277–1284, 1999.
- [51] E. Westphal and S. D. Bakrania, "Investigating Pt-based micro-combustor performance for portable power device," in *Proceedings of the ASME International Mechanical Engineering Congress & Exposition (IMECE '14)*, American Society of Mechanical Engineers, Montreal, Canada, 2014.

Research Article

Evaluation of a Novel Water Treatment Residual Nanoparticles as a Sorbent for Arsenic Removal

Elsayed Elkhatib, Ahmed Mahdy, Fatma Sherif, and Hala Hamadeen

Department of Soil and Water Sciences, Alexandria University, Alexandria 21545, Egypt

Correspondence should be addressed to Elsayed Elkhatib; selkhatib1@yahoo.com

Received 24 August 2015; Revised 20 September 2015; Accepted 21 September 2015

Academic Editor: Sesha Srinivasan

Copyright © 2015 Elsayed Elkhatib et al. This is an open access article distributed under the Creative Commons Attribution License, which permits unrestricted use, distribution, and reproduction in any medium, provided the original work is properly cited.

A novel sorbent, water treatment residual nanoparticles (nWTR), was synthesized and used to remove As(V) from water solutions. The kinetics and equilibrium of As(V) adsorption by nWTR were evaluated. The kinetic data for nWTR at 3 different pH values indicate that As(V) sorption is biphasic, is favored at low pH values, and followed the power function and first-order kinetics models fit. The results of the batch adsorption study showed that nWTR was effective in As(V) removal and its removal capability was 16 times higher than that of bulk WTR. Fourier transmission infrared (FTIR), SEM-EDX spectra, and As fractionation results indicate the crucial role of surface hydroxyl groups in As retention onto nWTR and the high capability of nWTR to immobilize As(V). The stability of As-nWTR surface complexes is suggested as less than 2% of adsorbed As(V) was released from nWTR after 4 consecutive desorption cycles.

1. Introduction

Arsenic (As) is listed in the US-EPA priority pollutant list with known adverse effects on humans and environment health. Land application of As based pesticides and biosolids, disposal of industrial wastes, and mining activities are the major sources of anthropogenic arsenic in soil and water ecosystems. The strong ability of As to accumulate in food chains can lead to living organisms' toxicity and pose greater risks to our health and the environment [1, 2].

Several remediation technologies are available to reduce As concentrations in soil and water systems high in As [3–6]. However, many of these technologies have shown limitations in removing the toxic contaminants from contaminated water to safe levels and they are costly, laborious, and time-consuming [7, 8]. Research on the development of inexpensive and green remediation techniques remains a challenge.

Water treatment residuals (WTRs), waste products from drinking water treatment facilities, have been gaining increased attention recently as an ecofriendly and low cost adsorbent. Because of their amorphous nature, WTRs have shown strong affinity for P, As, Ni, Cu, and Pb [9–13].

Moreover, conclusive prior studies have demonstrated that the smaller fraction of WTR greatly influences its active surface area and leads to increase its adsorption capacity [12–14]. Recently, Elkhatib et al. [13] developed a method to produce nanoparticles sorbent from water treatment residues using precision milling. They reported that the P sorption capacity of the produced nanoparticles was 30 times higher than the P sorption capacity of bulk water treatment residuals. The comparatively greater adsorption capacity and stability of water treatment residual nanoparticles (nWTR) suggest their use as a very promising and practical solution to remediate various environmental contaminants. For the best of our knowledge, information is not available in the literature on the potential use of nanoscale WTRs in removal of arsenic from aqueous media. The objectives of this study were to (1) determine arsenic adsorption capacity of water treatment residual nanoparticles and to investigate the pertinent adsorption mechanism and (2) study the effects of operational parameters including adsorbent dosages, solution pH, and coexisting cations on the removal of As by nWTR. Such a study is important for practical guidance and for gaining future acceptance in utilizing nWTR as a remediation agent for waste water and freshwater.

2. Experimental

2.1. Synthesis and Characterization of nWTR. The bulk WTR (mWTR) was obtained from the drinking water treatment plant in Kafr El-Dawar, El Beheira, Egypt. The plant uses aluminum sulfate for flocculation. The WTR samples were collected, transported to the laboratory, and air-dried. Sub-samples were ground and passed through two different sieves having 2 mm (mWTR) and 51 μm (μWTR) of pore diameters. Synthesis of nanoscale WTR was achieved by milling subsamples of μWTR (<51 μm) using Fritsch Planetary Mono Mill [13]. The characteristics and element contents of nWTR, mWTR, and μWTR were investigated using transmission electron microscopy (TEM), X-ray diffraction (XRD), scanning electron microscopy (SEM) with energy dispersive X-ray (INCAx-Sight model 6587, Oxford Instruments, UK), and autosorb iQ surface area analyzer (Quantachrome, USA) and the results have been reported elsewhere [15].

2.2. Adsorption Kinetics. Adsorption kinetic experiments were carried out at room temperature (23°C) using the batch technique. A dose of nWTR (100 mg) and 20 mL of As(V) solutions with the initial concentration of 350 mg/L were placed in 50 mL centrifuge tubes and shaken using an end-over-end shaker for different time intervals (5 min–24 h) at 3 different pH levels (pH 5, 7, and 9). The pH of each suspension was kept constant by adding HCl or NaOH using the automatic titrator. The As-nWTR suspensions were centrifuged at 4000 rpm for 10 min and the supernatant solutions were filtered through a membrane filter (0.45 μm ; Millipore Corp.). The concentrations of As in the supernatant solutions were analyzed by the atomic absorption spectrometry method (AAS, Perkin Elmer Optima 2000 DV). Arsenic(V) solutions were prepared from stock standard Na_2HAsO_4 solution (1000 mgL^{-1}). The kinetics of As adsorption on the nWTR samples was investigated by fitting the sorption data to power function, parabolic diffusion, first-order, and Elovich kinetic models.

2.3. Adsorption Isotherms. Arsenic(V) sorption equilibrium studies were performed on three sizes of WTR (2 mm (bulk WTR), <51 micron (μWTR), and <100 nm (nWTR)) at As(V) concentrations ranging from 0 to 160 mg/L. The adsorption studies were conducted at normal pH (7.2) using 0.01 M K_2SO_4 as background electrolyte. The WTR-As mixtures were equilibrated on an end-over-end shaker for 24 h (pre-determined equilibrium adsorption time) and centrifuged at 4000 rpm for 10 min and the supernatant solutions were filtered through a membrane filter (0.45 μm ; Millipore Corp.). All experiments were performed in triplicate, and solutions were analyzed for As by AAS. The sorption data were then fitted to seven different isotherm models and the best fit model was used to calculate the maximum sorption capacity [15]. The solid nWTR material used in these sorption experiments was recovered and examined for sorbed As via scanning electron microscopy (SEM), equipped with an X-ray energy dispersive spectrometer (SEM-XED).

The effect of pH on As(V) adsorption by nanoscale WTR was studied in the pH range of 3–11 at room temperature. A dose of nWTR (0.1 g) and 20 mL of As(V) solutions with the initial concentration of 150 mg/L were placed in 50 mL centrifuge tubes and shaken using an end-over-end shaker for 15 min at different pH levels (3–11). The pH of each suspension was kept constant by adding HCl or NaOH using the automatic titrator. The As-nWTR suspensions were centrifuged at 4000 rpm for 10 min and the supernatant solutions were filtered through 0.45 μm Millipore membrane filters. The concentrations of As in the supernatant solutions were analyzed by AAS.

For the determination of optimal dosage of nWTR, three masses (0.02, 0.05, and 0.10 g) were shaken with 10 mL each of different As(V) concentrations (0–500 mgL^{-1}) contained in 50 mL centrifuge tubes for 24 h using end-over-end shaker. The suspensions were then centrifuged at 4000 rpm for 10 min and the supernatant solutions were filtered.

The effect of initial As(V) concentration on the extent of adsorption was investigated at the initial As concentrations of 5, 20, 40, 80, and 160 mg/L. The experiments were performed by adding 0.10 g of nWTR sample to 20 mL of As solutions. The mixtures were shaken on the orbital shaker for 24 h and then removed for centrifugation. After centrifugation, the supernatant solutions were transferred into clean tubes and kept under refrigeration (–4°C) until analysis. To evaluate the effect of coexisting ions on As adsorption by nWTR, similar set of experiments were performed in the presence of two competing cations (Hg and Cr) at concentrations equal to As(V) concentration. All experiments were performed in triplicate, and solutions were analyzed for As by AAS.

3. Results and Discussion

3.1. Characterization of nWTR. The SEM analysis of nWTR samples showed that the WTR nanoparticles are spherical with sizes in the range of 45 to 96 nm and the EDX analysis revealed the prominence of iron, silicon, calcium, and aluminum in nWTR (Figure 1(a)). The X-ray diffraction analysis (Figure 2) confirmed EDX results and ascertained amorphous iron, aluminum (hydr)oxides, and silicon oxide dominating all nWTR, with no apparent crystalline iron-Al (hydr)oxides. The SEM images of nWTR before and after saturation with As ions are shown in Figures 1(a) and 1(b). The figures showed a coating layer of adsorbed arsenic on the surface of the nWTR after arsenic adsorption. The SEM-EDX analysis spectrum (Figure 1(b)) ascertained the appearance of As peak (7.52%) amongst the elements detected in As-saturated nWTR. An important feature of the EDX results is a clear reduction in the intensity of the iron peak in the As-saturated nWTR which suggests arsenate exchange with FeOH in the aqueous system.

3.2. Arsenic Adsorption versus Time. The effects of contact time (15 min to 24 h) on adsorption of As(V) by nWTR at pH values 5, 7, and 9 were evaluated, and the results are presented in Figure 3. Adsorption of As(V) by the nWTR was biphasic, consisting of an immediate sorption phase followed

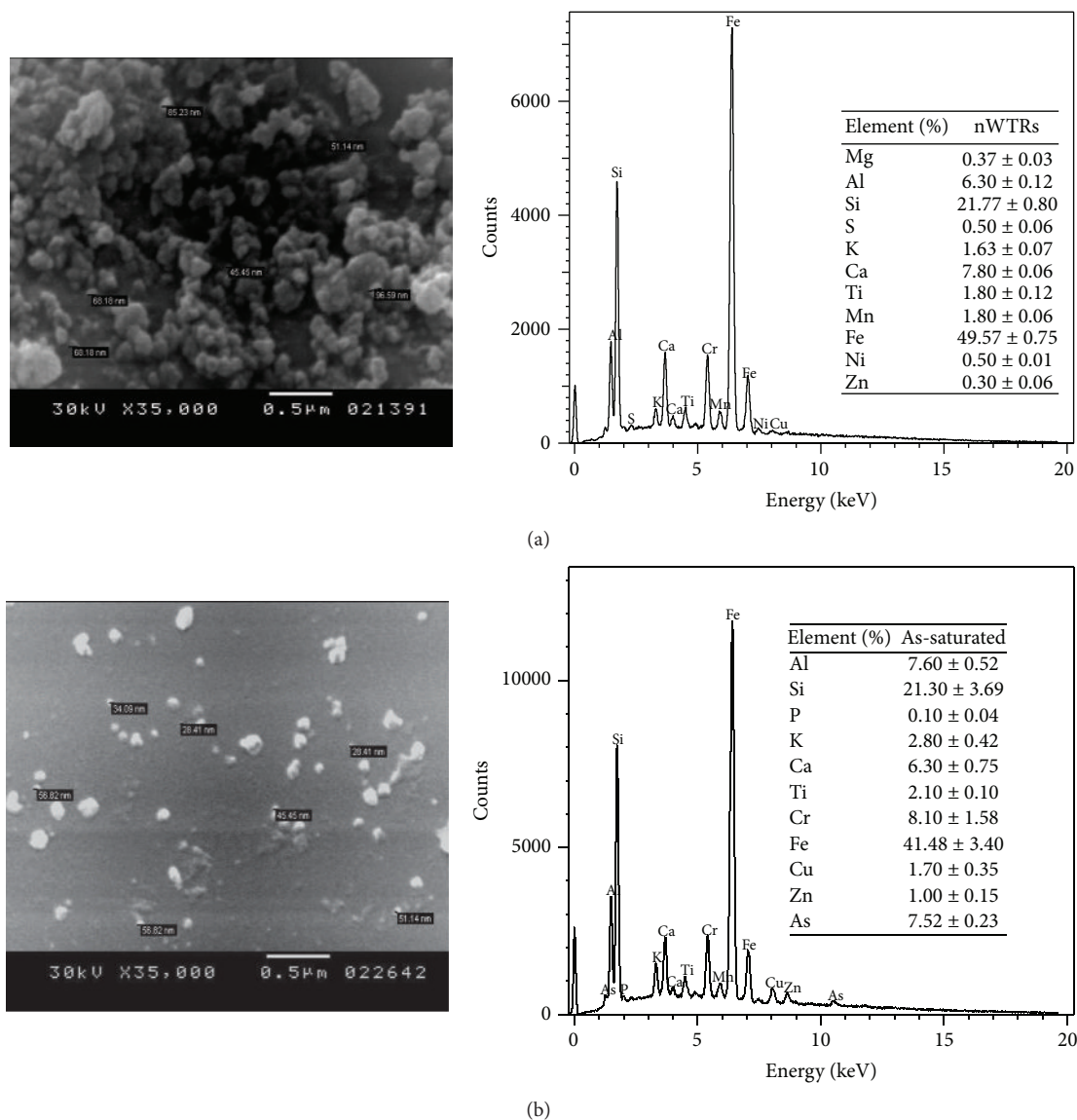


FIGURE 1: Scanning electron microscopy (SEM) image and energy dispersive X-ray (EDX) spectrum of (a) nWTR and (b) the As-saturated nWTR. The figures showed that a coating layer of adsorbed arsenic is formed on the surface of the nWTR after arsenic adsorption.

by a much slower sorption phase. The rapid adsorption of As(V) by nWTR could be due to the availability of active adsorption sites. Figure 3 also presents that As(V) adsorption on nWTR decreased as pH increased from 5 to 9. This could be attributed to the increase of negative-charge sites on the nWTR surface at high pH values. At pH > 9, HAsO_4^{2-} is the dominant As(V) species that may compete with negative site of the nWTR surface to reduce the adsorption capability due to electrostatic repulsion [16]. Approximately 89% of As was adsorbed by nWTR within the first 15 min and slowly preceded to 100% sorption by the end of the 24 h period. Therefore, using nWTR for As(V) removal is practical and highly efficient. Similar biphasic As kinetic sorption data were obtained for the Fe-WTR [17].

The kinetically driven As(V) adsorption data at three pH solution values (5, 7, and 9) were fitted to first-order, Elovich,

intraparticle diffusion, and power function models [18]. The power function model best described As(V) adsorption on nWTR as R^2 values of the model were quite high (significant at $p < 0.01$) and SE values were the lowest (Table 1 and Figure 4). The adsorption kinetics of arsenate on Fe-Si binary oxide adsorbent was also reported to follow power function model [19]. The first-order kinetics model fits the adsorption experimental data satisfactorily as evidenced by the R^2 and SE values. The much higher SE values of parabolic and Elovich models than those of power function and first-order models indicate that the predictive capability of these models to describe sorption data is not satisfactory (Table 1). Power function model parameters of As(V) sorption by nWTR as affected by solution pH are given in Table 1. The decrease in the adsorption rate (k_a) of the power function model from 6.22×10^4 to $1.99 \times 10^4 \text{ min}^{-1}$ with the increase in the system

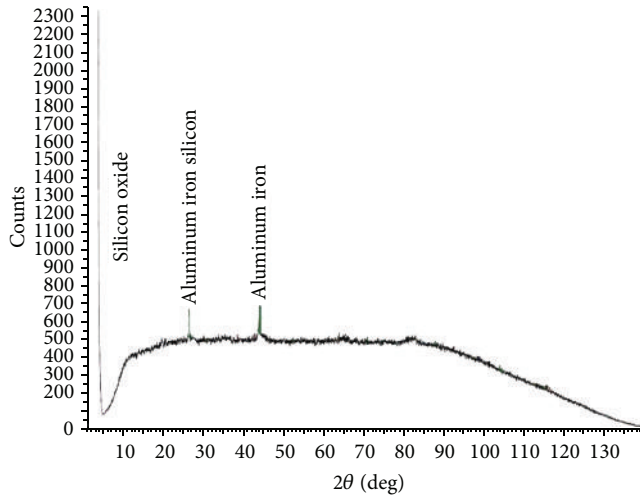


FIGURE 2: The X-ray diffraction (XRD) analyses of WTR nanoparticles. The XRD results ascertained amorphous iron, aluminum (hydr)oxides, and silicon oxide dominating all nWTR, with no apparent crystalline iron-Al (hydr)oxides.

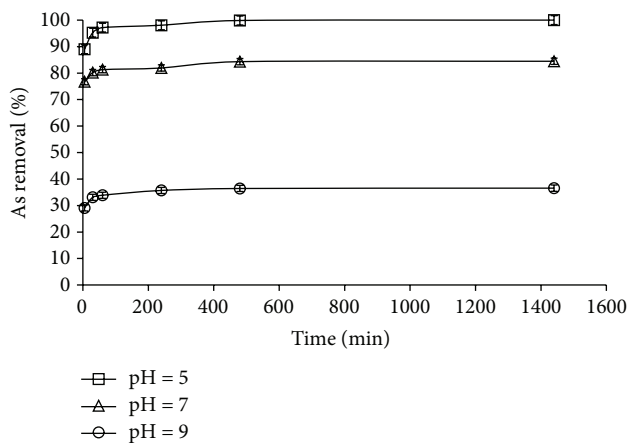


FIGURE 3: Effect of contact time on the removal of As(V) by nWTR at three different pH values. Notice that approximately 89% of As was adsorbed by nWTR within the first 15 min.

pH from 5 to 9 indicates that As(V) sorption is favored at low pH values.

3.3. Equilibrium Adsorption Studies. Equilibrium studies were performed to determine the maximum sorption capacity of WTR nanoparticles in comparison to mWTR and μ WTR. The adsorption isotherm data for the three different particle sizes of WTR was fitted to seven isotherm models (Freundlich, Langmuir, Elovich, Temkin, Kiselev, Fowler-Guggenheim, and Hill-de Boer) [15, 20, 21] for reliable prediction of adsorption parameters including maximum sorption capacity. The models tested and associated parameters are presented in Table 2. The coefficients of determination (R^2) for all of the models tested were quite high. However, the SE values of Freundlich, Fowler-Guggenheim, Hill-de Boer, Elovich, and Kiselev models were much higher than the SE

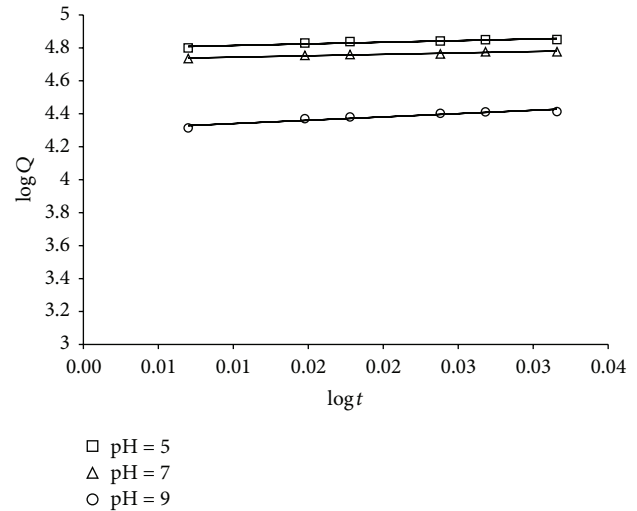


FIGURE 4: Power function kinetics model for As(V) adsorbed onto nWTR at three different pH values.

values of Langmuir and Temkin models. This indicates the low predictive capability of Freundlich, Fowler-Guggenheim, Elovich, and Kiselev models to describe sorption data (Table 2). Therefore, Freundlich, Fowler-Guggenheim, Hill-de Boer, Elovich, and Kiselev models were not analyzed further.

Langmuir Isotherm Model. R^2 and the SE values of Langmuir models for all sorbent-As systems are presented in Table 2. Arsenic sorption data conformed to the Langmuir model over the entire concentration range for all three particle sizes of WTR studied as evidenced by the high R^2 values ($p > 0.001$) and the low SE values of Langmuir model (Figure 5). The conformity of adsorption data to Langmuir model suggested the homogeneous and monolayer mode of adsorption. The Langmuir K_L , a coefficient attributed to the affinity between the sorbent and As, values for mWTR, μ WTR, and nWTR were 1.8, 144.4, and 250 (mg g^{-1}), respectively. It is clear that As sorption affinities expressed by Langmuir K_L values follow the sequence nWTR > μ WTR > mWTR. The maximum adsorption capacity (q_{max}) for mWTR, μ WTR, and nWTR was 3.33, 5.0, and 50 mg As g^{-1} , respectively (Table 2). It is interesting to note that the q_{max} of WTR nanoparticles is 16 times higher than q_{max} of Bulk WTR. This could be due to the smaller size and higher surface area ($129 \text{ m}^2 \text{ g}^{-1}$) of WTR nanoparticles compared to bulk WTR ($53.1 \text{ m}^2 \text{ g}^{-1}$). Large surface area leads to high adsorption capacity and surface reactivity [20].

Temkin Isotherm Model. The data of As(V) sorption onto the three particle sizes of WTR were analyzed according to the linear form of the Temkin isotherm and the linear plots are shown in Figure 5. R^2 and SE values of Temkin models indicate that Temkin model satisfactory fits to the As sorption data for all the three WTR particle sizes studied (Table 2). However, Langmuir model showed a better fit to adsorption data than Temkin model. The Temkin

TABLE 1: Kinetics model parameters and determination coefficients and standard error of estimate for arsenic adsorption by nWTR at 3 pH values.

Models	Parameter	pH 5	pH 7	pH 9
Elovich $q_t = (1/\beta) \ln(\alpha\beta) + (1/\beta) \ln t$	$\alpha \text{ mg g}^{-1} \text{ min}^{-1}$	2.11×10^{23}	7.32×10^{26}	1.25×10^{12}
	$\beta \text{ mg g}^{-1}$	7.49×10^{-4}	1.03×10^{-3}	1.06×10^{-3}
	R^2	0.89	0.94	0.92
	SE	1100	536	619
First-order $\ln(q_o - q) = a - k_a t$	$k_a \text{ min}^{-1}$	-0.008	-0.007	-0.008
	$a \text{ } \mu\text{g g}^{-1}$	8.59	8.50	8.24
	R^2	0.93	0.91	0.98
	SE	0.32	0.25	0.28
Parabolic diffusion $q = a + k_d t^{1/2}$	$k_d \text{ } \mu\text{g g}^{-1} \text{ min}^{-1/2}$	166.52	130.67	119.15
	$a \text{ } \mu\text{g g}^{-1}$	6580	5570	2240
	R^2	0.58	0.72	0.62
	SE	2120	1200	1380
Power function $q = k_a C_o t^{1/m}$	$k_a \text{ min}^{-1}$	6.22×10^4	5.33×10^4	1.99×10^4
	$1/m$	0.020	0.017	0.040
	R^2	0.88	0.94	0.91
	SE	0.007	0.004	0.013

q or q_t is As adsorbed (mg kg^{-1}) at time t , q_o is As adsorbed (mg kg^{-1}) at equilibrium, k_a is apparent sorption rate coefficient, α is the initial adsorption rate ($\text{mg g}^{-1} \text{ min}^{-1}$), β is a constant related to the extent of surface coverage (mg g^{-1}), a is a constant; k_d is apparent diffusion rate coefficient, q is adsorbed As (mg kg^{-1}), C_o is initial As concentration (mg L^{-1}), t is reaction time (min), k_a is sorption rate coefficient (min^{-1}), and $1/m$ is constant. R^2 is determination coefficient and SE is standard error of estimate.

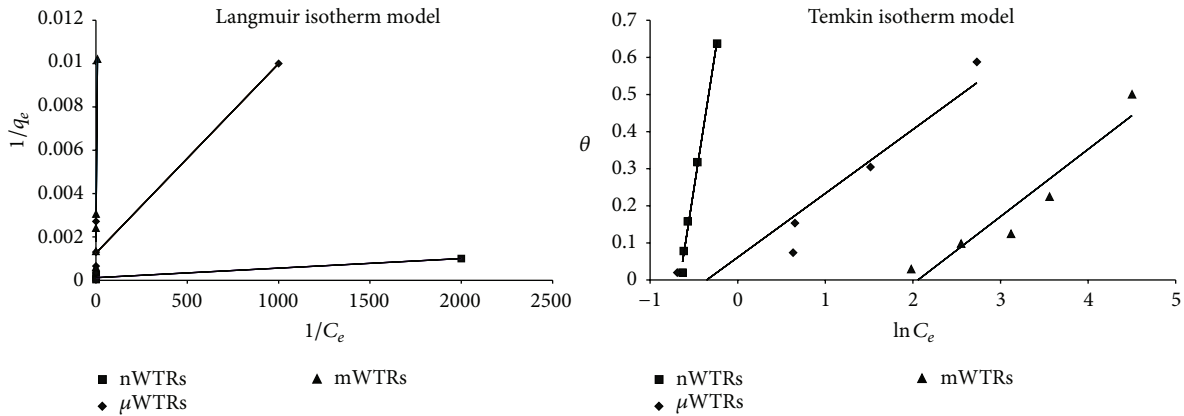


FIGURE 5: Arsenic sorption isotherm models for different particle sizes of WTR.

model assumed that the adsorption enthalpy ΔH decreases linearly with increasing surface coverage and adsorbent-adsorbate interactions [21]. The results (Table 1) showed that the adsorption reactions of As(V) on mWTR, μ WTR, and nWTR are exothermic as ΔH values are negative for all WTRs studied.

3.4. Selection of the Operating Conditions for the Adsorption Study

3.4.1. Adsorbent Dose. The effect of adsorbent dose on As(V) adsorption by nWTR is shown in Figure 6. The isotherms indicate greater differences in As sorption capacities among different doses. Adsorption of As increases rapidly with

increasing adsorbent dose of nWTR from 0.020 to 0.10 g/L. The isotherm of 0.10 g/L dose showed nearly a vertical line and has been classified as H-type isotherms suggesting a very strong metal-nWTR surface interaction [22]. The increase in As removal efficiency with increasing adsorbent dose could be attributed to more surface area available with increasing adsorbent dose. The adsorbent dose of 0.10 g/L was used in the subsequent studies.

3.4.2. Effect of Solution pH. The effect of pH on As(V) adsorption by nanoscale WTR in the pH range of 3–11 is shown in Figure 7. It can be seen that As(V) adsorption by nWTR was highly pH-dependent. The maximum efficiency of As(V) removal by nWTR was at pH 3 (88%) and the least

TABLE 2: Equilibrium model constants and standard error of estimate and determination coefficients for arsenic adsorption by the three different particles sizes of WTR.

Models	Parameter	mWTR	μ WTR	nWTR
Freundlich $q_e = K_F C_e^{1/n}$	K_F (mL g^{-1})	194.377	251.137	132.32×10^3
	$1/n$	0.3759	1.0005	6.143
	R^2	0.91	0.93	0.98
	SE	0.36	0.40	0.23
Langmuir $q_e = q_{\max}(K_L C_e / 1 + K_L C_e)$	q_{\max} ($\mu\text{g g}^{-1}$)	3333	5000	50000
	K_L (L mg^{-1})	1.8	144.44	250
	R^2	0.95	0.95	0.95
	SE	0.001	0.001	0.0001
Elovich $q_e/q_m = K_E C_e \exp(-q_e/q_m)$	q_{\max} ($\mu\text{g g}^{-1}$)	2000	3333	20000
	K_E (L mg^{-1})	0.044	0.146	0.432
	R^2	0.93	0.97	0.98
	SE	0.10	0.08	0.06
Temkin $\theta = RT/\Delta Q \ln K_0 C_e$	ΔQ (kJ mol^{-1})	13.584	14.372	1.639
	K_0 (L g^{-1})	7.930	1.426	1.94
	R^2	0.91	0.91	0.99
	SE	0.06	0.06	0.02
Fowler-Guggenheim (FG) $K_{FG} C_e = \theta / (1 - \theta \exp(2\theta w / RT))$	W (kJ mol^{-1})	12.816	5.2309	3.9852
	K_{FG} (L mg^{-1})	1.6093	1.0899	1.0849
	R^2	0.97	0.96	0.97
	SE	0.39	0.22	0.17
Kiselev $k_1 C_e = \theta / (1 - \theta)(1 + k_n \theta)$	k_1 (L mg^{-1})	0.288	22.118	44.17
	k_n	5.537	5.776	5.48
	R^2	0.95	0.95	0.95
	SE	0.996	119.55	225.03
Hill-de Boer $K_1 C_e = \theta / (1 - \theta) \exp(\theta / (1 - \theta) - K_2 \theta / RT)$	K_1 (L mg^{-1})	4.371	1.785	1.303
	K_2 (kJ mol^{-1})	54.22	14.841	4.037
	R^2	0.87	0.94	0.98
	SE	1.74	0.38	0.07

q_e (mg g^{-1}) is P adsorbed per gram of adsorbent, C_e (mg L^{-1}) is equilibrium P concentration in solution, K_F is a constant related to adsorption capacity of the adsorbent (L mg^{-1}), n is a constant, q_{\max} (mg g^{-1}) is the maximum adsorption capacity of the adsorbent, K_L (L mg^{-1}) is Langmuir constant related to the free energy of adsorption, θ is fractional coverage, R is the universal gas constant ($\text{kJ mol}^{-1} \text{K}^{-1}$), T is the temperature (K), ΔQ is ($-\Delta H$) the variation of adsorption energy (kJ mol^{-1}), K_0 is Temkin constant (L mg^{-1}), K_{FG} is Fowler-Guggenheim constant (L mg^{-1}), w is the interaction energy between adsorbed molecules (kJ mol^{-1}), k_1 is Kiselev constant (L mg^{-1}), k_n is a constant of complex formation between adsorbed molecules, K_1 is Hill-de Boer constant (L mg^{-1}), and K_2 (kJ mol^{-1}) is a constant related to the interaction between adsorbed molecules. A positive K_2 means attraction between adsorbed species and a negative value means repulsion.

efficiency of As removal by nWTR was at pH 11 (14.9%). These results show clearly that As can be readily adsorbed by nWTR in an acidic pH range. Because As(V) species (H_2AsO_4^- , HAsO_4^{2-} , and AsO_4^{3-}) exist as negative anions at the investigated pH values (3–11) [23, 24], the low efficiency of As(V) removal at high pH values could be due to the increase in the coulomb repulsive force between the surface of nWTR nanoparticles and As(V) when the solution pH increases from 3 to 11 [25].

3.4.3. Initial As Concentration and Competing Ions. The effect of initial As(V) concentration on the extent of adsorption by nWTR was investigated at As initial concentrations ranges 5–160 mg/L and the results are shown in Figure 8. When

initial As(V) concentrations were changed from 5 to 160 mg/L at room temperature, the amount sorbed per unit mass showed an increase with rise in initial As(V) concentrations. This is due to the increase in the mass driving force which allows more As(V) molecules to pass from the solution to the adsorbent surface. At low As(V) initial concentration, the ratio of As(V) in solution to the available sorption sites is small and consequently the sorption is dependent of the initial concentration, but as the concentration of the As(V) increases, the competition for sorption sites becomes fierce [26].

The removal of (As) by nWTR was markedly affected by the presence of Hg and Cr (Figure 8). The efficiency of As removal considerably decreased from 99% to 16.7–18.3% due

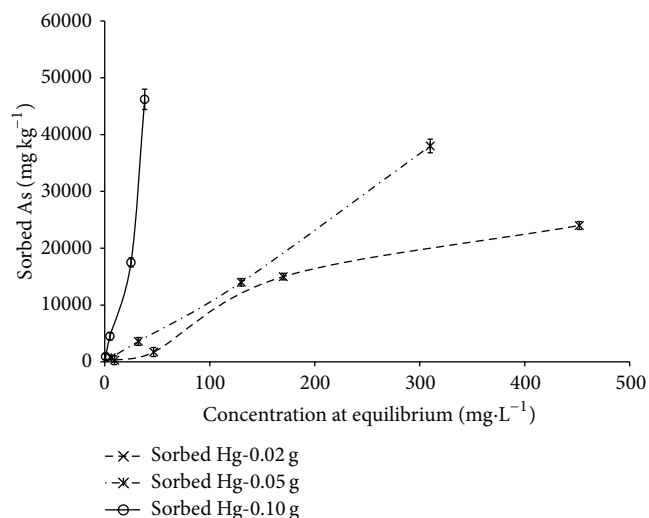


FIGURE 6: Effect of adsorbent dose on As sorbed by nWTR. Adsorption of As increases rapidly with increasing adsorbent dose of nWTR from 0.020 to 0.10 g.

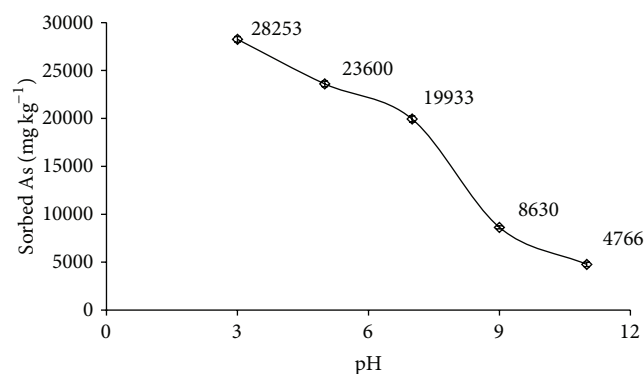


FIGURE 7: Effect of pH on As(V) adsorption by nWTR. The figure clearly shows that As(V) adsorption by nWTR was highly pH-dependent.

to the competitive effect of Hg and Cr for the adsorption sites available to As. Similar adverse effect on the adsorption of As by mixed magnetite-maghemite nanoparticles through competitive adsorption mechanism was reported [27].

3.5. Fractionation of the As-Saturated nWTR and As Mobility. The SEM-EDX and XRD analyses confirmed that the three sorbents studied (nWTR, μ WTR, and mWTR) contained two elements (Fe and Al) that have a strong affinity for As (Figures 1 and 2). Therefore, to evaluate the potential mobility of As sorbed onto nWTR relative to mWTR and μ WTR, the fractionation scheme of Tessier et al. [28] was performed on the As-saturated sorbents. According to the scheme, the labile metals are extracted as five fractions: exchangeable, carbonates, oxides, organic matter, and residual fraction. The metals associated with the residual (RS) fraction are less mobile than metals associated with the nonresidual (NORS)

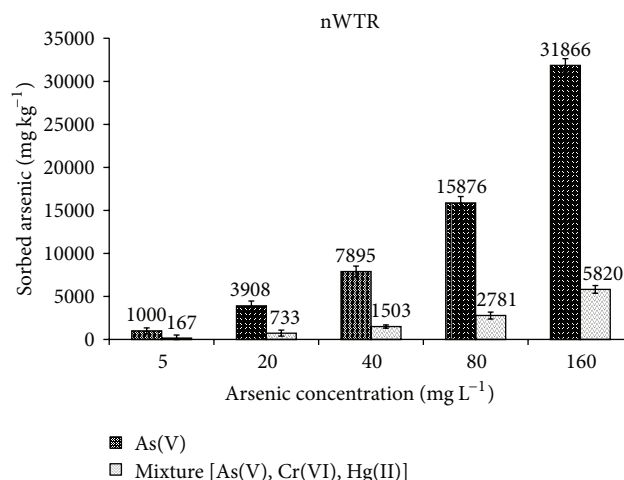
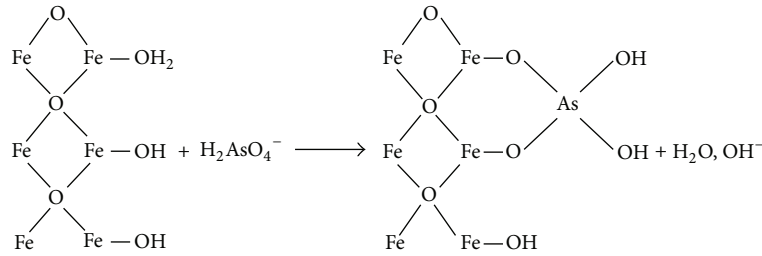


FIGURE 8: Arsenic(V) adsorption in the presence of two competing ions. Notice that the removal of (As) by nWTR was markedly affected by the presence of Hg(II) and Cr(VI).

fraction (sum of all fractions except the residual fraction). The As fractionation results (Figure 9) show that As adsorbed on mWTR was mostly associated with the more mobile nonresidual fraction (67%) whereas 80% of As on nWTR was associated with the residual fraction (RS), the less mobile fraction. The association of much greater percentage of As in the residual fraction of nWTR indicates the higher capability of nWTR to immobilize As than bulk WTR (mWTR). These observations support the hypothesis that the smaller size and the higher surface area of WTR nanoparticles greatly enhance its sorptive characteristics and stability.

3.6. Fourier Transmission Infrared Spectroscopy (FTIR). The FTIR spectroscopic analysis was performed with FTIR spectrophotometer Model 4400 (Shimadzu Corporation, Japan) to investigate the adsorption mechanism of As(V) onto nWTR. Solid adsorbent was mixed with KBr in 1:10 ratio and pressed under 10 ton pressure into pellet and the infrared spectra were measured. The FTIR spectra of nWTR before and after As adsorption are demonstrated in Figure 10. The FTIR spectrum of WTR nanoparticles before As adsorption shows (1) HOH stretching (3427 cm^{-1}) and bending (1631 cm^{-1}) vibrations of H_2O and (2) bending vibrations of hydroxyl groups on metal oxides (Al OH) at 1046 cm^{-1} [29]. After As adsorption, the band at 3416 cm^{-1} (O-H bending vibration) and the four small peaks located between 3416 and 4012 cm^{-1} (attributed to the dangling O-H bonds on the surface of the H_2O layer in nWTR) completely disappeared (Figure 10(a)). The decay of aforementioned peaks ascertained that the surface hydroxyl group on the surface of nWTR took part in the reaction with As.

Shifts in the peaks at 1626 and 1448 cm^{-1} on the surface of nWTR to higher wave numbers 1637 and 1462 cm^{-1} were noticed after As adsorption suggesting molecular interactions between As(V) and nWTR [30, 31]. However, due to the fact that stronger bonds usually vibrate faster than weaker bonds [32, 33], peaks at 1091 and 545 cm^{-1} (O-Al-O stretching



SCHEME 1

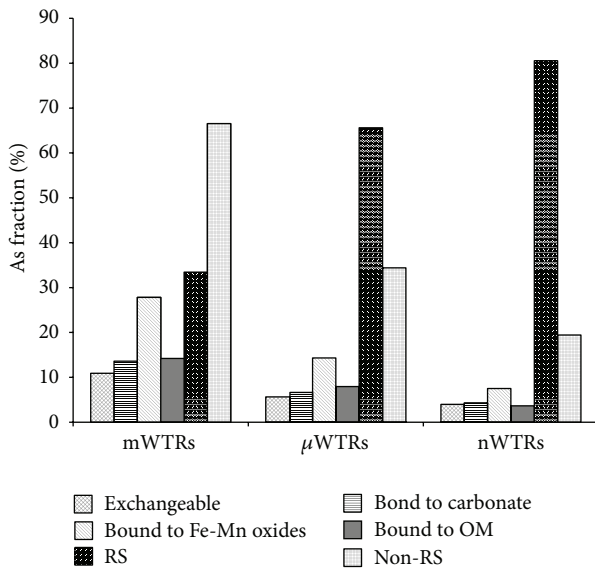


FIGURE 9: Fractionation of adsorbed As(V) on different particle sizes of WTR. Notice that As adsorbed on nWTR was mostly associated with the less mobile fraction (residual fraction, RS) which indicate the high capability of nWTR to immobilize As.

vibrations) on the surface of nWTR were shifted to lower wave numbers 1033 and 534 cm^{-1} , respectively, after arsenate adsorption.

Based on the aforementioned discussion on As(V) adsorption by WTR nanoparticles, the following mechanisms of As(V) adsorption are proposed.

(1) *On Iron Sites.* Arsenate anion is strongly bound to two adjacent structural Fe^{3+} cations through surface hydroxyl groups and form a bidentate surface complex. The surface complexation modeling study of Fukushi and Sverjensky [34] predicted that the dominant arsenate species on the surface of hematite will be a fully deprotonated bridging bidentate complex at lower pH values and higher surface coverage than the mononuclear species as shown in Scheme 1.

(2) *On Aluminum Sites.* Adsorption of arsenate ions onto aluminum hydroxides sites can be explained by the formation of inner-sphere complexes between arsenate and the singly coordinated hydroxyl groups as represented by the following equations:

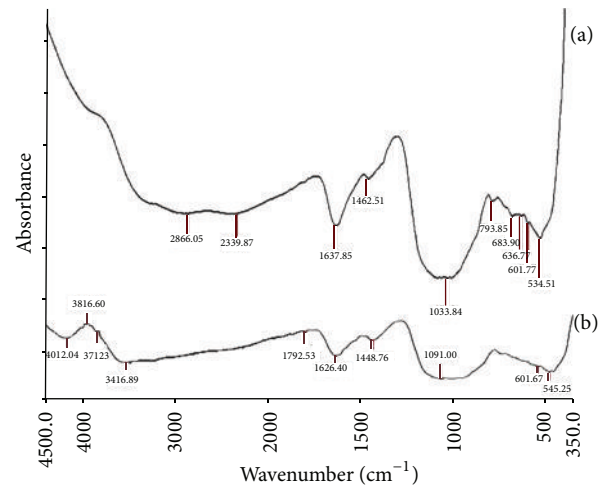
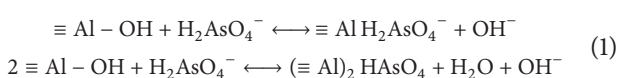


FIGURE 10: Fourier transmission infrared (FTIR) spectrum of nWTR (a) after As(V) adsorption and (b) before As(V) adsorption.

Because arsenate is not strongly bound to $\text{Al}(\text{OH})_3$ as to Fe oxides, it is suggested that formation of monodentate complex or outer-sphere complex could be possible bonding mechanisms on Al sites. The recent X-ray scattering evidence supports the presence of inner-sphere and outer-sphere As(V) on similar aluminol sites in corundum [35].

3.7. Desorption Behavior. To determine the stability of As removed by nWTR, desorption behaviors of As-loaded nWTR at various As concentrations were studied. Portions of high purity water (10.0 mL) were added to 0.1 g of arsenic-loaded nWTR and shaken. After 24 h, the solution was filtered and the filtrate was acidified and analyzed for As. The percentages of As desorbed after four consecutive cycles are shown in Figure 11. The amounts of As released increased from 0.49 to 1.73% as the As concentrations increased from 5 to 500 mg/L (at pH 7.0). It is clear that the As adsorbed on nWTR was not significantly altered as less than 2% of adsorbed As was released at the highest As concentration load after 4 consecutive desorption cycles. These results suggest the stability of As-nWTR surface complexes.

4. Conclusion

A low cost adsorbent, water treatment residual nanoparticles, has proven to be effective in As(V) removal from the aqueous solution. Kinetics data reveal that 89% of As(V) was adsorbed

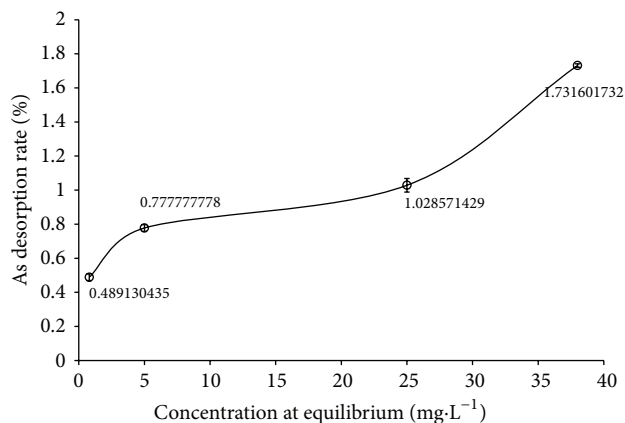


FIGURE 11: Desorption of As(V) from nWTR loaded with different As concentrations. Notice the stability of As adsorbed on nWTR as less than 2% of adsorbed As was released after 4 consecutive desorption cycles.

by nWTR within the first 15 min and slowly preceded to 100% sorption by the end of the 24 h period. The equilibrium data fitted well to the Langmuir and Temkin models and the maximum adsorption capacity (q_{\max}) of WTR nanoparticles was 16 times higher than q_{\max} of Bulk WTR. The As(V) removal by nWTR was strongly dependent on pH and the formation of bidentate and monodentate surface complexes could be possible bonding mechanisms for As(V) sorption on Fe and Al sites, respectively. The high capability of nWTR to remove As(V) from aqueous media and the stability of As-nWTR surface complexes suggest the great potential of nWTR as economic and effective sorbent for removal of As from contaminated natural water and wastewater.

Conflict of Interests

The authors declare that there is no conflict of interests regarding the publication of this paper.

Acknowledgment

The authors gratefully acknowledge the financial support from the Egyptian Science and Technology Development Fund (STDF 4977-2013).

References

- [1] D. Mohan and C. U. Pittman Jr., "Arsenic removal from water/wastewater using adsorbents—a critical review," *Journal of Hazardous Materials*, vol. 142, no. 1-2, pp. 1-53, 2007.
- [2] T. S. Y. Choong, T. G. Chuah, Y. Robia, F. L. G. Koay, and I. Azni, "Arsenic toxicity, health hazards and removal techniques from water: an overview," *Desalination*, vol. 217, no. 1-3, pp. 139-166, 2007.
- [3] K. Košutić, L. Furač, L. Sipos, and B. Kunst, "Removal of arsenic and pesticides from drinking water by nanofiltration membranes," *Separation and Purification Technology*, vol. 42, no. 2, pp. 137-144, 2005.
- [4] Y.-H. Xu, T. Nakajima, and A. Ohki, "Adsorption and removal of arsenic(V) from drinking water by aluminum-loaded Shirasuzzeolite," *Journal of Hazardous Materials*, vol. 92, no. 3, pp. 275-287, 2002.
- [5] Y. Zhang, M. Yang, and X. Huang, "Arsenic(V) removal with a Ce(IV)-doped iron oxide adsorbent," *Chemosphere*, vol. 51, no. 9, pp. 945-952, 2003.
- [6] US Environmental Protection Agency (USEPA), *Arsenic Treatment Technologies for Soil, Waste, and Water*, EPA-542-R-02-004, Office of Solid Waste and Emergency Response, 2002.
- [7] N. Savage and M. S. Diallo, "Nanomaterials and water purification: opportunities and challenges," *Journal of Nanoparticle Research*, vol. 7, no. 4-5, pp. 331-342, 2005.
- [8] R. P. Schwarzenbach, B. I. Escher, K. Fenner et al., "The challenge of micropollutants in aquatic systems," *Science*, vol. 313, no. 5790, pp. 1072-1077, 2006.
- [9] J. A. Ippolito, K. A. Barbarick, D. M. Heil, J. P. Chandler, and E. F. Redente, "Phosphorus retention mechanisms of a water treatment residual," *Journal of Environmental Quality*, vol. 32, no. 5, pp. 1857-1864, 2003.
- [10] D. Sarkar, K. C. Makris, V. Vandanapu, and R. Datta, "Arsenic immobilization in soils amended with drinking-water treatment residuals," *Environmental Pollution*, vol. 146, no. 2, pp. 414-419, 2007.
- [11] E. A. Elkhatib, A. M. Mahdy, and M. M. ElManeah, "Effects of drinking water treatment residuals on nickel retention in soils: a macroscopic and thermodynamic study," *Journal of Soils and Sediments*, vol. 13, no. 1, pp. 94-105, 2013.
- [12] E. A. Elkhatib and M. L. Moharem, "Immobilization of copper, lead, and nickel in two arid soils amended with biosolids: effect of drinking water treatment residuals," *Journal of Soils and Sediments*, vol. 15, no. 9, pp. 1937-1946, 2015.
- [13] E. A. Elkhatib, A. M. Mahdy, and K. A. Salama, "Green synthesis of water treatment residual nanoparticles using precision milling," *Environmental Chemistry Letters*, vol. 13, pp. 333-339, 2015.
- [14] A. G. Caporale, P. Punamiya, M. Pigna, A. Violante, and D. Sarkar, "Effect of particle size of drinking-water treatment residuals on the sorption of arsenic in the presence of competing ions," *Journal of Hazardous Materials*, vol. 260, pp. 644-651, 2013.
- [15] E. A. Elkhatib, A. M. Mahdy, F. K. Sherif, and K. A. Salama, "Water treatment residual nanoparticles: a novel sorbent for enhanced phosphorus removal from aqueous medium," *Current Nanoscience*, vol. 11, no. 5, pp. 655-668, 2015.
- [16] F.-S. Zhang and H. Itoh, "Iron oxide-loaded slag for arsenic removal from aqueous system," *Chemosphere*, vol. 60, no. 3, pp. 319-325, 2005.
- [17] K. C. Makris, D. Sarkar, and R. Datta, "Evaluating a drinking-water waste by-product as a novel sorbent for arsenic," *Chemosphere*, vol. 64, no. 5, pp. 730-741, 2006.
- [18] E. A. Elkhatib, O. L. Bennett, and R. J. Wright, "Kinetics of arsenite sorption in soils," *Soil Science Society of America Journal*, vol. 48, no. 4, pp. 758-762, 1984.
- [19] L. Zeng, "Arsenic adsorption from aqueous solutions on an Fe(III)-Si binary oxide adsorbent," *Water Quality Research Journal of Canada*, vol. 39, no. 3, pp. 267-275, 2004.
- [20] T. A. Kurniawan and W.-H. Lo, "Removal of refractory compounds from stabilized landfill leachate using an integrated H₂O₂ oxidation and granular activated carbon (GAC) adsorption treatment," *Water Research*, vol. 43, no. 16, pp. 4079-4091, 2009.

- [21] K. Y. Foo and B. H. Hameed, "Insights into the modeling of adsorption isotherm systems," *Chemical Engineering Journal*, vol. 156, no. 1, pp. 2–10, 2010.
- [22] C. H. Giles, T. H. MacEwan, N. S. Nakhwa, and D. Smith, "Studies in sorption. Part XI. A system of classification of solution adsorption isotherms, and its use in diagnosis on adsorption mechanisms and in measurement of specific surface areas of solids," *Journal of the Chemical Society*, vol. 111, pp. 3973–3993, 1960.
- [23] D. Mohan and C. U. Pittman Jr., "Arsenic removal from water/wastewater using adsorbents—a critical review," *Journal of Hazardous Materials*, vol. 142, no. 1–2, pp. 1–53, 2007.
- [24] B. A. Manning, M. L. Hunt, C. Amrhein, and J. A. Yarmoff, "Arsenic(III) and arsenic(V) reactions with zerovalent iron corrosion products," *Environmental Science and Technology*, vol. 36, no. 24, pp. 5455–5461, 2002.
- [25] C. Wang, H. Luo, Z. Zhang, Y. Wu, J. Zhang, and S. Chen, "Removal of As(III) and As(V) from aqueous solutions using nanoscale zero valent iron-reduced graphite oxide modified composites," *Journal of Hazardous Materials*, vol. 268, pp. 124–131, 2014.
- [26] R. Saravanane, T. Sundararajan, and S. S. Reddy, "Efficiency of chemically modified low cost adsorbents for the removal of heavy metals from waste water: a comparative study," *Indian Journal of Environmental Health*, vol. 44, no. 2, pp. 78–87, 2002.
- [27] S. R. Chowdhury and E. K. Yanful, "Arsenic and chromium removal by mixed magnetite-maghemite nanoparticles and the effect of phosphate on removal," *Journal of Environmental Management*, vol. 91, no. 11, pp. 2238–2247, 2010.
- [28] A. Tessier, P. G. C. Campbell, and M. Blsson, "Sequential extraction procedure for the speciation of particulate trace metals," *Analytical Chemistry*, vol. 51, no. 7, pp. 844–851, 1979.
- [29] Y. Zhang, M. Yang, X.-M. Dou, H. He, and D.-S. Wang, "Arsenate adsorption on an Fe-Ce bimetal oxide adsorbent: role of surface properties," *Environmental Science and Technology*, vol. 39, no. 18, pp. 7246–7253, 2005.
- [30] V. M. Bermudez, "Effect of humidity on the interaction of dimethyl methylphosphonate (DMMP) vapor with SiO₂ and Al₂O₃ surfaces, studied using infrared attenuated total reflection spectroscopy," *Langmuir*, vol. 26, no. 23, pp. 18144–18154, 2010.
- [31] P. Tarte, "Infra-red spectra of inorganic aluminates and characteristic vibrational frequencies of AlO₄ tetrahedra and AlO₆ octahedra," *Spectrochimica Acta Part A: Molecular Spectroscopy*, vol. 23, no. 7, pp. 2127–2143, 1967.
- [32] D. A. Skoog, F. J. Holler, and T. A. Nieman, *Principles of Instrumental Analysis*, Harcourt Brace and Company, Orlando, Calif, USA, 5th edition, 1998.
- [33] K. B. Payne and T. M. Abdel-Fattah, "Adsorption of arsenate and arsenite by iron-treated activated carbon and zeolites: effects of pH, temperature, and ionic strength," *Journal of Environmental Science and Health—Part A: Toxic/Hazardous Substances and Environmental Engineering*, vol. 40, no. 4, pp. 723–749, 2005.
- [34] K. Fukushi and D. A. Sverjensky, "A predictive model (ETLM) for arsenate adsorption and surface speciation on oxides consistent with spectroscopic and theoretical molecular evidence," *Geochimica et Cosmochimica Acta*, vol. 71, no. 15, pp. 3717–3745, 2007.
- [35] J. G. Catalano, C. Park, P. Fenter, and Z. Zhang, "Simultaneous inner- and outer-sphere arsenate adsorption on corundum and hematite," *Geochimica et Cosmochimica Acta*, vol. 72, no. 8, pp. 1986–2004, 2008.

Research Article

Kinetics, Equilibrium, and Thermodynamics of the Sorption of Bisphenol A onto N-CNTs- β -Cyclodextrin and Fe/N-CNTs- β -Cyclodextrin Nanocomposites

Keletso Mphahlele,^{1,2} Maurice S. Onyango,¹ and Sabelo D. Mhlanga³

¹Department of Chemical and Metallurgical Engineering, Tshwane University of Technology, Private Bag X680, Pretoria 0001, South Africa

²DST-CSIR Nanotechnology Innovation Centre, National Centre for Nanostructured Materials, P.O. Box 395, Pretoria 0001, South Africa

³Nanotechnology and Water Sustainability Research Unit, College of Science, Engineering and Technology, University of South Africa, Florida, Johannesburg 1709, South Africa

Correspondence should be addressed to Sabelo D. Mhlanga; mhlands@unisa.ac.za

Received 18 July 2015; Revised 21 September 2015; Accepted 29 September 2015

Academic Editor: Sesha Srinivasan

Copyright © 2015 Keletso Mphahlele et al. This is an open access article distributed under the Creative Commons Attribution License, which permits unrestricted use, distribution, and reproduction in any medium, provided the original work is properly cited.

We analysed the adsorptive behaviour of Fe/N-CNTs- β -CD nanocomposite in the removal of bisphenol A (BPA) from aqueous solution and identified the key influencing parameters. The Fe/N-CNTs- β -CD nanocomposite adsorbent was prepared by dispersing Fe uniformly on N-CNTs- β -CD using a microwave polyol method and characterized using Fourier transform infrared spectroscopy (FTIR), focused ion beam scanning electron microscopy (FIB-SEM), and energy-dispersive X-ray spectroscopy (EDS). The solution pH and temperature had minimal effect on sorption of BPA while the initial concentration and adsorbent mass affected the adsorption of BPA. No leaching of Fe into the water was observed; thus the nanocomposites were found suitable for use in water purification. From equilibrium isotherm studies, the Langmuir isotherm model gave the best description of the experimental data. The Langmuir monolayer adsorption capacities of BPA onto N-CNTs- β -CD and Fe/N-CNTs- β -CD are 38.20 mg·g⁻¹ and 80.65 mg·g⁻¹ at 298 K, respectively. Evidently, these adsorption capacity values gave an indication that uniform dispersion of Fe N-CNTs- β -CD prepared by the microwave polyol method enhances the adsorption of BPA. Meanwhile, the sorption kinetics of BPA onto Fe/N-CNTs- β -CD were best described by the pseudo-second-order model.

1. Introduction

Bisphenol A (BPA) is generally used as a monomer in the fabrication of polycarbonates and epoxy resins, as an antioxidant in polyvinyl chloride (PVC) plastics, and as an inhibitor of end polymerization in PVC polymers [1]. As a consequence, BPA is present in products such as the interior coating of wine storage vats, food cans, milk containers, water carboys, food storage vessels, dental materials, baby formula bottles, and water pipes [2]. Due to the recurrent usage of polycarbonate plastics, epoxy resins, and PVC in industry and at homes, BPA has been allegedly observed in rivers, seas, and soils. It is known to have estrogenic activity and it can interfere with endocrine systems of animals and people [3].

Furthermore, BPA is difficult to remove once it builds up in the environment or in the human body due to its poor solubility (381 mg·L⁻¹ in water) [4]. The main sources of BPA discharged to environmental water are expected to be the release of industrial wastewater and municipal effluent [5]. Therefore, the removal of BPA from environmental water is necessary and critical.

Some existing technologies to remove BPA from the aquatic environment include adsorption [5–9], solvent extraction [10], membrane separation technology [11], and photodegradation [9, 12]. Removal of BPA by adsorption is economically feasible especially if the adsorbent has high adsorption efficiency and can be recycled. Some adsorbents that have been explored in the removal of BPA from aqueous

solution include activated carbon, mineral clays, raw agricultural solid wastes, and waste materials from forest industries such as maize cob, palm-fruit bunch particles, bagasse pith, sawdust, papaya seeds, and hazelnut shell [13–16]. Most of these materials have low sorption capacity and therefore are not suitable for adsorption technology.

Much attention has shifted towards the use of biopolymers and natural molecules as adsorbents [17]. Cyclodextrins (CDs) are known to form host-guest complexes with hydrophobic compounds. This phenomenon leads to the idea that insolubilized CDs may act as a good adsorbent of BPA [18]. However, because of their solubility in water, CDs cannot be used directly for separation, and hence it seemed plausible that insoluble CDs copolymerized with carbon nanotubes (CNTs) would be good candidates for a recyclable adsorbent [19], which can selectively bind to BPA in water. When CNTs (1–5%) were copolymerized with CDs polymer the recyclability improved considerably, losing only 10% of the polymer mass over twenty-five cycles, compared to 50% loss over nine cycles for the natural CD polymers [20]. In order to further tune CNTs, nitrogen doping is necessary. Modification of the crystalline nanotube properties by controllably placing defects or foreign atoms (heteroatoms) brings along tremendous technological implications [21]. CNTs with nitrogen wall doping possess outer walls with defects and rugosity that provide unique sites for chemical functionalization of the CNTs. This is a way to improve the tube covalent chemistry, which once functionalized can serve to anchor groups or particles that are useful for further functionalization routes [21].

Zero-valent iron (Fe) nanoparticles (NPs) are known for their reductive properties and their sorption capabilities for organics and heavy metals by turning them into less toxic forms or less soluble forms through changes in their oxidation state and/or by adsorption [22]. Concerns over the discharge of these NPs into the environment led to this study where the NPs were anchored on nitrogen doped carbon nanotubes (N-CNTs) in order to immobilize and reduce their environmental mobility. It was believed that a combination of Fe-NPs, N-CNTs, and CD polymers would form an effective adsorbent with enhanced performance for water treatment.

Consequently, the objective of this study was to investigate the sorption equilibrium, kinetics, and thermodynamics of BPA removal from aqueous solution using metal dispersed N-doped carbon nanotubes- β -cyclodextrin (Fe/N-CNTs- β -CD) nanocomposites. The metal nanoparticles were dispersed on N-CNTs by a microwave polyol method. The stability of the metal (Fe) on Fe/N-CNTs- β -CD was explored by determining the amount of Fe released under predetermined sonication times. The effects of time, initial concentration, pH, and temperature on BPA removal from aqueous solution were investigated. Appropriate mathematical models were used to interpret experimental data.

2. Materials and Methods

2.1. Materials. All solvents and chemicals used in this study were purchased from Sigma-Aldrich (USA) and were used as received without further purification. The endocrine

disrupting compound (EDC) used as target adsorbate in the present study was bisphenol A (BPA, 97% purity, CAS 80-05-7 and molecular weight of 228.29 g·mol⁻¹). Reagent grade chemicals such as sodium hydroxide (NaOH) and nitric acid (HNO₃, 65%) were used for adjusting initial pH. N,N-Dimethylformamide (DMF, 99% purity) and toluene diisocyanate (TDI, 98% purity) were used to copolymerize β -CDs and N-CNTs.

2.2. Preparation of N-CNTs and Fe/N-CNTs Copolymerized with β -CD. In a typical reaction, 2 g of β -CDs was dried and dissolved in 18 mL of DMF with constant stirring. To this, a solution of presuspended and sonicated (10 min) 1% of N-CNTs and Fe/N-CNTs in 2 mL DMF was added. The mixture of β -CD and Fe/N-CNTs was then heated to 70°C followed by dropwise addition of 2 mL of the bifunctional linker, TDI. This mixture was stirred under inert atmosphere for 24 h. The formed polymer was precipitated, washed with acetone, and dried under vacuum overnight at ambient temperature.

2.3. Batch Adsorption Equilibrium Studies. Batch equilibrium adsorption experiments were carried out using a bottle-point method. In this method a stock solution of BPA (1000 mg·L⁻¹) was prepared and was subsequently diluted to the required initial concentrations. The adsorption capacity of the sorbent towards BPA was determined by contacting a constant mass (0.05 g) of sorbent with a fixed volume (50 mL) in sealed plastic bottles. Two variables were explored: changes in initial pH (pH 2–10) at a fixed concentration of BPA of 100 mg·L⁻¹ and changes in temperature (temperatures 298–318 K) at initial concentrations ranging within 10–100 mg·L⁻¹ of BPA solution. The bottles were agitated in an isothermal water bath shaker for 24 h until equilibrium was reached.

A calibration curve for BPA was prepared by recording the absorbance values for a range of known concentrations of BPA solution at the maximum absorbance of $\lambda_{\max} = 276$ nm using double beam Ultraviolet-Visible (UV-Vis) spectrophotometer (Lambda 7505, Perkin Elmer). The amount of BPA adsorbed onto sorbent, q_e (mg·g⁻¹), was calculated by the following equation:

$$q_e = \frac{(C_o - C_e)V}{m}, \quad (1)$$

where C_o and C_e are the initial and equilibrium concentrations of BPA solution (mg·L⁻¹), respectively, V is the total volume of the BPA solution (L), and m is the mass of sorbent used (g).

Further, two equilibrium isotherm models, the Langmuir and Freundlich models, were used to describe the relationship between the adsorbed amount of BPA and its equilibrium concentration in solution. The Langmuir isotherm is represented:

$$q_e = \frac{Q_{\max} b_L C_e}{1 + b_L C_e}. \quad (2)$$

The linearized Langmuir isotherm is expressed by

$$\frac{C_e}{q_e} = \frac{1}{b_L Q_{\max}} + \frac{C_e}{Q_{\max}}, \quad (3)$$

where b_L is the Langmuir affinity constant ($L \cdot mg^{-1}$) and Q_{max} is the maximum adsorption capacity of the material ($mg \cdot g^{-1}$).

The Freundlich isotherm is represented by the following [23]:

$$q_e = K_F C_e^{1/n}. \quad (4)$$

The linearized Freundlich isotherm is expressed as follows:

$$\ln q_e = \ln K_F + \frac{1}{n} \ln C_e, \quad (5)$$

where K_F is the Freundlich constant ($L \cdot g^{-1}$) and n is the heterogeneity factor. The K_F value is related to the adsorption capacity, while $1/n$ value is related to the adsorption intensity. The magnitude of exponent (n) gives an indication of the favourability of the sorbent/sorbate system [24].

2.4. Batch Adsorption Kinetics. The kinetics of BPA removal from aqueous solution were studied by varying mass of the sorption media and initial concentration of BPA. The experiments were carried out separately in 1 L batch reactor. When exploring the effect of mass (0.5 g, 0.7 g, and 1 g) of sorption media, the initial BPA concentration of $50 \text{ mg} \cdot \text{L}^{-1}$ was used. In the case when initial (50, 75, and $100 \text{ mg} \cdot \text{L}^{-1}$) concentration was a variable, the sorbent mass was fixed at $1 \text{ g} \cdot \text{L}^{-1}$. The reactor was stirred with an overhead stirrer operated at 200 rpm. At predetermined time intervals, 5 mL samples were taken from the reactor and filtered through a syringe filter and residual BPA concentration was analysed by UV-Vis spectroscopy. By performing appropriate material balance, the quantity of BPA adsorbed at the selected time intervals was determined and used for kinetic analysis. The amount of BPA adsorbed at any time was calculated by

$$q_t = \frac{(C_o - C_t) V}{m}, \quad (6)$$

where C_t is the concentration of BPA solution at any time ($mg \cdot L^{-1}$). The kinetic data was modelled using the pseudo-first-order, pseudo-second-order, and Elovich kinetic models. The Lagergren pseudo-first-order kinetic rate expression is given by [24, 25]:

$$\frac{dq_t}{dt} = k_1 (q_e - q_t). \quad (7)$$

Integrating this for the boundary conditions $t = 0$ to $t = t$ and $q_t = 0$ to $q_t = q_t$, (7) may be rearranged for linearized data plotting as shown in

$$\log (q_e - q_t) = \log q_e - \frac{k_1}{2.303} t, \quad (8)$$

where k_1 is the rate constant of first-order sorption (min^{-1}). The pseudo-second-order kinetic rate equation is expressed as [15]:

$$\frac{dq_t}{dt} = k_2 (q_e - q_t)^2. \quad (9)$$

Integrating this for the boundary conditions $t = 0$ to $t = t$ and $q_t = 0$ to $q_t = q_t$, (9) may be rearranged for linearized data plotting as

$$\frac{t}{q_t} = \frac{1}{k_2 q_e^2} + \frac{t}{q_e}, \quad (10)$$

where k_2 is the rate constant of second-order sorption ($g \cdot mg^{-1} \cdot \text{min}^{-1}$). Finally, the Elovich model equation is generally expressed as [26]:

$$\frac{dq_t}{dt} = \alpha \exp(-\beta q_t), \quad (11)$$

where α is the initial adsorption rate ($mg \cdot g^{-1} \cdot \text{min}^{-1}$) and β is the desorption constant ($g \cdot mg^{-1}$). To simplify the Elovich equation, it can be assumed that $\alpha\beta t \gg t$ and by applying the boundary condition $q_t = 0$ at $t = 0$ and $q_t = q_t$ at $t = t$, (11) becomes

$$q_t = \frac{\ln(\alpha\beta)}{\beta} + \frac{1}{\beta} \ln t. \quad (12)$$

2.5. Error Analysis. Due to the inherent bias resulting from linearization [27], attempts were made to compare the kinetic and equilibrium models by the square sum of errors (SSE). SSE is represented by

$$SSE = \sum_{i=1}^n \frac{\sqrt{(q_{e,\text{exp}} - q_{e,\text{cal}})^2}}{N}. \quad (13)$$

3. Results and Discussion

3.1. Characterization of the Nanocomposite Materials before and after Sorption. For most real-world applications, experimental conditions need to be tightly controlled in order to obtain nanoparticles (NPs) with at least the following characteristics: identical particles in terms of size (a uniform size distribution), shape, or morphology, chemical composition and crystal structure (ideally, core and surface composition must be the same, unless specifically designed for other purposes), and monodispersity (no aggregation) [28, 29]. A facile, fast, and green microwave polyol approach was adopted to disperse Fe nanoparticles into the internal matrix of N-CNTs. The sorbent was characterized before and after BPA sorption and the results are as discussed in Sections 3.1.1 and 3.1.2.

3.1.1. Focused Ion Beam Scanning Electron Microscopy (FIB-SEM). The surface morphology of the Fe/N-CNTs- β -CD sorbent before and after sorption of BPA is shown in Figure 1. The FIB-SEM was used to assess the morphological changes in the sorbent surface following sorption of BPA. The sorbent before sorption exhibited a cave-like, irregular, and uneven surface morphology. The roughness of the surface is considered as a factor providing an increase in the surface area. In addition, the material was porous and this property reduces the diffusional resistance and makes it easy for mass transfer

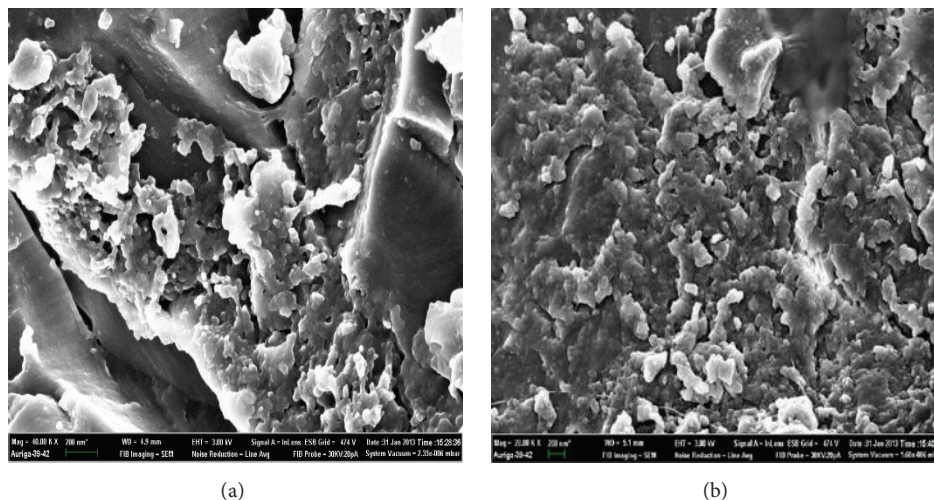


FIGURE 1: SEM images of Fe/N-CNTs- β -CD nanocomposite polymer before (a) and after (b) adsorption of BPA. The Fe/CNTs could not be seen because they were embedded in the bulk of the β -CD polymer.

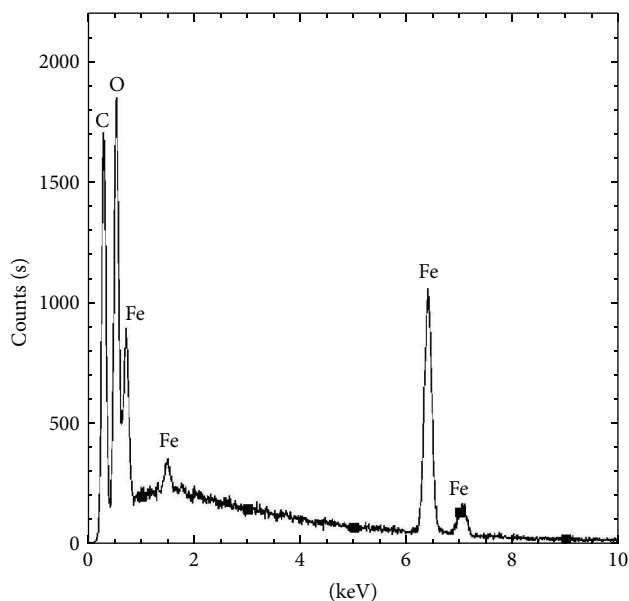


FIGURE 2: Energy-dispersive X-ray spectroscopy of Fe/N-CNTs.

to take place because of high internal surface area [30, 31]. It is clearly seen that, after sorption process (Figure 1(b)), the pores and surface of the sorbent were covered; the sorbate may have densely and homogeneously adhered to the surface of the sorbent as a result of either natural entrapment into the porous nanocomposite due to physical sorption by electrostatic forces or covalent binding between the cellular sorbent and the sorbate [32, 33].

Figure 2 shows the EDS analysis of the Fe/N-CNTs nanocomposites taken from various points with high magnification in order to do an elemental qualitative composition of the metal particles. The nanocomposites contained the Fe as desired. The EDS analysis gave quantitative results of Fe

TABLE 1: Quantitative results for Fe/N-CNTs using EDS.

Element line	Weight percentage	Weight % error	Atom %	Atom % error
C K	19.43	± 0.17	31.5	± 0.24
O K	60.55	—	65.1	± 23.25
Fe K	20.01	± 6.34	3.4	± 0.11
Total	100		100	

at concentrations above 20 wt.%. Accuracies for the major elements in aqueous standards were 6.34% (Table 1).

3.1.2. FTIR Spectroscopy Analysis. Sorbents are widely used as separation media in water treatment to remove organic and inorganic contaminants from polluted water. Nanomaterials have two main properties that make them particularly attractive as sorbents. On a mass basis, they have greatly larger surface areas than their bulk counterparts. Nanomaterials can also be functionalized with various chemical groups to increase their affinity towards the targeted contaminants [34]. Concerns over the discharge of these nanomaterials into the environment prompted us to use N-CNTs as a support for Fe nanoparticles in order to immobilize and reduce their environmental mobility [20]. CDs are slightly soluble in water and this restricts their application in water purification. This necessitates their functionalization and, in particular, polymerization of the parental CDs with suitable bifunctional linkers such as hexamethylene diisocyanate (HDI) and toluene diisocyanate (TDI) [35]. Evidence of polymerization was confirmed by the disappearance of the isocyanate peak (Figure 3(a)) in the FTIR spectrum. Complete disappearance of the isocyanate peak was observed after 16 h of polymerization (Figure 3(b)). This was an indication that polymerization was complete. The FTIR bands corresponding to C-H (2938 cm^{-1}), C=O (1714 cm^{-1}), and C=C (1631 cm^{-1}) further confirmed that polymerization between monomers (N-CNTs

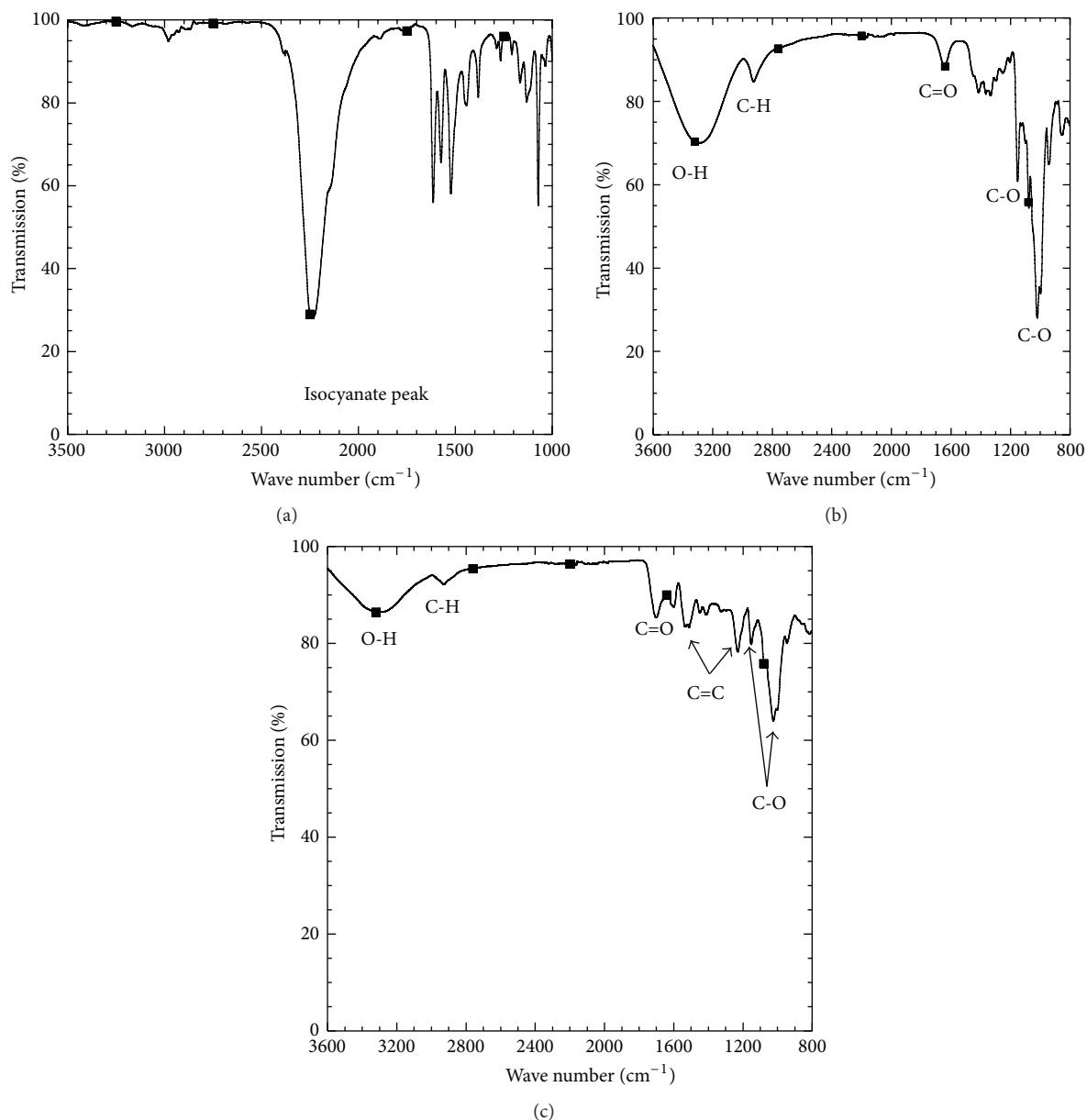


FIGURE 3: FTIR spectra of the copolymerization of β -CD and metal/N-CNTs: (a) at start of the reaction, (b) after 16 h, and (c) after adsorption.

and β -CD) and the linker (TDI) had occurred [36, 37]. Comparing Figures 3(b) and 3(c) after adsorption, a shift or disappearance of peaks C-O (1200 cm^{-1} and 1000 cm^{-1}) and C-H (2938 cm^{-1}) was observed. The appearance of new peaks was also observed, that is, C=C at 1600 cm^{-1} and 1500 cm^{-1} . These changes observed in the spectrum indicate the possible involvement of those functional groups on the surface of the sorbent during sorption process.

3.2. Effect of pH on BPA Sorption. The pH of water varies for different sources. From a chemistry point of view, this affects the charge of a given sorbate and the surface charge density of the sorbent. Thus depending on the pH value of solution and nature of the sorption process, a coulombic repulsive or attractive force may be experienced in a sorptive

system [9, 38]. The effect of solution pH on BPA sorption onto CNTs- β -CD and Fe/N-CNTs- β -CD was studied by varying the initial pH from 2 to 12. The results are presented in Figure 4. The removal of BPA from aqueous solution was found to be insensitive to pH changes. It is well known that CDs form host-guest complexes with hydrophobic compounds [18]. These results suggested that BPA was trapped by the sorbents through the hydrophobic interaction and the hydrogen-bonding interaction simultaneously [39]. A pH 7 was selected for the following studies to minimise cost of pH adjustment that may be required in real field situation. Meanwhile, it was also observed that the sorption capacity for sorbent Fe/N-CNTs- β -CD was higher than that of N-CNTs- β -CD, that is, $79.85\text{ mg}\cdot\text{g}^{-1}$ and $38.9\text{ mg}\cdot\text{g}^{-1}$, respectively. Having Fe nanoparticles on the surface of the N-CNTs

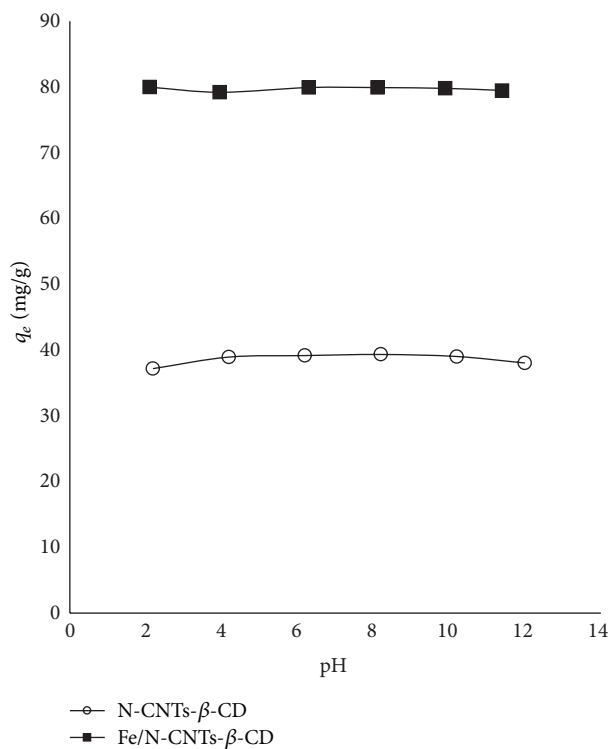


FIGURE 4: The effect of pH on the removal of BPA.

enhanced the sorption capacity of the sorbent. Consequently the subsequent discussions are centred on Fe dispersed N-CNTs-β-CD.

3.3. Effect of Temperature: Sorption Equilibrium Isotherms.

The effect of temperature on sorption capacity was investigated in the temperature range of 298 K to 318 K. The interaction between N-CNTs-β-CD and Fe/N-CNTs-β-CD with BPA is presented in the form of equilibrium data (experimental data) (Figures 5 and 6). The experimental data show that sorption capacity of BPA is insensitive to temperature. The temperature range used did not cause any effect simply because the temperature difference was not large. Environmental water sources do not have temperatures beyond 318 K. As such, it was not worthwhile to carry out the sorption studies beyond this temperature. In Figure 5(a), a rectangular type isotherm was observed in which the curve rose sharply in the initial stages, demonstrating that there was an abundance of readily available sites. This was followed by an asymptotic plateau indicating that the sorbent was now saturated, that is, formation of monolayer. In the presence of Fe in the nanocomposite, the rate of BPA sorption was much faster (Figure 6(a)).

Solid-liquid equilibrium can be easily described by sorption isotherms. To model the isotherm data, the Langmuir and Freundlich models are often used. From (3) linear curves were obtained by plotting C_e/q_e versus C_e for the Langmuir isotherm and $\ln C_e$ versus $\ln q_e$ for the Freundlich isotherm. The plots of C_e/q_e versus C_e are used to determine Langmuir parameters. The data fit quite well to the Langmuir model for

the Fe/N-CNTs-β-CD nanocomposites as all R^2 values were 1.000. Q_{max} was $80.65 \text{ mg}\cdot\text{g}^{-1}$ for Fe/N-CNTs-β-CD and was independent of temperature. The Freundlich isotherm plots are presented in Figures 5(c) and 6(c). It was also observed that data fitted fairly well. From the plots, the Langmuir and Freundlich isotherm parameters are summarized in Table 2. There was a minor change in the Freundlich isotherm parameters with a change in temperature.

Linear regression has been developed as the most important option in designing sorption systems but may produce inconsistency (between the predictions and experimental data). Depending on the way adsorptive equation is linearized, the error distribution changes can worsen. This has attested the utilization of nonlinearized models in conjunction with number of error analysis techniques [27, 40]. A comparison of SSE for the two isotherms is also listed in Table 2. From the SSE values, the Langmuir isotherm was the most suitable for the experimental data compared to the Freundlich isotherm.

3.4. Adsorption Kinetics

3.4.1. Effect of Mass. Figure 7 shows the uptake-time plots for the study of the effect of the mass of Fe/N-CNTs-β-CD use on sorption kinetics. The uptake of BPA was rapid and dependent on the mass of the sorbent. The rapid rate of the sorption was attributed to the size of the particles. In sorption, sorbent particle size affects the kinetics of uptake since as particle size changes, also the diffusion path changes. Small particles exhibit faster sorption kinetics due to reduced diffusional path or resistance. The kinetic data presented in Figure 7(a) were further modelled using pseudo-first-order, pseudo-second-order, and Elovich models in an attempt to extract model parameters and to determine which model offers the best description of the data. The data fitting to the linearized pseudo-first-order model (8) is presented in Figure 7(b). Linear curves were obtained only up to the 60th minute, beyond which the curves became nonlinear (this part is not shown in Figure 7(b)) suggesting that this model did not sufficiently describe the experimental data. Figure 7(c) shows the data fitted to the linear form of the pseudo-second-order model (10). Evidently, the correlation between the experimental data over the time period and the theoretical data was good for this model. All the correlation coefficients, R^2 , were >0.99 . For the Elovich model, the experimental data fitted to the linear form (12) is summarized in Figure 7(d). Similar to the case of the pseudo-first-order model, linear curves were only obtained up to the 60th minute.

The model parameter values are summarized in Table 3. The parameters depend on sorbent mass. For instance, the k_2 value increased with an increase in sorbent mass. This was due to the fact that the BPA concentration in the solution was rapidly reduced as mass of sorbent was increased. The mass of the sorbent is related to the number of active sites for sorption and both of these increase in parallel [41]. The active sites determine the extent and rate of sorption. Furthermore, the SSE was used to determine the best fit model since linear regression has some inherent weakness. Minimum SSE for

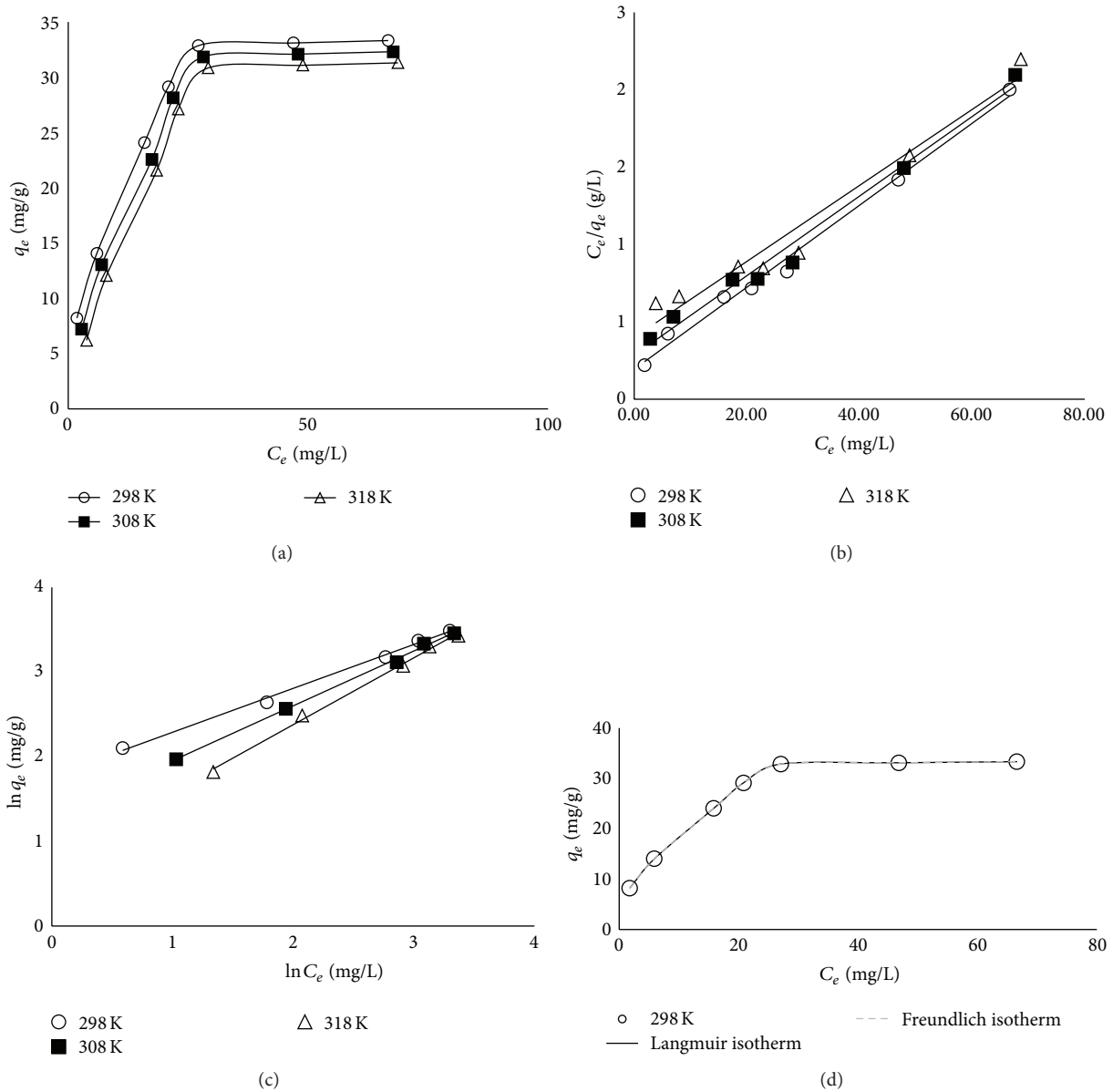


FIGURE 5: (a) Adsorption isotherm of BPA in aqueous solution (1), (b) linearized Langmuir isotherm (3) for BPA adsorption, (c) linearized Freundlich isotherm (5) at temperatures 298 K, 308 K, and 318 K, and (d) Langmuir and Freundlich isotherms ((2) and (4), resp.) obtained using nonlinear fitting onto N-CNTs-β-CD at 298 K. Sorbent dose = 0.05 g/50 mL solution.

TABLE 2: Langmuir and Freundlich isotherm parameters at three temperatures for the sorption of BPA by N-CNTs-β-CD and Fe/N-CNTs-β-CD.

Temperature (K)	Langmuir			SSE	K_F	Freundlich		%SSE
	Q_{max} (mg/g)	b_L (L/mg)	R^2			n	R^2	
N-CNTs-β-CD								
298	38.20	0.12	0.98	0.00	6.80	2.40	0.94	0.001
308	39.40	0.08	0.97	0.00	6.80	2.00	0.92	0.000
318	41.50	0.06	0.95	0.00	3.40	1.70	0.90	0.000
Fe/N-CNTs-β-CD								
298	80.65	11.27	1.00	0.00	102.82	2.26	0.99	0.001
308	80.65	9.54	1.00	0.00	116.08	1.92	0.98	0.006
318	80.65	8.86	1.00	0.00	125.67	1.73	0.97	0.006

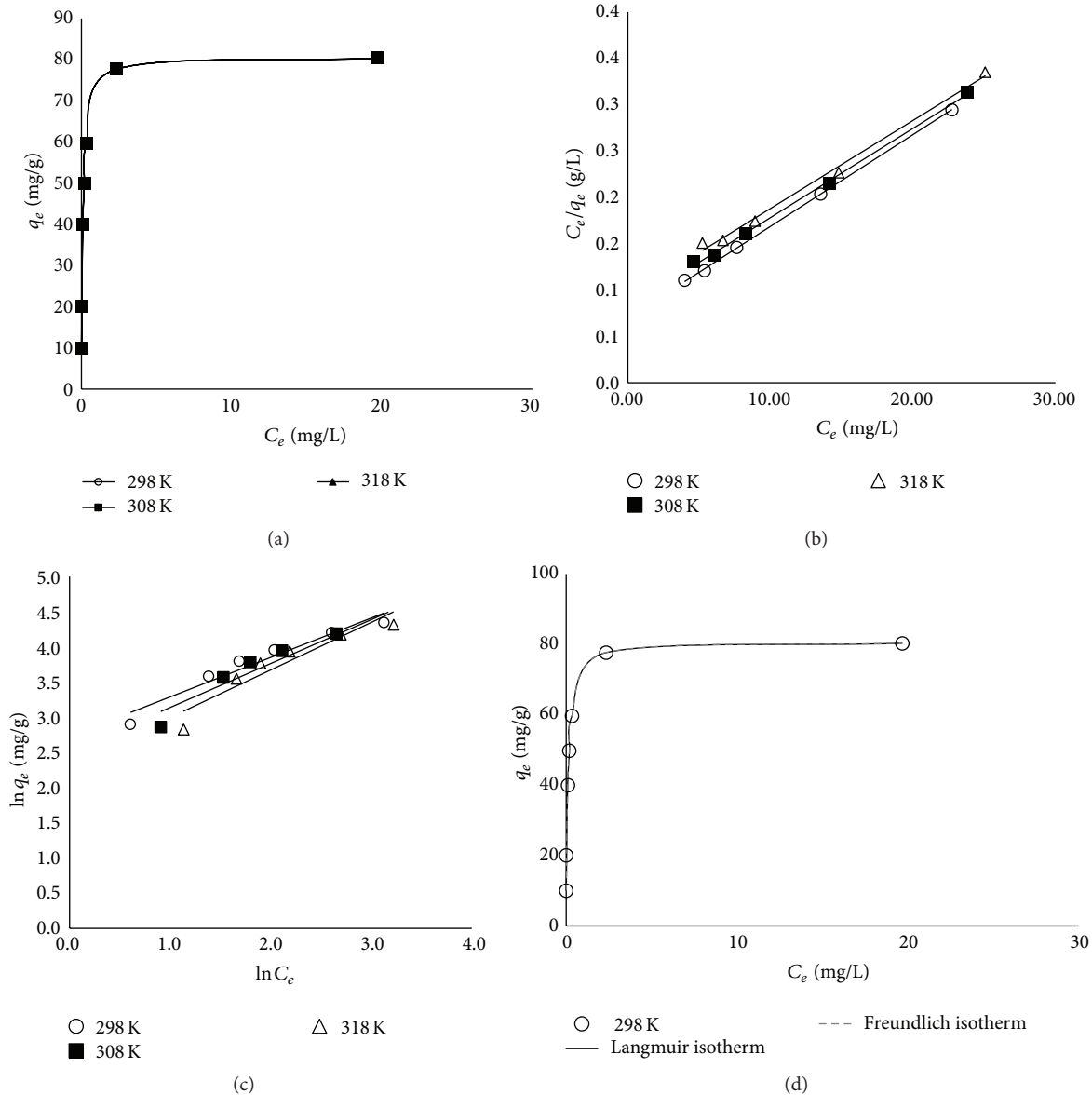


FIGURE 6: (a) Adsorption isotherm of BPA in aqueous solution (1), (b) linearized Langmuir isotherm (3) for BPA adsorption, (c) linearized Freundlich isotherm (5) at temperatures 298 K, 308 K, and 318 K, and (d) Langmuir and Freundlich isotherms ((2) and (4), resp.) obtained using nonlinear fitting onto Fe/N-CNTs-β-CD at 298 K. Sorbent dose = 0.05 g/50 mL solution.

the sorption of BPA onto Fe/N-CNTs-β-CD was obtained for the pseudo-second-order model.

3.4.2. Effect of Initial Concentration. The kinetics of BPA uptake for various initial concentrations are shown in Figure 8(a). The uptake of BPA was fast in the first 60 min, after which equilibrium was achieved for all the BPA initial concentrations used. Compared with bulk activated carbon reported by Li et al. [8], the kinetic performance of Fe/N-CNTs-β-CD in BPA uptake was much faster. As already discussed in Section 3.4.1, the nanomaterials resulted in reduced resistance to mass transfer and increased surface area, hence the faster uptake of BPA seen in this study. Generally, the uptake of BPA increased with an increase in

initial concentration. The sorption of BPA is a passive process driven by concentration gradient as a driving force. The higher the initial concentration, the higher the driving force leading to a higher uptake rate [42, 43].

The kinetic data was further fitted to the linear forms of the pseudo-first-order, pseudo-second-order, and Elovich model at different initial BPA concentrations. The modelling plots are given in Figures 8(b), 8(c), and 8(d). The pseudo-first-order and Elovich models plots were only linear up to the 60th min (nonlinear section omitted). The pseudo-second-order model gave a good fit over the entire sorption period. The extracted model parameters are summarized in Table 4. Overall, the model parameters were dependent on the initial concentration of BPA although no trend was visible. Whereas

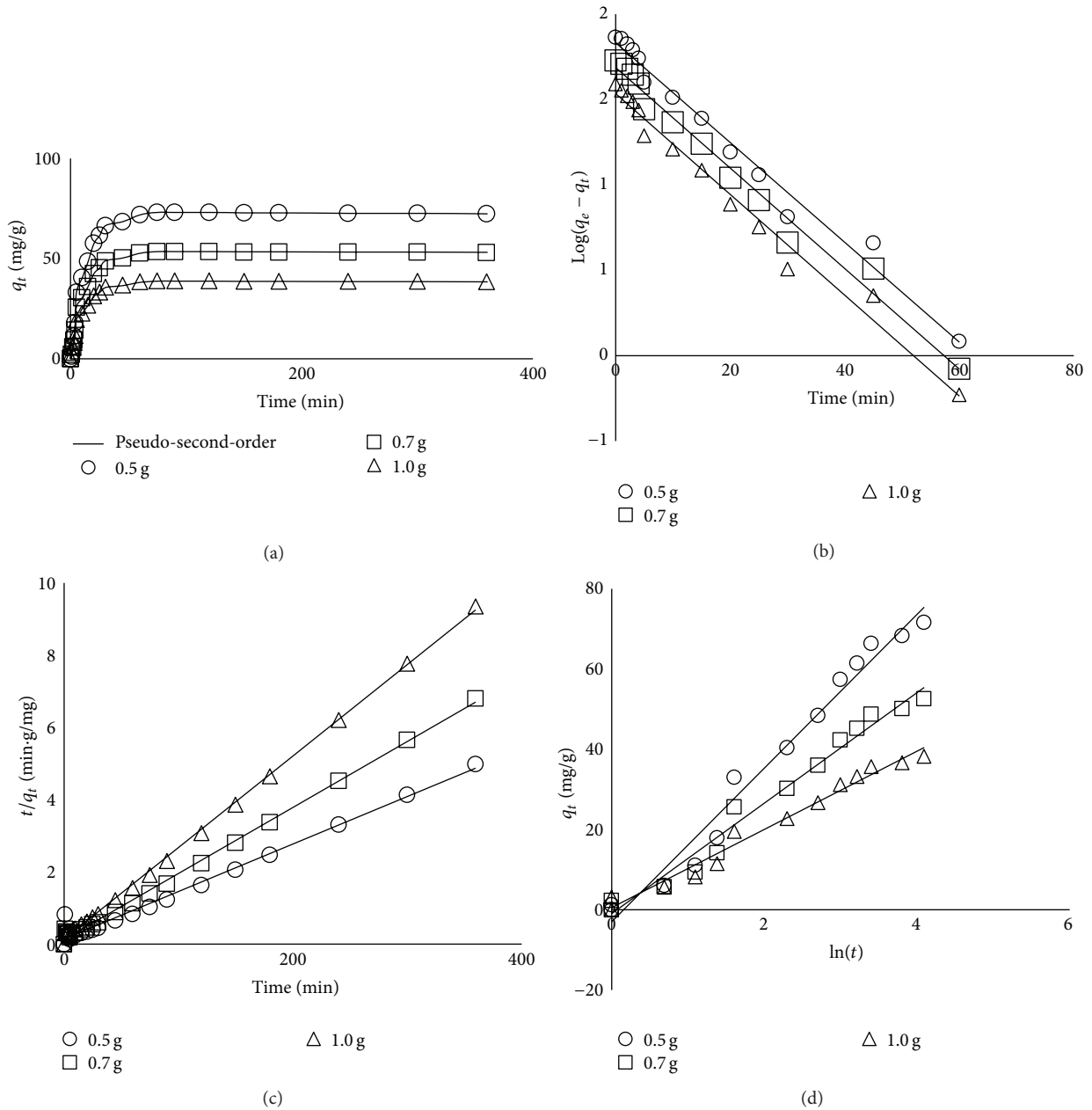


FIGURE 7: The influence contact time on the sorption capacity of BPA for different mass of Fe/N-CNTs-β-CD: (a) nonlinear fitting of pseudo-second-order model, (b) linearized pseudo-first-order kinetic model (8), (c) linearized pseudo-second-order kinetic model (10), and (d) linearized Elovich model (12) obtained at 298 K, 1000 mL solution.

TABLE 3: Pseudo-first-order, pseudo-second-order, and Elovich kinetic models parameters at 298 K, with an initial concentration of 50 mg·L⁻¹ and volume of 1000 mL for Fe/N-CNTs-β-CD with different masses: 0.5 g, 0.7 g, and 1.0 g.

Mass (g)	$q_{e,exp}$ (mg·g ⁻¹)	Pseudo-first-order kinetic model				Pseudo-second-order kinetic model				Elovich kinetic model			
		K_1 (1/min)	$q_{e,cal}$ (mg·g ⁻¹)	R^2	SSE	K_2 (g/mg·min)	$q_{e,cal}$ (mg·g ⁻¹)	R^2	SSE*	α (mg/g·min)	β	R^2	SSE
0.50	72.90	0.067	67.87	0.98	14.00	0.001	76.34	0.99	7.01	16.33	0.05	0.98	7.11
0.70	53.40	0.067	47.97	0.98	18.01	0.002	54.64	1.00	12.00	12.78	0.07	0.98	16.95
1.00	38.90	0.068	34.08	0.98	10.99	0.004	39.52	1.00	4.97	10.24	0.10	0.98	5.00

*Values represent the minimum sum of square error (SSE).

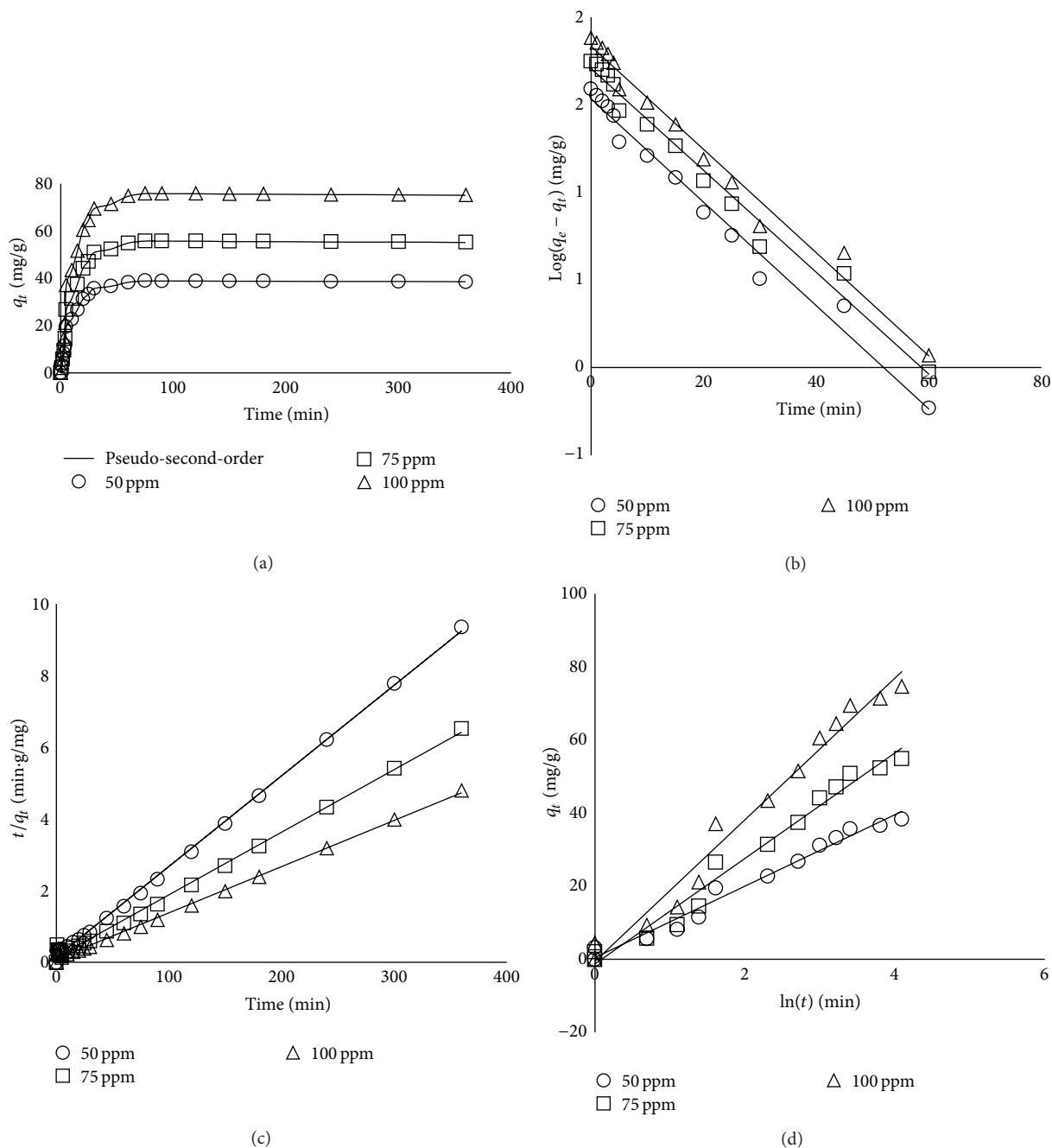


FIGURE 8: The influence contact time on the sorption capacity of BPA for different concentrations of Fe/N-CNTs-β-CD: (a) nonlinear fitting of pseudo-second-order model, (b) linearized pseudo-first-order kinetic model (8), (c) linearized pseudo-second-order kinetic model (10), and (d) linearized Elovich model (12) obtained at 298 K, 1000 mL solution.

TABLE 4: Pseudo-first-order, pseudo-second-order, and Elovich kinetic models parameters at 298 K for Fe/N-CNTs-β-CD at different concentrations of BPA: 50 mg·L⁻¹, 75 mg·L⁻¹, and 100 mg·L⁻¹. Sorbent dose = 1 g/1000 mL solution.

C_o (ppm)	$q_{e,exp}$ (mg·g ⁻¹)	Fe/N-CNTs-β-CD											
		Pseudo-first-order kinetic model				Pseudo-second-order kinetic model				Elovich kinetic model			
		K_1 (1/min)	$q_{e,cal}$ (mg·g ⁻¹)	R^2	SSE	K_2 (g/mg·min)	$q_{e,cal}$ (mg·g ⁻¹)	R^2	SSE*	α (mg/g·min)	β	R^2	SSE
50	38.90	0.007	34.08	0.98	15.80	0.004	39.52	1.00	4.97	10.24	0.10	0.98	5.00
75	55.80	0.007	50.71	0.98	5.00	0.002	55.18	1.00	8.00	10.15	0.07	0.98	8.11
100	75.90	0.007	68.02	0.98	7.00	0.002	77.52	1.00	8.99	18.82	0.05	0.98	8.99

* Values represent the minimum sum of square error (SSE).

TABLE 5: Thermodynamic parameters for the sorption of BPA at different temperatures by N-CNTs- β -CD and Fe/N-CNTs- β -CD adsorbents.

Sorbent	ΔH° (kJ·mol ⁻¹)	ΔS° (J/mol·K)	ΔG° (kJ·mol ⁻¹)		
			298 K	308 K	318 K
N-CNTs- β -CD	-40.92	-125.00	-3.65	-2.48	-1.15
Fe/N-CNTs- β -CD	-1.33	41.60	-13.73	-14.15	-14.15

the pseudo-second-order model provided a fair prediction of the experimental uptake values ($q_{e,exp.}$), the equilibrium uptake values predicted by the pseudo-first-order model were relatively low. This indicated that the pseudo-first-order model did not describe the BPA-Fe/N-CNTs- β -CD interaction. From the linear regression coefficients and SSE values, it could be concluded that both the pseudo-second-order and Elovich models gave a satisfactory description of experimental data.

3.5. Sorption Thermodynamics. A thermodynamic consideration of sorption processes is essential to determine whether the process is spontaneous or not. Gibbs's free energy change, ΔG° , is the essential measure of spontaneity [44]. A reaction occurs spontaneously at a given temperature if ΔG° is a negative value. The thermodynamic parameters of Gibbs free energy change, ΔG° , enthalpy change, ΔH° , and entropy change, ΔS° , for the adsorption processes were calculated using the equations below:

$$\begin{aligned}\Delta G^\circ &= -RT \ln K_a, \\ \Delta G^\circ &= \Delta H^\circ - T\Delta S^\circ,\end{aligned}\tag{14}$$

where R is universal gas constant (8.314 J·mol⁻¹·K⁻¹) and T is the absolute temperature in K .

A positive value of enthalpy change shows that the process is endothermic, while a negative value indicates an exothermic process. A plot of $\ln K_L$ against $1/T$ should yield a straight line with the intercept of $\Delta S^\circ/RT$ and a slope of $\Delta H^\circ/R$ [45]. The thermodynamic parameters are given in Table 5. The negative values of Gibbs free energy change confirmed the feasibility of the process and indicate the spontaneous nature of sorption of BPA at all the temperatures of all the sorbents studied. The values of ΔG° decreased from -3.65 kJ·mol⁻¹ to -1.15 kJ·mol⁻¹ for adsorbents N-CNTs- β -CD and increased from -13.73 kJ·mol⁻¹ to -14.15 kJ·mol⁻¹ for Fe/N-CNTs- β -CD, indicating that the sorption of BPA on Fe/N-CNTs- β -CD is feasible and spontaneous. The negative value of ΔH° , -40.92 kJ·mol⁻¹ and -1.33 kJ·mol⁻¹ onto N-CNTs- β -CD and Fe/N-CNTs- β -CD, respectively, indicated that the sorption process was exothermic. The negative value of ΔS° for N-CNTs- β -CD indicated a decreased randomness at the solid-solute interface during sorption process possibly due to the rapid saturation of the active sites of these materials, while the positive value of ΔS° for Fe/N-CNTs- β -CD indicated an increased randomness at the solid-solute interface during adsorption process.

4. Conclusions

Stable N-CNTs- β -CD and Fe/N-CNTs- β -CD nanocomposites were successfully prepared and evaluated as sorbents for the removal of BPA from aqueous solution under varying process conditions. The results revealed that dispersing metal nanoparticles onto N-CNTs- β -CD significantly enhances the BPA sorption capacity. From equilibrium studies, it has been shown that the Langmuir isotherm model gives a good description of experimental data for the metal nanoparticles dispersed N-CNTs- β -CD composite, that is, Fe/N-CNTs- β -CD. Further, the Langmuir monolayer capacity of Fe/N-CNTs- β -CD was 80.65 mg·g⁻¹ at all temperatures. This value is competitive when compared to those reported in open literature. Meanwhile, from the kinetic studies, the uptake of BPA by Fe/N-CNTs- β -CD composite was rapid and followed the pseudo-second-order model. The results obtained thus far give an indication that Fe/N-CNTs- β -CD nanocomposites are a potential sorbent for water treatment applications. Further work is however needed to evaluate the long term stability of the materials and to get some indication of cost, and reusability of the material needs to be evaluated in adsorption-desorption studies.

Conflict of Interests

The authors declare that there is no conflict of interests regarding the publication of this paper.

Acknowledgments

The authors wish to thank the National Research Foundation of South Africa (NRF, SA) under the Nanotechnology Flagship Programme (UID 68705) and the Tshwane University of Technology and the Council for Scientific and Industrial Research (CSIR, Pretoria) for financial support. Sabelo D. Mhlanga is grateful to Dr. D. Saad for her various contributions during preparation of the paper.

References

- [1] G. Xiao, L. Fu, and A. Li, "Enhanced adsorption of bisphenol A from water by acetylaniline modified hyper-cross-linked polymeric adsorbent: effect of the cross-linked bridge," *Chemical Engineering Journal*, vol. 191, pp. 171–176, 2012.
- [2] A. M. Soto, L. N. Vandenberg, M. V. Maffini, and C. Sonnenschein, "Does breast cancer start in the womb?" *Basic & Clinical Pharmacology & Toxicology*, vol. 102, no. 2, pp. 125–133, 2008.

- [3] H. Maruyama, H. Seki, Y. Matsukawa, A. Suzuki, and N. Inoue, "Adsorption behavior of bisphenol-A and diethyl phthalate onto bubble surface in nonfoaming adsorptive bubble separation," *Chemical Engineering Journal*, vol. 141, no. 1-3, pp. 112-118, 2008.
- [4] Z.-X. Yang, Y. Chen, and Y. Liu, "Inclusion complexes of bisphenol A with cyclomaltoheptaose (β -cyclodextrin): solubilization and structure," *Carbohydrate Research*, vol. 343, no. 14, pp. 2439-2442, 2008.
- [5] Y. Dong, D. Wu, X. Chen, and Y. Lin, "Adsorption of bisphenol A from water by surfactant-modified zeolite," *Journal of Colloid and Interface Science*, vol. 348, no. 2, pp. 585-590, 2010.
- [6] W. Guo, W. Hu, J. Pan et al., "Selective adsorption and separation of BPA from aqueous solution using novel molecularly imprinted polymers based on kaolinite/ Fe_3O_4 composites," *Chemical Engineering Journal*, vol. 171, no. 2, pp. 603-611, 2011.
- [7] W.-T. Tsai, H.-C. Hsu, T.-Y. Su, K.-Y. Lin, and C.-M. Lin, "Adsorption characteristics of bisphenol-A in aqueous solutions onto hydrophobic zeolite," *Journal of Colloid and Interface Science*, vol. 299, no. 2, pp. 513-519, 2006.
- [8] Z. Li, M. A. Gondal, and Z. H. Yamani, "Preparation of magnetic separable CoFe_2O_4 /PAC composite and the adsorption of bisphenol A from aqueous solution," *Journal of Saudi Chemical Society*, vol. 18, no. 3, pp. 208-213, 2014.
- [9] G. Liu, J. Ma, X. Li, and Q. Qin, "Adsorption of bisphenol A from aqueous solution onto activated carbons with different modification treatments," *Journal of Hazardous Materials*, vol. 164, no. 2-3, pp. 1275-1280, 2009.
- [10] E. Yiantzi, E. Psillakis, K. Tyrovolas, and N. Kalogerakis, "Vortex-assisted liquid-liquid microextraction of octylphenol, nonylphenol and bisphenol-A," *Talanta*, vol. 80, no. 5, pp. 2057-2062, 2010.
- [11] M. Gómez, G. Garralón, F. Plaza, R. Vílchez, E. Hontoria, and M. A. Gómez, "Rejection of endocrine disrupting compounds (bisphenol A, bisphenol F and triethyleneglycol dimethacrylate) by membrane technologies," *Desalination*, vol. 212, no. 1-3, pp. 79-91, 2007.
- [12] Z. Peng, F. Wu, and N. Deng, "Photodegradation of bisphenol A in simulated lake water containing algae, humic acid and ferric ions," *Environmental Pollution*, vol. 144, no. 3, pp. 840-846, 2006.
- [13] C. P. Silva, M. Otero, and V. Esteves, "Processes for the elimination of estrogenic steroid hormones from water: a review," *Environmental Pollution*, vol. 165, pp. 38-58, 2012.
- [14] S. Barnabé, S. K. Brar, R. D. Tyagi, I. Beauchesne, and R. Y. Surampalli, "Pre-treatment and bioconversion of wastewater sludge to value-added products—fate of endocrine disrupting compounds," *Science of the Total Environment*, vol. 407, no. 5, pp. 1471-1488, 2009.
- [15] N. Yeddou and A. Bensmaili, "Kinetic models for the sorption of dye from aqueous solution by clay-wood sawdust mixture," *Desalination*, vol. 185, no. 1-3, pp. 499-508, 2005.
- [16] I. Ali, M. Asim, and T. A. Khan, "Low cost adsorbents for the removal of organic pollutants from wastewater," *Journal of Environmental Management*, vol. 113, pp. 170-183, 2012.
- [17] Y. P. Chin, S. Mohamad, and M. R. B. Abas, "Removal of parabens from aqueous solution using β -Cyclodextrin cross-linked polymer," *International Journal of Molecular Sciences*, vol. 11, no. 9, pp. 3459-3471, 2010.
- [18] M. Kitaoka and K. Hayashi, "Adsorption of bisphenol A by cross-linked β -cyclodextrin polymer," *Journal of Inclusion Phenomena*, vol. 44, no. 1-4, pp. 429-431, 2002.
- [19] H. Yamasaki, Y. Makihata, and K. Fukunaga, "Efficient phenol removal of wastewater from phenolic resin plants using crosslinked cyclodextrin particles," *Journal of Chemical Technology & Biotechnology*, vol. 81, no. 7, pp. 1271-1276, 2006.
- [20] R. W. M. Krause, B. B. Mamba, L. N. Dlamini, and S. H. Durbach, "Fe-Ni nanoparticles supported on carbon nanotube-co-cyclodextrin polyurethanes for the removal of trichloroethylene in water," *Journal of Nanoparticle Research*, vol. 12, no. 2, pp. 449-456, 2010.
- [21] P. Ayala, R. Arenal, M. Rümmele, A. Rubio, and T. Pichler, "The doping of carbon nanotubes with nitrogen and their potential applications," *Carbon*, vol. 48, no. 3, pp. 575-586, 2010.
- [22] S. Klimkova, M. Cernik, L. Lacinova, J. Filip, D. Jancik, and R. Zboril, "Zero-valent iron nanoparticles in treatment of acid mine water from in situ uranium leaching," *Chemosphere*, vol. 82, no. 8, pp. 1178-1184, 2011.
- [23] S. Qi and L. C. Schideman, "An overall isotherm for activated carbon adsorption of dissolved natural organic matter in water," *Water Research*, vol. 42, no. 13, pp. 3353-3360, 2008.
- [24] Y. S. Ho and G. McKay, "Pseudo-second order model for sorption processes," *Process Biochemistry*, vol. 34, no. 5, pp. 451-465, 1999.
- [25] D. H. Lataye, I. M. Mishra, and I. D. Mall, "Adsorption of 2-picoline onto bagasse fly ash from aqueous solution," *Chemical Engineering Journal*, vol. 138, no. 1-3, pp. 35-46, 2008.
- [26] W. Plazinski, W. Rudzinski, and A. Plazinska, "Theoretical models of sorption kinetics including a surface reaction mechanism: a review," *Advances in Colloid and Interface Science*, vol. 152, no. 1-2, pp. 2-13, 2009.
- [27] K. Y. Foo and B. H. Hameed, "Insights into the modeling of adsorption isotherm systems," *Chemical Engineering Journal*, vol. 156, no. 1, pp. 2-10, 2010.
- [28] Y. Ju-Nam and J. R. Lead, "Manufactured nanoparticles: an overview of their chemistry, interactions and potential environmental implications," *Science of the Total Environment*, vol. 400, no. 1-3, pp. 396-414, 2008.
- [29] M. N. Timofeeff, T. K. Lowenstein, and W. H. Blackburn, "ESEM-EDS: an improved technique for major element chemical analysis of fluid inclusions," *Chemical Geology*, vol. 164, no. 3-4, pp. 171-181, 2000.
- [30] Y.-M. Zheng, S.-F. Lim, and J. P. Chen, "Preparation and characterization of zirconium-based magnetic sorbent for arsenate removal," *Journal of Colloid and Interface Science*, vol. 338, no. 1, pp. 22-29, 2009.
- [31] S. Akgöl and A. Denizli, "Novel metal-chelate affinity sorbents for reversible use in catalase adsorption," *Journal of Molecular Catalysis B: Enzymatic*, vol. 28, no. 1, pp. 7-14, 2004.
- [32] G. Annadurai, L. Y. Ling, and J.-F. Lee, "Adsorption of reactive dye from an aqueous solution by chitosan: isotherm, kinetic and thermodynamic analysis," *Journal of Hazardous Materials*, vol. 152, no. 1, pp. 337-346, 2008.
- [33] S. D. Mhlanga, S. P. Masinga, M. F. Bambo, B. B. Mamba, and E. N. Nxumalo, "A facile procedure to synthesize a three-component β -cyclodextrin polyurethane nanocomposite matrix containing Ag decorated N-CNTs for water treatment," *Nanoscience and Nanotechnology Letters*, vol. 5, no. 3, pp. 341-348, 2013.
- [34] N. Savage and M. S. Diallo, "Nanomaterials and water purification: opportunities and challenges," *Journal of Nanoparticle Research*, vol. 7, no. 4-5, pp. 331-342, 2005.

- [35] T. J. Malefetse, B. B. Mamba, R. W. Krause, and M. M. Mahlambi, "Cyclodextrin-ionic liquid polyurethanes for application in drinking water treatment," *Water SA*, vol. 35, no. 5, pp. 729–734, 2009.
- [36] K. L. Salipira, R. W. Krause, B. B. Mamba, T. J. Malefetse, L. M. Cele, and S. H. Durbach, "Cyclodextrin polyurethanes polymerized with multi-walled carbon nanotubes: synthesis and characterization," *Materials Chemistry and Physics*, vol. 111, no. 2-3, pp. 218–224, 2008.
- [37] K. L. Salipira, B. B. Mamba, R. W. Krause, T. J. Malefetse, and S. H. Durbach, "Carbon nanotubes and cyclodextrin polymers for removing organic pollutants from water," *Environmental Chemistry Letters*, vol. 5, no. 1, pp. 13–17, 2007.
- [38] W.-T. Tsai, C.-W. Lai, and T.-Y. Su, "Adsorption of bisphenol-A from aqueous solution onto minerals and carbon adsorbents," *Journal of Hazardous Materials*, vol. 134, no. 1–3, pp. 169–175, 2006.
- [39] J. Pan, X. Zou, X. Wang, W. Guan, Y. Yan, and J. Han, "Selective recognition of 2,4-dichlorophenol from aqueous solution by uniformly sized molecularly imprinted microspheres with β -cyclodextrin/attapulgite composites as support," *Chemical Engineering Journal*, vol. 162, no. 3, pp. 910–918, 2010.
- [40] J. Lin and L. Wang, "Comparison between linear and non-linear forms of pseudo-first-order and pseudo-second-order adsorption kinetic models for the removal of methylene blue by activated carbon," *Frontiers of Environmental Science and Engineering in China*, vol. 3, no. 3, pp. 320–324, 2009.
- [41] A. Gürses, Ç. Doğar, M. Yalçın, M. Açıkıldiz, R. Bayrak, and S. Karaca, "The adsorption kinetics of the cationic dye, methylene blue, onto clay," *Journal of Hazardous Materials*, vol. 131, no. 1–3, pp. 217–228, 2006.
- [42] Y.-S. Ho, C.-C. Chiang, and Y.-C. Hsu, "Sorption kinetics for dye removal from aqueous solution using activated clay," *Separation Science and Technology*, vol. 36, no. 11, pp. 2473–2488, 2001.
- [43] M. Bhaumik, T. Y. Leswif, A. Maity, V. V. Srinivasu, and M. S. Onyango, "Removal of fluoride from aqueous solution by polypyrrole/Fe₃O₄ magnetic nanocomposite," *Journal of Hazardous Materials*, vol. 186, no. 1, pp. 150–159, 2011.
- [44] D. G. Myszk, "Kinetic, equilibrium, and thermodynamic analysis of macromolecular interactions with BIACORE," in *Methods in Enzymology*, G. K. A. Michael and L. Johnson, Eds., pp. 325–340, Academic Press, 2000.
- [45] I. I. Fasfous, E. S. Radwan, and J. N. Dawoud, "Kinetics, equilibrium and thermodynamics of the sorption of tetrabromobisphenol A on multiwalled carbon nanotubes," *Applied Surface Science*, vol. 256, no. 23, pp. 7246–7252, 2010.

Research Article

Experimental Study and Stabilization Mechanisms of Silica Nanoparticles Based Brine Mud with High Temperature Resistance for Horizontal Shale Gas Wells

Xian-yu Yang, Ye Yue, Ji-hua Cai, Yue Liu, and Xiao-ming Wu

School of Engineering, China University of Geosciences, Wuhan 430074, China

Correspondence should be addressed to Ji-hua Cai; catchercai@hotmail.com

Received 22 July 2015; Revised 10 October 2015; Accepted 12 October 2015

Academic Editor: Sesha Srinivasan

Copyright © 2015 Xian-yu Yang et al. This is an open access article distributed under the Creative Commons Attribution License, which permits unrestricted use, distribution, and reproduction in any medium, provided the original work is properly cited.

Previous studies showed that silica nanoparticles based fresh water drilling muds had good thermal stability up to 160°C; however its performance at high salt concentration was rather poor. Therefore, high performance silica nanoparticles based brine mud (NPBMs) with high temperature resistance for horizontal shale gas wells was proposed. Thermal stability tests from ambient temperature to 180°C, along with pressure transmission tests and rheology analysis, were performed to evaluate comprehensive properties of the NPBMs. Results show that the NPBMs embody excellent salt tolerance and thermal resistance for their rheological parameters did not suffer significant fluctuation. Fluid loss of the NPBM-1 (4% NaCl plus 3% KCl) at 180°C was only 7.6 mL while the NPBM-2 (10% NaCl plus 3% KCl) had a fluid loss of 6.6 mL at 150°C. Low water activity and good lubricity of the NPBMs were beneficial to improve wellbore stability and reduce friction resistance. Pressure transmission tests on the NPBM-1 show that it can mitigate or even prevent the transmission of drilling mud pressure into shale thus improving wellbore stability. Additionally, optimal rheological models for the NPBM-1 and the NPBM-2 were Herschel-Bulkley model and Power Law model separately.

1. Introduction

Fluid penetration from water-based drilling mud into shale formations results in swelling and subsequent wellbore instability. Shale accounts for 75% of all footage drilled and is responsible for 90% of wellbore stability problems [1–3]. Maintaining wellbore stability is one of the most critical aspects of oil and gas drilling. The main cause of shale instability for both soft and hard shale is water absorption and subsequent swelling and sloughing of the wellbore [4]. Wellbore pressure penetrates into the pore space when water invades into the shale. This reduction of true overbalance, which acts like a support pressure for the hole, can result in shale failure and wellbore instability [5].

It is generally accepted that balanced activity oil-continuous mud offers a good solution to shale instability problems since there is no interaction between oil and shale [4]. However, for environmental and economic considerations, water-based mud would be much preferred if the interaction between drilling mud and shale could be minimized. Hayatdavoudi and Apende [6] found that the best

possible way of preventing contact between argillaceous rock and water is to seal off exposed clayey surfaces. Carminati et al. [7] showed that the most effective additives in controlling the pore fluid pressure in the formation and the shale hardness, and consequently in preventing shale instability, are the silicates. Pore blocking is a time dependent process that requires a few hours to develop. Van Oort et al. [3] introduced silicate-based mud as superior fluids for drilling troublesome formations like intact and (micro)fractured shale and chinks. In addition, these inorganic systems are environmentally friendly and inexpensive. Reid et al. [8] regarded the interaction between potassium ions and polyols at the clay surface as the critical factor in the provision of shale inhibition. Zhong et al. [9] elaborated the mechanisms of polyether diamine to improve shale wellbore stability in water-based drilling fluids.

Different from traditional sandstone or carbonate reservoirs, shale from China and North America is featured with nanosized pores. The pore diameter of gas shale in China and North America is in a range of 5–300 nm and 8–100 nm separately [10–16]. Therefore, only nanoparticles

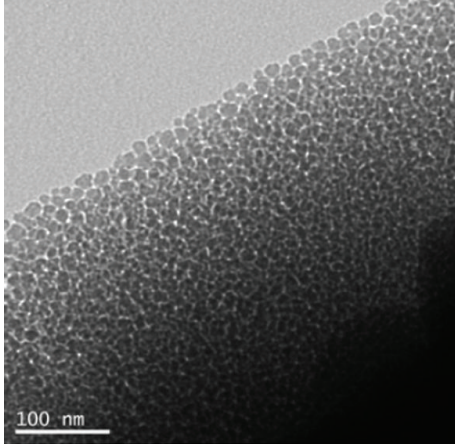


FIGURE 1: TEM picture of nano-SiO₂ dispersion.

have the possibility of plugging pore throats in shale. On the other side, Cai et al. [17], Sharma et al. [18], Akhtarmanesh et al. [19], Kapadnis et al. [20], and Liang et al. [21] found that wellbore stability of shale could be improved with nanoparticles. For shale gas wells, especially the ones with long intervals, good cutting transferring capability, excellent inhibition on shale to absorb water, and good lubricity to decrease circulating friction resistance become the focuses of designing inhibitive drilling mud.

Our previous studies have showed that silica nanoparticles (nano-SiO₂) based fresh water mud could improve wellbore stability of shale and had good thermal stability up to 160°C [17, 22]. However, its performance at high salt concentration was rather poor as the American Petroleum Institute (API) filtration was over 15 mL at 120°C. In this paper, basing on synergic wellbore stabilization theory of physical plugging of nanoparticles, balanced activity with inorganic salts, chemical inhibition, and rational mud density, high performance silica nanoparticles (nano-SiO₂) based brine mud (NPBMs) with high temperature resistance for horizontal shale gas wells was proposed. The thermal stability tests on rheology, filtration, lubricity, and water activity of the NPBMs from ambient temperature to 180°C were carried out and pressure transmission tests were run to systematically evaluate the performances of the NPBMs. In addition, rheological model of the NPBMs was also analyzed.

2. Material and Methods

2.1. Material

2.1.1. Nanoparticles. Nano-SiO₂ used in this study was milky white dispersion and had a concentration of 30%. It was procured from Nanjing Haitai Nano Materials Co., Ltd., China. Its transmission electron microscopy (TEM) picture is shown in Figure 1. The diameter of nano-SiO₂ ranges between 10 nm and 20 nm.

2.1.2. Shale Properties. Shale is a sedimentary rock that mineralogically consists of clays, quartz, and other silicate and carbonate minerals. Because of its high clay content, shale

TABLE 1: Composition of shale samples from the first shale gas well of Jiangxi, China.

X-ray diffraction	wt/%
Chlorite	25
Illite	20
Calcite	15
Feldspar	10
Gypsum	3
Pyrite	5
Quartz	22

tends to absorb water from water-based mud, which results in swelling and sloughing of the wellbore. In this study, core samples from the first shale gas well of Jiangxi, China, were obtained. The mineralogical composition of this shale is listed in Table 1. It contains 45% clay minerals (25% chlorite plus 20% illite) showing strong water sensitivity and moderate brittleness.

2.1.3. Mud Used. The NPBMs with high temperature resistance were developed through basic formula optimization. A 4% NaCl brine mud and 10% NaCl brine mud were obtained separately. Both mud types contain clay (1.5% attapulgite, 1.5% sodium bentonite), nanoparticles (2% nano-SiO₂), fluid loss additives (0.3% LV-CMC, 1% Dristemp, and 2% lockseal), shale inhibitors (3% KL, 3% SPNH, 2% Soltex, 2% SMP-II, and 3% KCl), pH regulator (Na₂CO₃), and weighting material (10% BaSO₄). The concentration of BaSO₄ could also be adjusted according to the pore pressure of the formation. The 4% NaCl and 10% NaCl NPBM contained 0.14% Na₂CO₃ and 0.2% Na₂CO₃ separately and were denoted as NPBM-1 and NPBM-2. Among the additives used, attapulgite was bought from Anhui Mingyuan New Material Co., Ltd., China. Sodium bentonite was supplied by Weifang Huixin Bentonite Co., Ltd., Shandong, China. LV-PAC, SPNH, KL, and SMP-II were offered by East Zhengzhou Drilling Additive Co., Ltd., China. Dristemp and Soltex were supplied by Chevron Phillips Chemical Company LP. NaCl, KCl, Na₂CO₃, and BaSO₄ were standard chemical reagents bought from Sinopharm Chemical Co. Ltd.

2.2. Experimental Methods

2.2.1. Thermal Stability Tests. The thermal stability tests consisted of heating the brine mud (BM) and the NPBMs to a given temperature from ambient temperature to 180°C for 16 h with OFITE roller oven and then cooling it to ambient temperature. The rheological properties were evaluated by a ZNN-D6 six-speed rotary viscometer. The readings at 600 rpm and 300 rpm could be marked as θ_{600} and θ_{300} , respectively. The plastic viscosity (PV) and yield point (YP) could be calculated according to the equations as follows:

$$\begin{aligned} PV &= \theta_{600} - \theta_{300}, \text{ mPa} \cdot \text{s} \\ YP &= 0.5 (2\theta_{300} - \theta_{600}), \text{ Pa.} \end{aligned} \quad (1)$$

The initial gel strength (τ_{10s}) and the final gel strength (τ_{10min}) of the BM and the NPBMs were also measured with the ZNN-D6 six-speed rotary viscometer.

TABLE 2: Rheological properties of BM with/without nanoparticles.

Formula	Temperature	PV (mPa·s)	YP (Pa)
BM-1	25°C	45	23
	120°C	67	31
	150°C	66	16.5
	180°C	63	17.5
BM-2	25°C	42	25
	120°C	57	32
	150°C	61	26
	180°C	51	23.5
NPBM-1	25°C	52	26
	120°C	66	32
	150°C	66	17
	180°C	76	22
NPBM-2	25°C	50	29
	120°C	67	32
	150°C	58	27
	180°C	47	20.5

TABLE 3: Gel strength of the BM with or without nanoparticles at elevated temperature.

Temperature	τ_{10s}/τ_{10min} (Pa/Pa)			
	BM-1	BM-2	NPBM-1	NPBM-2
25°C	2/6	1.5/4	2.5/8	2.1/6
120°C	1.5/2.5	1.5/2.5	1.6/2.6	1.6/2.6
150°C	2.5/7.5	2.5/6	2.4/5	2/4
180°C	2.5/4	2.1/5.5	2/3.2	2/3.3

After that, the filtration properties of the NPBM-1s were tested for 30 minutes by a ZNS-5A moderate pressure filter press with a pressure difference of 0.69 MPa at ambient temperature (25°C). The friction coefficient was measured with EP-2 extreme pressure lubricity tester. The motor speed was adjusted to 60 rpm and the torque was loaded to 15.96 N·m. The test procedures followed the API standards. Novasina Labswift water activity tester was used to analyze the water activity of drilling mud. The results were shown in Tables 2 and 3 and Figures 2–5.

2.2.2. High Temperature and High Pressure (HTHP) Rheological Tests. Fann 50SL rheometer was employed to evaluate the HTHP rheological properties at 5.17 MPa. The temperature range was set from 25°C to 180°C. The readings at 100 rpm of the rheometer were derived and the rheological curve was drawn, as shown in Figure 6.

2.2.3. Pressure Transmission Tests. The interaction between varied working fluids with shale was investigated by HKY-3 pressure transmission test apparatus. The shale samples used were collected from the first shale gas well of Jiangxi, China, and had similar original permeability. The confining pressure and upstream pressure were set as 3.5 MPa and 2.5 MPa separately while the initial downstream pressure was set as zero. The downstream pressure data was collected for the calculation of permeability (k) of shale sample in contact

with working fluids. It was decided to first flow brine (10% NaCl) through shale samples until equilibrium was reached so as to produce saturated shale samples. For the second step, the test was run using compound brine (7% NaCl plus 3% KCl). In the third step, the test was run using the NPBM-1 at ambient temperature. To verify the capability of the NPBM-1 mitigating pressure penetration into shale, the upstream pressure was increased to 10 MPa in the last step. Table 4 and Figures 7 and 8 present the pressure penetration test results. A transient pressure model is used for calculating the permeability of shale sample [10]. Another similar pressure transmission tests were undergone with the difference that the NPBM-1 at ambient temperature was substituted by the NPBM-1 mud after hot roll at 180°C and being cooled to ambient temperature.

2.2.4. Rheological Model Analyses. Rheological model of the NPBM-1s have important and direct effect on the calculation of circulating pressure loss, pressure surge, cuttings carrying performances and water horse power of drilling bits which are beneficial to rapid drilling, borehole cleaning, and wellbore stabilization. A data processing system (DPS) software was used to analyze the rheological model of the NPBM-1s.

3. Results

3.1. Thermal Stability Tests

3.1.1. Rheology and Filtration. Table 2 and Figure 2 present the PV and YP of the NPBM-1s compared with non-NP mud. Standard deviation data has been also added in Figure 2. The addition of nano-SiO₂ does not show strong influence on the PV and YP of the BM. Up to 10 types of additives had been used; therefore linear increase or decrease of PV or YP did not appear (Figure 2). To the NPBM-1, it experienced an increase of 24 mPa·s for the PV with the increase of temperature, which can be attributed with the fact that high temperature may promote the hydration of sodium bentonite and increase the internal friction of the NPBM-1 with lower salinity (4% NaCl), thus increasing the PV. Its YP suffered a fluctuation from 17 Pa to 32 Pa, which is still acceptable to drilling engineering. Therefore, we conclude that its thermal tolerance is 180°C. To the NPBM-2, for its higher salinity (10% NaCl), its PY dropped about 20 mPa·s when the temperature increased from 120°C to 180°C. Taking its PV at 25°C as a referenced example, we deduce that its temperature tolerance is 150°C.

The initial gel strength (τ_{10s}) and the final gel strength (τ_{10min}) of BM mud with/without the addition of nano-SiO₂ were presented in Table 3. The presence of nanoparticles did not bring significant change to the bentonite mud and showed good compatibility.

Figure 3 shows the filtration properties of the NPBM-1s with the elevation of temperature. For the NPBM-1, the fluid loss was less than 7.6 mL at 180°C while, for the NPBM-2, the fluid loss was below 6.6 mL at 150°C. From 150°C to 180°C, the NPBM-2 experienced higher fluid loss which might be explained for its higher NaCl concentration (10%).

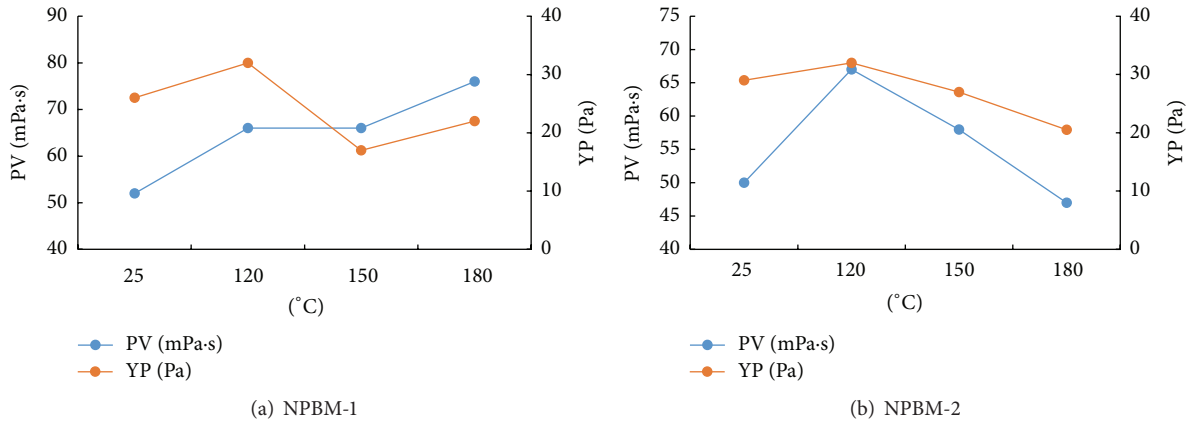


FIGURE 2: Change of plastic viscosity and yield point versus temperature.

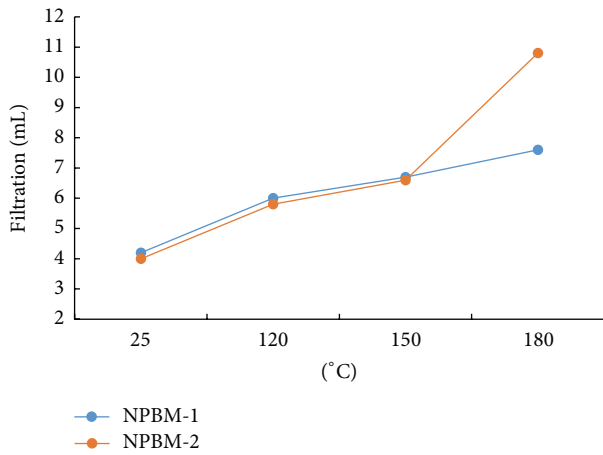


FIGURE 3: Change of fluid loss versus temperature.

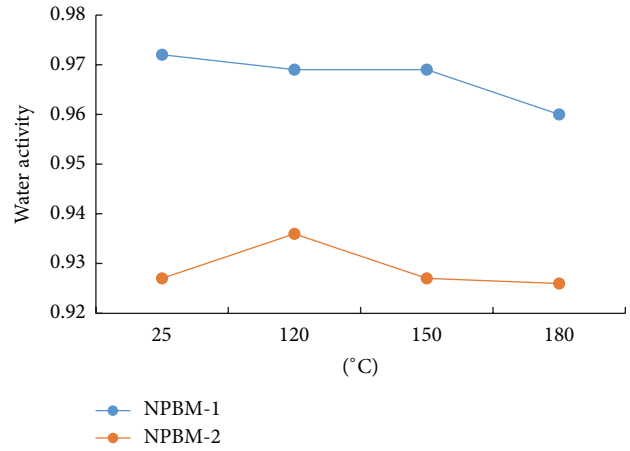


FIGURE 5: Change of water activity versus temperature.

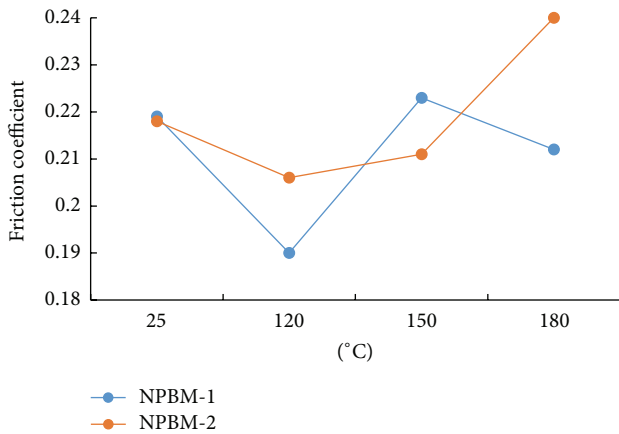


FIGURE 4: Change of friction factor versus temperature.

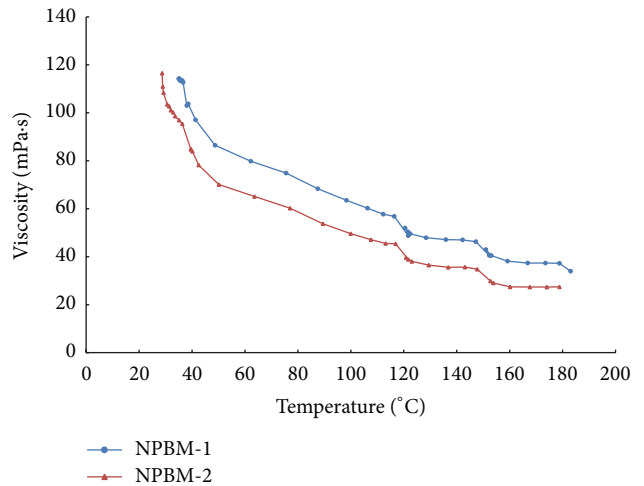


FIGURE 6: HTHP rheological curves of the NPBM-1 and NPBM-2 at 100 rpm.

By integrating Figures 2 and 3 and Tables 2 and 3 together, we found that the NPBM-1 shows excellent properties at high salt concentration up to 13% and high temperature up to 180°C (NPBM-1) or 150°C (NPBM-2).

3.1.2. Lubricity and Water Activity. In the drilling of horizontal shale gas well with long interval, drilling contractors not

only need to face with the technical problem of lost circulation and collapse but also need to reduce friction resistance and ensure the transferring of cuttings. From Figure 4, it is observed that the friction coefficient kept around 0.2 during the increasing of temperature from ambient temperature to

TABLE 4: Testing conditions and results of pressure transmission tests.

Number of shale samples	Testing fluid	Permeability (mD)	Reducing rate of permeability (%)	Testing conditions	Test time (h)
1#	10% NaCl	0.91	—	Upstream pressure: 2.3 MPa Downstream pressure: 0 MPa	3
	7% NaCl + 3% KCl	2.72×10^{-3}	99.7		30
	NPBM-1 at 25°C	1.96×10^{-6}	99.99	40	
	NPBM-1 at 25°C	1.5×10^{-5}	99.99	Upstream pressure: 10 MPa Downstream pressure: 0.02 MPa	30
2#	10% NaCl	1.89	—	Upstream pressure: 2.3 MPa Downstream pressure: 0 MPa	3
	7% NaCl + 3% KCl	2.17×10^{-3}	99.89		30
	NPBM-1 after being rolled at 180°C	4.69×10^{-6}	99.99	60	
	NPBM-1 after being rolled at 180°C	1.29×10^{-5}	99.99	Upstream pressure: 10 MPa Downstream pressure: 0.02 MPa	20

180°C, with fluctuation in a narrow range. Excellent lubricity performance is very beneficial for the reducing of friction resistance of drilling bits and tools.

Lower water activity is helpful to improve wellbore stability of shale to some extent [4]. Figure 5 presents water activity of the NPBM-1 and NPBM-2 from ambient temperature to 180°C. Water activity of the NPBM-1 and NPBM-2 was in the range of 0.96~0.972 and 0.926~0.936, respectively, indicating good thermal resistance. The NPBM-2 had lower water activity than the NPBM-2 for its higher NaCl concentration (10%).

3.2. HTHP Rheological Tests. As shown in Figure 6 both the NPBM-1 and NPBM-2 types endured a decrease of viscosity with the elevation of temperature. However, the NPBM-1 shows better thermal stability than the NPBM-2. It may be attributed to its lower salinity.

3.3. Pressure Transmission Tests. Pressure transmission tests are often used to study the transmission of drilling mud pressure to pore fluid pressure which has critical impact on wellbore stability issue [4, 5, 18, 24]. In this study, HKY-3 pressure transmission test apparatus was used to evaluate whether the NPBM-1 could mitigate the pressure transmission into shale or not. As shown in Table 1, the shale sample from the first shale gas well of Jiangxi, China, has 45% clay and 22% quartz, showing strong water sensitivity and moderate brittleness.

Table 4 and Figures 7 and 8 summarized the testing conditions and results of pressure transmission tests.

In the first step with brine containing 10% NaCl, the upstream pressure penetrated into the downstream fast in about 6 h and the permeability of the shale sample was derived as 0.91 mD, as shown in Table 4 and Figure 7. Then the 10% NaCl was substituted by a compound brine (7% NaCl plus 3% KCl), the upstream pressure penetrated fast into the downstream in about 30 h, and the permeability of the shale sample was derived as 2.72×10^{-3} mD. Compound brine shows much more inhibition effect on the shale sample. After that, the compound brine was substituted by the NPBM-1 and the downstream pressure curve kept flat in about 40 h which shows that the NPBM-1 can mitigate or even prevent the

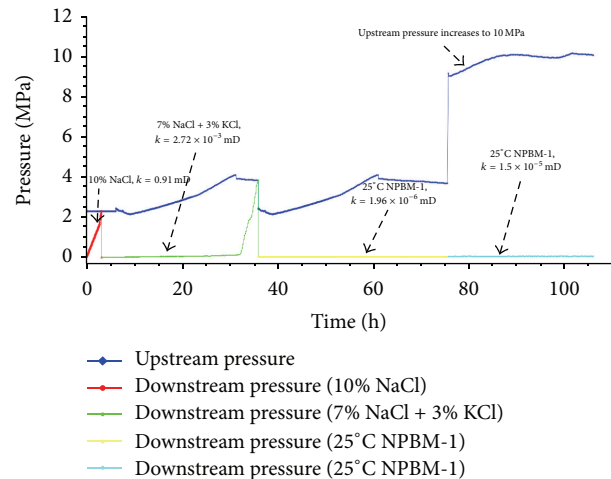


FIGURE 7: Pressure transmission test curves of the shale with brine and the NPBM-1 at ambient temperature.

transmission of upstream pressure (simulated drilling mud pressure). The calculated permeability of the shale sample was 1.96×10^{-6} mD (or 1.96 nD) and the reducing rate of shale permeability compared with brine was 99.99%. To confirm the inhibition effect, the upstream pressure was increased from 3.5 MPa to 10 MPa (Figure 7), the downstream pressure still kept constant for 30 h, and the calculated permeability of the shale was lower as 1.5×10^{-5} mD (or 15 nD). The permeability of shale sample in contact with NPBM-1 at ambient temperature is less than thousandth of the permeability of shale sample with compound brine. Shale permeability decreased from the level of milli-Darcy (mD) to the level of nano-Darcy (nD) showing that the invasion of water from drilling mud into shale sample was restricted to a great extent.

Another similar pressure transmission tests were undergone with the difference that the NPBM-1 at ambient temperature was substituted by the NPBM-1 mud after hot roll at 180°C and being cooled to ambient temperature. The results were shown in Figure 8. In the first step with brine (10% NaCl), similar result was observed to the above and the

TABLE 5: Rheological equation fitting in different temperature of NPBM-1.

Flow pattern	Determination coefficient (R^2), test value (F), and significant level (p)			
	25°C	120°C	150°C	180°C
Bingham	$\tau = 10.431 + 0.073 \times \gamma$ $R^2 = 0.9557$, $F = 86.26$, $p = 0.007$	$\tau = 10.758 + 0.094 \times \gamma$ $R^2 = 0.9578$, $F = 90.69$, $p = 0.007$	$\tau = 5.905 + 0.080 \times \gamma$ $R^2 = 0.9856$, $F = 273.02$, $p = 0.001$	$\tau = 9.787 + 0.093 \times \gamma$ $R^2 = 0.9757$, $F = 273.02$, $p = 0.001$
Power Law	$\tau = 1.440 \times \gamma^{0.579}$ $R^2 = 0.9995$, $F = 8414.51$, $p = 0.000$	$\tau = 1.239 \times \gamma^{0.635}$ $R^2 = 0.9919$, $F = 489.93$, $p = 0.000$	$\tau = 0.504 \times \gamma^{0.740}$ $R^2 = 0.9994$, $F = 7004.41$, $p = 0.000$	$\tau = 0.990 \times \gamma^{0.665}$ $R^2 = 0.9978$, $F = 1827.63$, $p = 0.000$
Carson	$\tau^{1/2} = 3.6146^{1/2} + 0.054^{1/2} \times \gamma^{1/2}$ $R^2 = 0.9874$, $F = 313.75$, $p = 0.001$	$\tau^{1/2} = 3.304^{1/2} + 0.072^{1/2} \times \gamma^{1/2}$ $R^2 = 0.9868$, $F = 298.52$, $p = 0.001$	$\tau^{1/2} = 1.378^{1/2} + 0.067^{1/2} \times \gamma^{1/2}$ $R^2 = 0.9959$, $F = 982.74$, $p = 0.000$	$\tau^{1/2} = 3.099^{1/2} + 0.071^{1/2} \times \gamma^{1/2}$ $R^2 = 0.9943$, $F = 702.67$, $p = 0.000$
Herschel-Bulkley	$\tau = 1.463 + 1.178 \times \gamma^{0.606}$ $R^2 = 1$, $F = 31230$, $p = 0.000$	$\tau = 1.356 + 1.064 \times \gamma^{0.656}$ $R^2 = 0.9922$, $F = 190.19$, $p = 0.007$	$\tau = 1.181 + 0.420 \times \gamma^{0.764}$ $R^2 = 0.9998$, $F = 7393.42$, $p = 0.000$	$\tau = 2.447 + 0.733 \times \gamma^{0.706}$ $R^2 = 0.9988$, $F = 1277.66$, $p = 0.000$

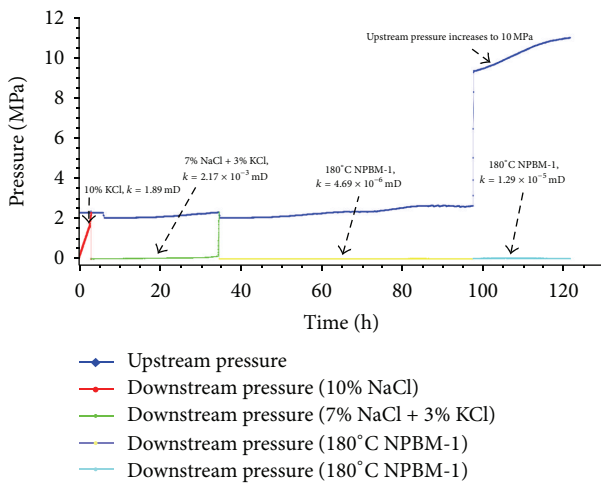


FIGURE 8: Pressure transmission test curves of the shale with brine and the NPBM-1 after being rolled at 180°C.

calculated permeability was 1.89 mD. Then the 10% NaCl was substituted by the compound brine (7% NaCl + 3% KCl), the upstream pressure penetrated fast into the downstream in about 30 h, and the permeability of the shale sample was derived as 2.12×10^{-3} mD. Compound brine still played well than 10% NaCl. After that, the compound brine was substituted by the NPBM-1 after being rolled at 180°C and the downstream pressure still kept flat in about 60 h and the permeability obtained was 4.69×10^{-6} mD (or 4.69 nD). The decreasing rate of shale permeability was as high as 99.99%. Similarly, with the upstream pressure being risen to 10 MPa again, the downstream pressure almost kept constant for 20 h and the calculated permeability of the shale was lower as 1.29×10^{-5} mD (or 12.9 nD). It indicates that, even after hot roll at 180°C, the NPBM-1 still shows excellent capability to mitigate or prevent the penetration of pressure from drilling fluid into the shale sample.

From Figures 7 and 8, we can see that although compound brine shows better inhibitive effect on the shale sample compared with 10% NaCl, the NPBM-1 could embody much more inhibition effect on the shale samples and thus improve wellbore stability, either at ambient temperature or after being rolled at 180°C.

3.4. Rheological Model Analysis with DPS Software. The investigation of rheological model analysis is to study the relationship of shearing stress (τ) and shearing velocity (γ). In the regression process with DPS software, determination coefficient (R^2), test value (F), and significant level (p) were adopted to evaluate regression precision of different flow models. Results show that the optimal rheological models for the NPBM-1 and NPBM-2 were Herschel-Bulkley model and Power Law model separately.

In the fitting process, the optimal rheological model was chosen according to the coefficient of determination (R^2), the test value (F), and the significant level (p). High value of R^2 and F indicate that the observed value and the fitting value are closer, and it means that the dispersion of the point is relatively close to the curve from the whole point of view. The significant level (p) is considered as arithmetic root of residual sum of squares. Naturally, the fitting equation with smaller p is accurate so the p gives a measure of the deviation from the observation point and the regression curve.

With comprehensive consideration of R^2 , F , and p together, as shown in Tables 5 and 6, the optimal rheological models for the NPBM-1 and NPBM-2 were Herschel-Bulkley model and Power Law model, separately.

4. Discussion of the Mechanisms of the NPBM-1

In this section, the mechanics of the NPBM-1 were discussed in detail.

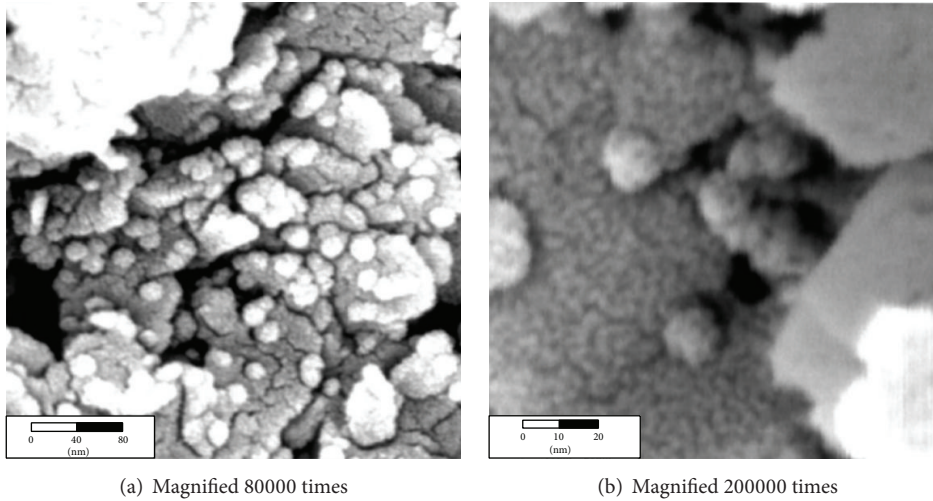
FIGURE 9: SEM picture of plugging shale using nano-SiO₂ [23].

TABLE 6: Rheological Equation fitting in different temperature of NPBM-2.

Flow pattern	Determination coefficient (R^2), test value (F), and significant level (p)			
	25°C	120°C	150°C	180°C
Bingham	$\tau = 10.550 + 0.075 \times \gamma$ $R^2 = 0.9413$, $F = 64.12$, $p = 0.0013$	$\tau = 10.794 + 0.096 \times \gamma$ $R^2 = 0.9547$, $F = 84.36$, $p = 0.008$	$\tau = 7.203 + 0.083 \times \gamma$ $R^2 = 0.9734$, $F = 146.39$, $p = 0.003$	$\tau = 4.591 + 0.067 \times \gamma$ $R^2 = 0.9801$, $F = 197.49$, $p = 0.001$
Power Law	$\tau = 1.567 \times \gamma^{0.570}$ $R^2 = 0.9988$, $F = 3226.91$, $p = 0.000$	$\tau = 1.306 \times \gamma^{0.629}$ $R^2 = 0.9929$, $F = 649.21$, $p = 0.000$	$\tau = 0.706 \times \gamma^{0.696}$ $R^2 = 0.9965$, $F = 1133.02$, $p = 0.000$	$\tau = 0.377 \times \gamma^{0.754}$ $R^2 = 0.9931$, $F = 574.27$, $p = 0.000$
Carson	$\tau^{1/2} = 3.128^{1/2} + 0.058^{1/2} \times \gamma^{1/2}$ $R^2 = 0.9802$, $F = 198.00$, $p = 0.001$	$\tau^{1/2} = 2.990^{1/2} + 0.076^{1/2} \times \gamma^{1/2}$ $R^2 = 0.9859$, $F = 280.20$, $p = 0.001$	$\tau^{1/2} = 1.763^{1/2} + 0.068^{1/2} \times \gamma^{1/2}$ $R^2 = 0.9916$, $F = 473.76$, $p = 0.000$	$\tau^{1/2} = 1.180^{1/2} + 0.054^{1/2} \times \gamma^{1/2}$ $R^2 = 0.9941$, $F = 678.97$, $p = 0.000$
Herschel-Bulkley	$\tau = 0.576 + 1.684 \times \gamma^{0.560}$ $R^2 = 0.9988$, $F = 1267.45$, $p = 0.000$	$\tau = 0.328 + 1.261 \times \gamma^{0.634}$ $R^2 = 0.9939$, $F = 244.04$, $p = 0.005$	$\tau = 0.764 + 0.636 \times \gamma^{0.710}$ $R^2 = 0.9966$, $F = 441.39$, $p = 0.002$	$\tau = 0.953 + 0.317 \times \gamma^{0.777}$ $R^2 = 0.9935$, $F = 227.57$, $p = 0.005$

4.1. Physical Plugging of Nanoparticles. To shale featured with nanosized pores, nano-SiO₂ has a fair chance of plugging the pores and forms low permeability sealing zones. The plugging of nano-SiO₂ into shale had been confirmed by Sensoy et al. [23] who ran scanning electron microscope tests (Figure 9) on the Atoka shale in contact with 20 nm nano-SiO₂. It is difficult for nano-SiO₂ to plug all the pore throats; however, the average pore throats would decrease with the plugging of nano-SiO₂ into the pore throats, which would increase the capillary force and restrict the further invading of drilling mud (Figures 7 and 8). On the other side, the sealing zone formed by nano-SiO₂ is beneficial to form thinner mud cake and lower fluid loss of drilling mud, as shown in Figure 3. Furthermore, approximate spherical nano-SiO₂ can act as nanosized bearings in mud cakes, improve the lubricity of mud cakes, and reduce the frictional resistance of drilling bits and tools especially in horizontal wells for shale gas.

As a whole, physical plugging of nano-SiO₂ can block the nanosized pore throats, restrict the transmission of pore pressure, and therefore improve wellbore stability.

4.2. Balanced Activity with Inorganic Salts. In case water activity of drilling mud is lower than that of the shale, osmotic pressure induced by the water activity difference can partially mitigate pressure transmission and fluid invasion from drilling mud into shale caused by hydraulic pressure. In the NPBM, the addition of NaCl and KCl can decrease water activity of the drilling mud to form balanced activity drilling mud to shale formation.

4.3. Chemical Inhibition. Shale inhibitor Soltex was used in the NPBM aiming at mitigating the water adsorption of shale. Plenty of ions with negative charge of Soltex can attach to the edge of ions with positive charge and restrict

water adsorption into shale. As one of the asphalt additives, Soltex can also squeeze into the possible micro fractures in shale driven by drilling mud pressure and improve the whole integrity of the wellbore. Additionally, other shale inhibitors and filtration additives as lockseal, SPNH, and SMP-II are beneficial to decrease fluid loss and further restrict the expansion and dispersion of shale and therefore improve wellbore stability.

4.4. Rational Drilling Mud Density. The pressure differential between drilling mud pressure and pore fluid pressure, which acts like a support pressure for the borehole, is a critical factor for wellbore stability. Too low mud density might cause overflow of pore fluid into the wellbore and even cause blowout of oil and gas while too high mud density would cause lost circulation and also speed up the invasion of fluid into shale. Generally, additional $0.1\text{--}0.2\text{ g/cm}^3$ over pore fluid pressure is acceptable.

Basing on the physical plugging of nanoparticles, balanced activity with inorganic salts, chemical inhibition, and rational drilling mud density, a synergic wellbore stabilization theory was simply described as follows. First, attapulgite was used for it has excellent salt resistance thus improving the filtration property of the NPBM. We also found that the mud had better thermal resistance and salt resistance when the proportion of attapulgite and bentonite was 1:1. Second, nano-SiO₂ had rather good thermal resistance at up to 180°C and can plug the nanosized pore throats existing in shale. It can also decrease fluid loss and improve the lubricity of the brine mud. Third, the addition of inorganic salts such as KCl and NaCl is helpful to lower water activity and to form balanced activity brine mud for shale. Fourth, powerfully chemical inhibition of Soltex can restrict water adsorption of shale. Fifth, in presence of proper portion of barite, mud density can be kept in a rational range to avoid wellbore instability or lost circulation. Finally, previous experiments showed that the recovery rate of gas permeability of coal samples was up to 72%–96% [25], indicating that the invasion of nano-SiO₂ was rather shallow which is beneficial for reservoir protection.

5. Conclusions

(1) The NPBM embodies excellent salt tolerance and thermal resistance for its rheological parameters did not suffer significant fluctuation. The NPBM-1 (4% NaCl plus 3% KCl) had a filtration of 7.6 mL at 180°C and the NPBM-2 (10% NaCl plus 3% KCl) had a filtration of 6.6 mL at 150°C.

(2) Rather low water activity and good lubricity of the NPBM improve the mud systems' capability for wellbore stabilization and reduce circulation friction resistance.

(3) Pressure transmission tests on the NPBM-1 indicate that the system has perfect performances in mitigating or even preventing the transmission of drilling mud pressure into shale thus improving wellbore stability.

(4) Basing on the physical plugging of nanoparticles, balanced activity with inorganic salts, chemical inhibition, and rational drilling mud density, a synergic wellbore stabilization theory was simply proposed with the NPBM.

(5) The optimal rheological models for the NPBM-1 and NPBM-2 were Herschel-Bulkley model and Power Law model separately.

Conflict of Interests

The authors declare that there is no conflict of interests regarding the publication of this paper.

Acknowledgments

The study is supported by the National Science Foundation of China (no. 41072111), the CNPC Innovation Foundation (no. 2014D-5006-0308), the Key Project of Natural Science Foundation of Hubei Province (no. 2015CFA135), and the Special Fund for Basic Scientific Research of Central Colleges (no. CUG130612).

References

- [1] M. Lal, "Shale stability: drilling fluid interaction and shale strength," in *Proceedings of the SPE Asia Pacific Oil and Gas Conference and Exhibition*, Society of Petroleum Engineers, Jakarta, Indonesia, April 1999.
- [2] R. P. Steiger and P. K. Leung, "Quantitative determination of the mechanical properties of shales," *SPE Drilling Engineering*, vol. 7, no. 3, pp. 181–185, 1992.
- [3] E. Van Oort, D. Ripley, I. Ward, J. W. Chapman, R. Williamson, and M. Aston, "Silicate-based drilling fluids: competent, cost-effective and benign solutions to wellbore stability problems," in *Proceedings of the SPE/IADC Drilling Conference*, SPE 35059, New Orleans, La, USA, March 1996.
- [4] M. E. Chenevert, "Shale control with balanced- activity oil-continuous muds," *Journal of Petroleum Technology*, vol. 22, no. 10, pp. 1309–1316, 1970.
- [5] R. T. Ewy and E. K. Morton, "Wellbore-stability performance of water-based mud additives," *SPE Drilling and Completion*, vol. 24, no. 3, pp. 390–397, 2009.
- [6] A. Hayatdavoudi and E. Apende, "A theoretical analysis of wellbore failure and stability in shales," in *Proceedings of the 27th U.S. Symposium on Rock Mechanics (USRMS '86)*, ARMA-86-0571, Tuscaloosa, Ala, USA, June 1986.
- [7] S. Carminati, L. Del Gaudio, and M. Brignoli, "Shale stabilisation by pressure propagation prevention," in *Proceedings of the SPE Annual Technical Conference and Exhibition*, SPE 63053, Dallas, Tex, USA, October 2000.
- [8] P. I. Reid, B. Dolan, and S. Cliffe, "Mechanism of shale inhibition by polyols in water based drilling fluids," in *Proceedings of the SPE International Symposium on Oilfield Chemistry*, SPE-28960-MS, San Antonio, Tex, USA, February 1995.
- [9] H. Zhong, Z. Qiu, W. Huang, and J. Cao, "Shale inhibitive properties of polyether diamine in water-based drilling fluid," *Journal of Petroleum Science and Engineering*, vol. 78, no. 2, pp. 510–515, 2011.
- [10] T. M. Al-Bazali, J. Zhang, M. E. Chenevert, and M. M. Sharma, "Measurement of the sealing capacity of shale caprocks," in *Proceedings of the SPE Annual Technical Conference and Exhibition*, SPE-96100-MS, Dallas, Tex, USA, October 2005.
- [11] P. H. Nelson, "Pore-throat sizes in sandstones, tight sandstones, and shales," *AAPG Bulletin*, vol. 93, no. 3, pp. 329–340, 2009.

- [12] A. R. Joseph, H. R. Chad, D. C. Mery, I. Y. Akkutlu, and C. Sondergeld, "New pore-scale considerations for shale gas in place calculations," in *Proceedings of the SPE Unconventional Gas Conference*, SPE 131772, Pittsburgh, Pa, USA, February 2010.
- [13] M. Milner, R. McLin, and J. Petriello, "Imaging texture and porosity in mudstones and shales: comparison of secondary and ion-milled backscatter SEM methods," in *Proceedings of the Canadian Unconventional Resources and International Petroleum Conference*, SPE 138975, Calgary, Canada, October 2010.
- [14] J. Schieber, "Common themes in the formation and preservation of intrinsic porosity in shales and mudstones—illustrated with examples across the Phanerozoic," in *Proceedings of the SPE Unconventional Gas Conference*, SPE 132370, Pittsburgh, Pa, USA, February 2010.
- [15] C. H. Sondergeld, R. J. Ambrose, C. S. Rai, and J. Moncrieff, "Micro-structural studies of gas shales," in *Proceedings of the SPE Unconventional Gas Conference*, SPE-131771-MS, Pittsburgh, Pa, USA, February 2010.
- [16] C. Zou, R. Zhu, B. Bai et al., "First discovery of nano-pore throat in oil and gas reservoir in China and its scientific value," *Acta Petrologica Sinica*, vol. 27, no. 6, pp. 1857–1864, 2011.
- [17] J. Cai, M. E. Chenevert, M. M. Sharma, and J. Friedheim, "Decreasing water invasion into Atoka shale using nonmodified silica nanoparticles," *SPE Drilling & Completion*, vol. 27, no. 1, pp. 103–112, 2012.
- [18] M. M. Sharma, M. E. Chenevert, Q. Guo, L. Ji, J. Friedheim, and R. Zhang, "A new family of nanoparticle based drilling fluids," in *Proceedings of the SPE Annual Technical Conference and Exhibition*, SPE-160045, Society of Petroleum Engineers, San Antonio, Tex, USA, October 2012.
- [19] S. Akhtarmanesh, M. J. A. Shahrabi, and A. Atashnezhad, "Improvement of wellbore stability in shale using nanoparticles," *Journal of Petroleum Science and Engineering*, vol. 112, pp. 290–295, 2013.
- [20] P. P. Kapadnis, B. H. Ghansar, S. P. Mandan, and P. Pandey, "Thermoelectric nanomaterial: a demiurgic approach towards improvement of shale stability," in *Proceedings of the SPE Unconventional Gas Conference and Exhibition*, SPE-164000-MS, Muscat, Oman, January 2013.
- [21] C. Liang, M. Chen, B. Lu et al., "The study of nano sealing to improve the brittle shale wellbore stability under dynamic load," in *Proceedings of the Offshore Technology Conference-Asia*, OTC-24919-MS, Kuala Lumpur, Malaysia, March 2014.
- [22] Y. Yuan, J. Cai, J. Wang, and C. Xiao, "Experimental study on improving filtration properties of drilling fluid using silica nano-particles," *Oil Drilling & Production Technology*, vol. 35, no. 3, pp. 30–41, 2013.
- [23] T. Sensoy, M. E. Chenevert, and M. M. Sharma, "Minimizing water invasion in shales using nanoparticles," in *Proceedings of the SPE Annual Technical Conference and Exhibition*, SPE-124429-MS, New Orleans, La, USA, October 2009.
- [24] F. K. Mody, U. A. Tare, C. P. Tan, C. J. Drummond, and B. Wu, "Development of novel membrane efficient water-based drilling fluids through fundamental understanding of osmotic membrane generation in shales," in *Proceedings of the SPE Annual Technical Conference and Exhibition*, SPE 77447, San Antonio, Tex, USA, September 2002.
- [25] J.-H. Cai, Y. Yuan, J.-J. Wang, X.-J. Li, and W.-J. Cao, "Experimental research on decreasing coalbed methane formation damage using micro-foam mud stabilized by nanoparticles," *Journal of the China Coal Society*, vol. 38, no. 9, pp. 1640–1645, 2013.

Research Article

Application of Polymeric Nanocomposites and Carbon Fiber Composites in the Production of Natural Gas Reservoirs

Gilberto João Pavani,¹ Sérgio Adalberto Pavani,² and Carlos Arthur Ferreira³

¹*Instituto Federal de Educação, Ciência e Tecnologia do Rio Grande do Sul, Avenida São Vicente 785, 95180-000 Farroupilha, Brazil*

²*Universidade Federal de Santa Maria, Avenida Roraima 1000, Prédio 5, 97105-900 Santa Maria, RS, Brazil*

³*LAPOL, Universidade Federal do Rio Grande do Sul, Avenida Bento Gonçalves 9500, 91501-970 Porto Alegre, RS, Brazil*

Correspondence should be addressed to Gilberto João Pavani; gilberto.pavani@farroupilha.ifrs.edu.br

Received 26 May 2015; Revised 4 August 2015; Accepted 11 August 2015

Academic Editor: Sessa Srinivasan

Copyright © 2015 Gilberto João Pavani et al. This is an open access article distributed under the Creative Commons Attribution License, which permits unrestricted use, distribution, and reproduction in any medium, provided the original work is properly cited.

This research work is about the experimental analysis of the mechanical behavior of reservoirs for storage of compressed natural gas (CNG) consisting of a nanopolymeric liner coated with carbon fiber preimpregnated with epoxy resin applied by filament winding (FW). It addresses technical solutions adopted to optimize the reservoir as reinforcement with fiber, the process of healing and thermal analysis, as well as the hydrostatic testing to verify its resistance to the pressure required for CNG storage. Different nanoclays were incorporated to the polymer aiming to increase the strength of the liner and to reduce the thickness of its wall and the final weight of the reservoir as well as decreasing gas permeability. The obtained results were the basis for proposing an adaptation of the equation traditionally used for the dimensioning of the wall thickness of metallic pressure vessels to determine the number of layers needed to endure any internal pressure to which the reservoir is subjected. They indicate that the used methodology enables the production of pressure vessels for the storage of CNG, according to the ISO 11439:2013 Standard.

1. Introduction

Natural gas is considered the fossil fuel with the lowest emissions of carbon dioxide, with low emission of pollutants and waste from the combustion process [1], allowing it to be efficiently used in internal combustion engines [2].

The main disadvantages presented by natural gas as an automotive fuel are the high cost of compression and the weight of the steel reservoir for transport and storage [3].

The use of reservoirs fabricated with nonmetallic material aims to reduce the inert load present in vehicles fueled by compressed natural gas (CNG), allowing fuel saving and the increase of the engine's life, as well as reducing the emission of pollutants.

This type of reservoir consists of a liner, whose primary function is gas impermeability, and reinforcement, whose main function is to resist the pressure of work.

The polymeric liner adds to the reservoir characteristics such as light weight, resistance to pressure and impact, corrosion protection, and durability [4] and is usually made

of rotomolded polyethylene (PE) due to the low cost of production. The PE is the most widely used resin for rotational molding due to low cost, chemical inertness, ease of processing, and mechanical properties [5] that can be improved by cross-linking or by the addition of nanoclays.

Rotational molding is suited for production of large and dimensionally stable hollow parts, with superficial finish comparable to injection molding. Additionally, as pointed out by Crawford and Throne [6], it has lower mold costs.

The high pressure of vehicular CNG storage requires the polymeric liner to be coated with carbon fiber, using the process of filament winding (FW) because of its low production cost, high productivity, and high reliability, besides providing nearly isotropic properties to the final product [7].

The liner is used as a mandrel in the FW process, allowing the arrangement of the fibers for structural reinforcement at various angles and patterns in the direction of the main solicitation by overlapping layers composed of nongeodesic winding and circumferential winding.

Based on the concept presented above, the Thiokol company has had success in the storage of hydrogen [8], but the main contribution of this work is the addition of nanoclay to the polyethylene blend, aiming to increase the polymeric liner's resistance to pressure as well as this polymer's gas permeability.

ISO 11439:2013 [9] covers cylinders of any seamless steel, seamless aluminium alloy, or nonmetallic material construction, using any design or method of manufacture suitable for the specified service conditions.

Thus, pressure vessels for CNG must conform to the ISO 11439:2013 Standard's Method, which specifies the requirements for the validation of CNG storage reservoirs for automotive vehicles, including buses and trucks.

The standard classifies as CNG-4 cylinders those produced entirely with nonmetallic materials, using appropriate manufacturing methods for the service conditions for vehicular transport, such as the reservoirs in development.

In order to increase the liner's resistance to pressure, the addition of nanoclays to polyethylene was chosen, adopting the following actions to achieve the standard pressure:

- (a) Analysis of possible failure on the existing liner.
- (b) Analysis of possible failure in the composite coating.
- (c) Adding more carbon fiber layers to satisfy the requirements of the standard.

Aiming to estimate the number of layers needed to endure any internal pressure to which the reservoir is subjected, an adaptation is proposed in the equation presented by Popov [10], having as base the hydrostatic tests' results made on reservoirs with one, two, and three layers of carbon fiber.

The proposed formula indicated that a fourth layer would meet the requirement of this standard, as calculated by linear regression and the equation proposed in this paper for calculating the number of layers for any internal pressure.

The obtained results indicate that the used methodology would allow the production of reservoirs for vehicular use classified as CNG-4, according to ISO 11439:2013, allowing a reduction of at least 60% (sixty percent) of the weight in relation to a steel cylinder.

2. Materials and Methods

2.1. CNG Reservoir. The polymeric liner in real scale ($\text{Ø}225 \times 725$ mm), with capacity for 22 liters of water, was manufactured by rotational molding, with a blend of LDPE/HDPE, coated with carbon fiber preimpregnated with epoxy resin, developed in a previous study [11].

2.2. Filament Winding. The simulation of the application of the reinforcement layers by FW was performed with the software CADWind 2007, version 8271 (Material SA).

The liner was used as a mandrel, being coated with in successive layers composed of nongeodesic winding and circumferential winding at a 10° angle which allows variation of the winding angle along a given section of the mandrel.

The layers were applied by a Kuka Roboter GmbH robot, type KR 140 L 100-2, for ensuring reliability and repeatability,

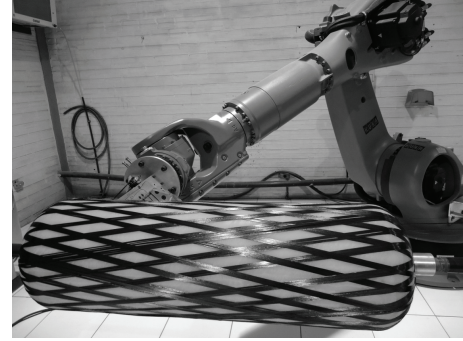


FIGURE 1: Nongeodesic winding.

shown in Figure 1, necessary characteristics to the reservoir in development that should store CNG.

The carbon fiber was applied at room temperature adopting as the cure cycle heating at $< 3^\circ\text{C}$ per minute to 90°C residence for 24 hours and cooling at $< 3^\circ\text{C}$ for a minute to 66°C before removal from the oven.

2.3. Reservoir Characterization

2.3.1. Hydrostatic Test. In that test, we used the Flutrol equipment (150 psi) with HBM 50 MPa load cell, Spindler 8, 60 Hz, HBM Interface. The samples were pressurized at 0.1 MPa/s and the data was processed with the Catman 4.0 Professional software.

2.3.2. Differential Exploratory Calorimetric Analysis. The samples were removed from the reservoirs with one, two, and three layers, taking as reference a carbon fiber sample taken from the roll in use, to check whether the cure cycle was adequate.

The samples were heated at a rate of $10^\circ\text{C}/\text{min}$ from room temperature to 250°C , with rapid cooling ($50^\circ\text{C}/\text{min}$) to room temperature, and again heated to 250°C .

The pieces of equipment used were DSC Q20 (TA Instruments) with nitrogen gas (N_2 Up) and graphs generated by Universal Analysis 2000 software, version 4.5 A, build 4.5.0.5, TA Instruments-Waters LLC.

The tensile testing of injection molded and rotomolded samples was carried out in the universal testing machine, aiming to select the best raw materials for the manufacturing of the liner regarding the mechanical strength.

The samples tested were as follows:

- (i) Blends of polyethylene.
- (ii) Blends of polyethylene with 5 weight% of Brazilian nanoclay.
- (iii) Blends of polyethylene with 5 weight% of American nanoclay.
- (iv) Blends of polyethylene with 5% of XLPE.
- (v) XLPE.
- (vi) XLPE with 5 weight% of Brazilian nanoclay.
- (vii) XLPE with 5 weight% of American nanoclay.

Remarks are as follows:

- (i) XLPE: ICORENE K1502 was from the company ICO Polymers.
- (ii) Brazilian nanoclay: montmorillonite clay with granulometry of 74 microns was produced by the company Bentonisa S/A.
- (iii) American nanoclay: montmorillonite Cloisite 30B clay was produced by the company Southern Clay Products.
- (iv) These products were mixed manually to the blend of polyethylene and extruded in single screw equipment.

The rotomolded samples were ground in a bench mill of the MTC Robotics brand, from the injected mold design, and taken directly from rotomolded parts.

The injected samples were produced in a brand mini-injector, Thermo Scientific, model MiniJet II Haake, with a standardized mold. The samples were injected at 185°C with two tons of pressure, except for the XLPE that was injected at 205°C.

Five samples of each raw material both machined and injected were subjected to a tensile test at 5,000 mm/min.

Tensile testing of carbon fiber preimpregnated with epoxy resin samples was conducted in the EMIC DL20000 brand universal testing machine, with a TRD26 load cell, TRD15 strain gauge, claws for polymeric films, and the MTest version 3.0 software, aiming to find the maximum tensile strength of a single strand of said fiber.

2.3.3. Oxygen Permeability Test. The test intended to measure the permeability of the liner to methane, but due to lack of equipment to measure the permeability, it verified the oxygen permeability which has compatible polarity and molecular diameter.

The test was performed with two groups of samples according to ASTM F 1927 (plates) [12] and ASTM D 3985 (film) [13].

The first group of samples consisted of hot pressed plates in the mold, cut 12 cm in diameter and machined to a thickness of 1 mm in the MTC milling machine.

Three samples were tested as follows:

- (i) Blend of polyethylene.
- (ii) Blends of polyethylene with 5% weight of Brazilian nanoclay.
- (iii) Blends of polyethylene with 5% weight of American nanoclay.

The second group of samples, consisting of films of polyethylene blend with nanoclay, had the pellets extruded at 250 rpm in twin screw corotating MH-Colour-20-32-Lab, after heating in an oven at 80°C for 24 hours for drying.

3. Results and Discussion

Reservoirs with three layers hit the average pressure of 350 bar \pm 5% when subjected to hydrostatic test but did not meet

TABLE 1: Relationship between layers, weight, and pressure.

Layers	Weight (kg)	Pressure (bar)
1	1,220 \pm 3%	150 bar \pm 5%
2	2,240 \pm 3%	250 bar \pm 5%
3	3,430 \pm 3%	350 bar \pm 5%



FIGURE 2: Reservoir destroyed.

the requirements of ISO 11439:2013 that determine the minimum pressure test for a CNG-4 reservoir as 2,25 times the working pressure, which is defined as 200 bar.

3.1. Hydrostatic Testing. Table 1 shows the average weight increase per layer and the average hydrostatic test results of the samples of liner coated with preimpregnated carbon fiber layers.

The calorimetric analysis by Differential Scanning Calorimetry indicates that the cure cycle for the preimpregnated carbon fiber with epoxy resin used in the reservoirs of one, two, and three layers was complete.

3.2. Fracture Liner. The fracture of the liner, in 80% (eighty percent) of the cases, regardless of the number of layers, occurred in the region near the tops due to lower wall thickness resulting from the manufacturing process by rotational molding, shown in Figure 2.

The simulation performed by Velosa et al. [14] indicated that the fracture occurred near the tops, a region of higher stress due to the action of the radial and the longitudinal stress, despite increased wall thickness.

In the case of the reservoir in development, the fracture also occurred near the tops, a region that has the lowest wall thickness, requiring adjustments to the project to increase the mechanical strength of the liner in the hydrostatic test.

However, careful control of the manufacturing process by rotomolding would maintain the continuity of the wall thickness of the polymeric reservoir, eliminating its significant reduction that causes premature rupture during hydrostatic testing. Furthermore, the addition of nanoclay increases the mechanical strength of the polyethylene blend constituting the reservoir and placing preimpregnated carbon fiber strips in the zone of concentration of the radial and longitudinal stresses results in increased resistance to pressure in said test.

3.3. Selection of New Materials for the Liner. In order to increase the liner's mechanical resistance and lower the nominal thickness of its wall, new materials were sought through tensile tests for its selection.

TABLE 2: Results of tensile testing of candidate materials (N).

Material	Rotomolded	Injected
Blend PE	143,84 ± 32,03	238,70 ± 18,37
Blend PE with 5 wt% of nanoclay, Brazilian	137,80 ± 11,38	205,12 ± 8,24
Blend PE with 5 wt% of nanoclay, American	140,74 ± 6,25	220,27 ± 3,79
Blend PE with 5% XLPE	151,23 ± 8,73	222,46 ± 5,06
XLPE	125,52 ± 4,07	267,44 ± 63,15
XLPE with 5 wt% of nanoclay, Brazilian	85,36 ± 4,25	364,08 ± 30,72
XLPE with 5 wt% of nanoclay, American	60,06 ± 4,74	367,95 ± 50,24

The tensile testing of such materials showed that the injected samples showed higher tensile strength than the rotomolded ones, that the addition of nanoclay increased tensile strength, and that American nanoclay (Cloisite 30B) showed better results than the Brazilian one because of it having more appropriate granulometry as observed in Table 2.

The literature recommends a weight percentage of nanoclay between 1% and 5% [15] for the gas barrier effect, but numerous studies indicate values optimized around 2% [16–18]. We opted for the limit value of 5% [19–21] to verify the influence of the type of nanoclay on the barrier and mechanical behavior of the reservoirs so that later the optimized value of the amount of nanoclay would be deemed appropriate for the purposes of this search.

In the tensile test, we adopted the von Mises criterion for the flow of an ideally plastic material in a triaxial stress state [22, 23]:

$$2(\sigma_y)^2 = (\sigma_1 - \sigma_2)^2 + (\sigma_2 - \sigma_3)^2 + (\sigma_3 - \sigma_1)^2, \quad (1)$$

where σ_y = flow tension at rupture, σ_1 = circumferential tension: σ_c , σ_2 = longitudinal tension: σ_l , and σ_3 = radial tension: σ_r .

Adjusting the equation,

$$2(\sigma_y)^2 = (\sigma_c - \sigma_l)^2 + (\sigma_l - \sigma_r)^2 + (\sigma_r - \sigma_c)^2. \quad (2)$$

In cylinders subjected to internal pressure, the expressions for σ_c , σ_l , and σ_r are

$$\begin{aligned} \sigma_c &= \frac{p \cdot d}{2} \cdot t, \\ \sigma_l &= \frac{p \cdot d^2}{(D^2 - d^2)}, \\ \sigma_r &= -\frac{p}{2}, \end{aligned} \quad (3)$$

where p is internal pressure in the cylinder, D is external diameter of the cylinder, d is inner diameter of the cylinder, and t is wall thickness.

Replacing these values in (2) and evidencing “ p ” we have

$$p = \frac{(4 \cdot \sqrt{3})}{3} \cdot \sigma_y \cdot \frac{(t - t^2/D)}{(D \cdot \sqrt{(1 - 4 \cdot t)/D})}. \quad (4)$$

Equation (4) shows that the cylinder’s burst pressure is directly proportional to the flow tension, whose value is close to the tensile resistance limit tension (σ_{rt}) obtained in the tensile test.

Thus, the higher the value of σ_{rt} , the greater the pressure supported by the cylinder in the hydrostatic test.

For Walters [23], do not use (4) to predict the burst pressure because σ_y differs from conventional yield stress (σ_e), obtained in the tensile test.

Therefore, in qualitative terms, it is possible to use the tensile test to select candidate materials for the manufacturing of CNG reservoirs.

3.4. Calculation of the Number of Layers of the Reservoir. The tensile testing of the carbon fiber preimpregnated with epoxy resin samples was carried out to find the maximum tensile strength of a single strand of fiber, allowing the calculation of the number of layers needed for any internal pressure that the reservoir is subjected to during hydrostatic testing.

In a cylindrical shell, there are two major strains:

- (i) Longitudinal stress (σ_l) which tends to break the tops, being supported by the nongeodesic winding.
- (ii) Circumferential stress (σ_c) which tends to break the side wall, being supported by circumferential winding.

For the design of a cylindrical reservoir, circumferential tension is used, because the longitudinal tension corresponds to half of this tension.

The tensile test conducted at IFRS resulted in an average tensile strength of $56.65 \text{ kgf/mm}^2 \pm 15\%$ for one preimpregnated filament of fiber, corresponding to resistance to circumferential tension.

The tensile strength of the nongeodesic winding is calculated by multiplying the value obtained in the tensile test by $\sin(10^\circ)$, resulting in an average tensile resistance of 9.84 kgf/mm^2 for one filament.

The value of the layer corresponds to the sum of the values, that is, 66.46 kgf/mm^2 .

The number of layers of a cylindrical reservoir can be calculated by tension caused by the internal pressure, according to (5) presented by Popov [10]:

$$\sigma_c = \frac{p \cdot r}{t}, \quad (5)$$

where σ_c is circumferential tension to the layer calculated from the value obtained in the tensile test in IFRS = 66.46 kgf/mm², p is internal pressure obtained in the hydrostatic testing for the three layers' reservoir = 3.57 kgf/mm², r is radius of the cylinder = 110 mm, and t is layer thickness (mm) = ?

Evidencing "t" in (5), we obtain

$$t = \frac{p \cdot r}{\sigma_c}, \quad (*)$$

where $t \sim 5.9$ mm = 6 layers.

However, the experimental results suggest that (*) must be adapted for coating in a preimpregnated carbon fiber composite as follows:

$$t = \frac{p \cdot r}{k} \cdot \sigma_c, \quad (*-1)$$

where k is the material factor and $k = 1$ for steel and $k = 2$ for preimpregnated carbon fiber.

Recalculating the number of layers of a cylindrical reservoir in preimpregnated carbon fiber ($k = 2$) in (*-1), we obtain the following result:

$$t = \frac{p \cdot r}{k} \cdot \sigma_c, \quad (*-2)$$

where $t \sim 2.95$ mm = 3 layers, which corresponds to the experimental result.

As the main function of the liner is gas impermeability, its small contribution to resistance to circumferential stress (σ_c) is disregarded.

Therefore, to calculate the number of layers for the standard pressure of 459 bar (4.59 kgf/mm²), using (*-1), we have the following result:

$$t = \frac{p \cdot r}{k} \cdot \sigma_c, \quad (*-3)$$

where p is internal pressure required by international standard = 4.59 kgf/mm², r is radius of the cylinder = 110 mm, k is material factor for preimpregnated carbon fiber composite = 2, σ_c is circumferential tension to the layer calculated from the value obtained in the tensile test in the IFRS = 66.46 kgf/mm², and approximately $t = 3.8$ mm corresponding 4 layers.

The value coincides with the calculation by linear regression and the equation proposed for calculating the number of layers for any internal pressure (see (*-1)), while maintaining the advantage in comparison to the weight of the steel cylinders.

In order to obtain the necessary pressure to halve the volume of the reservoir, at room temperature, (6) is used as follows:

$$P \cdot V = z \cdot n \cdot R \cdot T, \quad (6)$$

where P = pressure [Pa = N/m²]; V = volume [m³]; n = number of moles; R (Universal Gas Constant) = 8.3144 Nm/(mol·K); T = absolute temperature [K]; z = compressibility factor (z).

The compressibility factor represents the ratio between the volume occupied by given mass of gas under certain conditions of pressure and temperature and the volume that this mass would occupy at the same conditions as if it was an ideal gas [24].

The compressibility factor varies with the composition, pressure, and temperature of the gas and can be calculated by the equation of state of Dranchuk and Abou-Kassem [25].

As the gas is the same and its temperature remains constant in the compression process, we have

$$n = \frac{P1 \cdot V1}{z1} = \frac{P2 \cdot V2}{z2}, \quad (7)$$

where $P1$ (usual storage pressure) = 220 bar = 22 MPa, $V1$ = volume before compression = 1 m³, $z1 = 0.73286$ = compressibility factor, $P2 = ?$, $V2$ = volume after compression = 0.5 m³, $z2 = 1,41458$, and $P2 = 648$ kgf/cm² = 636 bar.

According to ISO 11439:2013, the hydrostatic test pressure of one CNG-4 reservoir is 2.25 times the working pressure, resulting in a 1.431-bar test pressure.

Calculating the number of layers of a cylindrical reservoir in preimpregnated carbon fiber, using (*-1), we obtain the following result:

$$t = \frac{p \cdot r}{k} \cdot \sigma_c, \quad (*-4)$$

where p (calculated hydrostatic test pressure) = 1.431 bar = 14.60 kgf/mm², r (radius of the cylinder) = 110 mm, k (material factor for preimpregnated carbon fiber composite) = 2, σ_c (circumferential tension to the layer calculated from the value obtained in the tensile test in the IFRS) = 66.46 kgf/mm², and $t = 12,13$ mm = 12 layers.

Equation (*-1) indicates that a fourth layer of carbon fiber will meet the requirements of ISO 11439:2013, resisting the pressure of 495 bar for hydrostatic testing, maintaining the advantage in relation to the weight.

3.5. Gas Permeability. The oxygen permeability test was performed on two groups of samples: rotomolded plates and film, adopted as reference.

The result of the permeability in the tested sheets is as follows:

- (i) Polyethylene blend: 13,660 mL (STP/m²/day) at 1 atm and 23°C.
- (ii) Blends of polyethylene with 5% weight of Brazilian nanoclay: 32,829 mL (STP/m²/day) at 1 atm and 23°C.
- (iii) Blends of polyethylene with 5% weight of American nanoclay: 150,000 mL (STP/m²/day) at 1 atm and 23°C (detection limit of the equipment).

The high permeability shown by rotomolded samples nanoclays is due to the processing in a single screw extruder which did not allow the adequate shear and distribution of the clay particles.

The following samples were analyzed in films:

- (i) Sample A: HDPE Blend (95%), LDPE (5%), and sodium nanoclay (no compatibilizer).

TABLE 3: Oxygen permeability coefficient (PO_2) at 23°C, dry.

Sample	PO_2 (mL (STP)· $\mu\text{m}\cdot\text{m}^{-2}\cdot\text{day}^{-1}\cdot\text{atm}^{-1}$)		
		Average	Individual values
Sample A Nanoclay sodium	295.761	144.332/309.589/433.364	49
Sample B Cloisite 15A	40.258	36.284/44.232	14
Sample C Cloisite 30B	93.236	60.644/63.405/155.659	58

- (ii) Sample B: HDPE Blend (95%), LDPE (5%), and Cloisite 15A nanoclay.
 (iii) Sample C: HDPE Blend (95%), LDPE (5%), and Cloisite 30B nanoclay.

The rates of oxygen permeability (TPO_2) were determined by coulometric method according to standard D3985-05 (ASTM, 2010), in OXTRAN equipment, model 2/20, from the company Mocon, operating with pure oxygen as permeant gas.

The tests were performed at 23°C with the conditioning of samples at 23°C with no humidity for 46 to 48 hours. The effective permeation area of each sample was 100 cm².

The obtained results were corrected to 1 atm of oxygen partial pressure gradient between the two surfaces of the film, since this gradient corresponds to the driving force for permeation of the oxygen through the film.

Although the rate of oxygen permeability is characteristic of the film, the permeability coefficient was used, which characterizes the composite to minimize the effect of variation in thickness of the samples in the comparison.

The material was processed in a twin screw extruder, but the speed of 250 rpm did not allow adequate shear and distribution of the clay particles.

Once TPO_2 was determined, the oxygen permeability coefficient (P) was calculated from the permeability rate as follows:

$$P = \frac{TPO_2 \cdot e}{p}, \quad (8)$$

where Q is oxygen permeability coefficient (mL (STP)· $\mu\text{m}\cdot\text{m}^{-2}\cdot\text{day}^{-1}\cdot\text{atm}^{-1}$); TPO_2 is oxygen permeability rate (mL (STP) $\text{m}^{-2}\cdot\text{day}^{-1}$); e is average thickness of the samples (μm); p is partial pressure of oxygen in the permeating gas chamber of the diffusion cell, because the partial pressure of O_2 in the carrier gas chamber is void.

The results of the oxygen permeability coefficient are presented in Table 3.

Table 3 shows that the sample with nanoclay Cloisite 15A has lower oxygen permeability coefficient, confirming the manufacturer's recommendation that indicates Cloisite 15 compatibilized with maleic acid for polyethylene due to the hydrophobicity of the polymer.

4. Conclusions

It is estimated that a fourth layer of carbon fiber will meet the requirements of ISO 11439:2013, supporting pressure of 495 bar for hydrostatic testing, maintaining the advantage in relation to the weight as calculated by linear regression and (*-1).

It was found that, in 80% (eighty percent) of the reservoirs, the fracture of the liner, regardless of the number of layers, occurred in the region near the tops, due to lower wall thickness resulting from the manufacturing process by rotational molding, corrections being required in the project, change of materials and better control in the process to increase the strength of the liner.

Despite the difference in format between the reservoir in development and the one presented by Velosa et al. [14], there are similarities in the location of fractures resulting from hydrostatic test and the ones found in the simulation that indicated fractures near the tops, the region of highest stress.

In the case of reservoir in development, the region close to the tops has the lowest wall thickness, according to the measurements performed in the liner, requiring adjustments to the project to increase the mechanical strength of the liner in the hydrostatic test.

To increase the mechanical strength of liner and reduce the nominal wall thickness from 10 mm to 7 mm, maximum thickness allowed by rotational molding, we sought new materials with rotomolded and injection molded samples.

The injected samples have higher tensile strength than the rotomolded ones, and the addition of nanoclay increases the tensile strength and the nanoclay Cloisite 30B shows better results than the Brazilian one due to the smaller particle size.

The low results obtained in the rotomolded test bodies with nanoclays are due to processing in a single screw extruder which did not allow adequate shear and distribution of the clay particles, unlike the test samples that were injected at better processing conditions.

Despite the XLPE obtaining the best result in the injected test samples, it showed the worst result as rotomolded samples, being discarded from the process for being permeable to oxygen and, by extension, to methane.

The qualitative method of selection through tensile test to evaluate the mechanical strength of the samples is justified by the application of the von Mises criterion for the flow of an ideally plastic material in a triaxial stress state, adapted to the uniaxial stress state, according to Walters.

The gas permeability is also an essential requirement for the selection of a material for the production of CNG reservoirs, but as it was not feasible to perform testing with methane, the main component of the CNG, we used oxygen which is compatible with it in terms of molecular diameter and polarity.

The high permeability shown by the rotomolded samples with nanoclays is due to processing in a single screw extruder which did not permit good distribution and adequate shearing of the clay particles, demonstrated by the results of permeability which increased with the addition of clay.

The value of the permeability of the blends of polyethylene with nanoclay Cloisite 30B reached the limit of scale equipment, because the smaller the particle is, the greater the tendency it has to be grouped, facilitating the gas passages.

As for the film, the permeability coefficient was used, which characterizes the composite in order to minimize the effect of thickness variation in the comparison of the samples. The permeability coefficient characterizes the barrier of homogeneous materials, not being entirely accurate in this case.

The material was processed in a twin screw extruder, but the speed of 250 rpm did not allow adequate shear and distribution of the clay particles, preventing the samples from becoming homogeneous.

From the data obtained it appears that the sample with nanoclay Cloisite 15A has lower coefficient of oxygen permeability.

As the pressure of the CNG reservoirs is 220 times greater than the gas permeability test performed, the values tend to increase significantly for methane reservoirs.

It was shown that it is possible to halve the volume of vehicular CNG reservoirs, maintaining autonomy equivalent to liquid fuels, by increasing the storage pressure to 636 bar, resulting in a hydrostatic test pressure of 1,431 bar according to ISO 11439:2013, 18 layers of composite to be supported, as calculated according to Formula (*-1).

Therefore, the use of the reservoir in development is a viable alternative for vehicles fueled by CNG for it reduces the inert load, linking fuel saving to increased engine life, besides adding ecological and economic benefits to society, as well as optimizing the useful volume of the trunk by providing new formats of fuel reservoir to meet the growing range of models due to the internationalization of the car market.

Conflict of Interests

The authors declare that there is no conflict of interests regarding the publication of this paper.

Acknowledgments

The authors are grateful to IFRS, LAMEF/UFRGS, ITAL, UCS, and Xalingo for providing equipment for the testing needed for this research work.

References

- [1] V. Chandra, *Fundamentals of Natural Gas: An International Perspective*, Penn Well, Tulsa, Okla, USA, 2006.
- [2] V. Ganesan, *Internal Combustion Engines*, McGraw-Hill, New Delhi, India, 3rd edition, 2008.
- [3] J. G. Speight, *Natural Gas: A Basic Handbook*, Gulf Publishing, 2007.
- [4] Y. Li, J. C. Liang, W. Zhang, W. Qi, M. Su, and C. D. Liu, "Study on process and impact strength for a rotationally molded truck fender," *Journal of Materials Processing Technology*, vol. 187-188, pp. 492-496, 2007.
- [5] R. J. Crawford, *Rotational Molding*, Rapra Technology, 1993.
- [6] R. J. Crawford and J. L. Throne, *Rotational Molding Technology*, William Andrew Publishing, 2002.
- [7] F. C. Shen, "A filament-wound structure technology overview," *Materials Chemistry and Physics*, vol. 42, no. 2, pp. 96-100, 1995.
- [8] T. Propulsion, "High-pressure conformable hydrogen storage for fuel cell vehicles," in *Proceedings of the 2000 Hydrogen Program Review*, San Ramon, Calif, USA, 2000.
- [9] ISO 11439:2013 Gas cylinders—High pressure cylinders for the on-board storage of natural gas as a fuel for automotive vehicles, 2015, <http://www.iso.org>.
- [10] E. P. Popov, *Introdução à Mecânica dos Sólidos*, Blucher, São Paulo, Brazil, 1978.
- [11] E. S. Barboza Neto, L. A. F. Coelho, M. M. C. Forte, S. C. Amico, and C. A. Ferreira, "Processing of a LLDPE/HDPE pressure vessel liner by rotomolding," *Materials Research*, vol. 17, pp. 236-241, 2013.
- [12] ASTM International, *ASTM F1927—Standard Test Method for Determination of Oxygen Gas Transmission Rate, Permeability and Permeance at Controlled Relative Humidity Through Barrier Materials Using a Coulometric Detector*, ASTM International, West Conshohocken, Pa, USA, 2015, <http://www.astm.org/Standards/F1927.htm>.
- [13] ASTM, "Standard test method for oxygen gas transmission rate through plastic film and sheeting using a coulometric sensor," ASTM D3985, 2010, <http://www.astm.org/Standards/D3985.htm>.
- [14] J. C. Velosa, J. P. Nunes, P. J. Antunes, J. F. Silva, and A. T. Marques, "Development of a new generation of filament wound composite pressure cylinders," *Ciência e Tecnologia dos Materiais*, vol. 19, no. 1, pp. 1-9, 2007.
- [15] A. L. Brody, "Nano and food packaging technologies converge," *Food Technology*, vol. 60, no. 3, pp. 92-94, 2006.
- [16] S. Pavlidou and C. D. Papaspyrides, "A review on polymer-layered silicate nanocomposites," *Progress in Polymer Science*, vol. 33, no. 12, pp. 1119-1198, 2008.
- [17] M. N. Khalaf, "Control the discontinuity of the flow curve of the polyethylene by nanoclay and compatibilizer," *Arabian Journal of Chemistry*, 2012.
- [18] M. R. Manikantan and N. Varadaraju, "Preparation and properties of linear low density polyethylene based nanocomposite films for food packaging," *Indian Journal of Engineering & Materials Sciences*, vol. 19, no. 1, pp. 54-66, 2012.
- [19] T. P. Mohan and K. Kanny, "Melt blend studies of nanoclay-filled polypropylene (PP)—high density polyethylene (HDPE) composites," *Journal of Materials Science*, vol. 48, no. 23, pp. 8292-8301, 2013.
- [20] N. Saba, P. M. Tahir, and M. Jawaid, "A review on potentiality of nano filler/natural fiber filled polymer hybrid composites," *Polymers*, vol. 6, no. 8, pp. 2247-2273, 2014.
- [21] M. Alexandre and P. Dubois, "Polymer-layered silicate nanocomposites: preparation, properties and uses of a new class of materials," *Materials Science and Engineering R: Reports*, vol. 28, no. 1, pp. 1-63, 2000.
- [22] H. Sehitoglu, *Thermomechanical Fatigue Behavior of Materials*, ASTM, 1993.
- [23] J. A. Walters, *Hoop-Wrapped Composite, Internally Pressurized Cylinders*, ASME Press, 2003.
- [24] C. Borgnakke and R. E. Sonntag, *Fundamentos da Termodinâmica*, Blucher, São Paulo, Brazil, 7th edition, 2009.
- [25] Equation, 2015, <http://checcalc.com/solved/naturalgasZ.html>.